UNIVERSITAT DE BARCELONA

Collapse scenarios in magnetized star-forming regions

Carmen Juárez Rodríguez

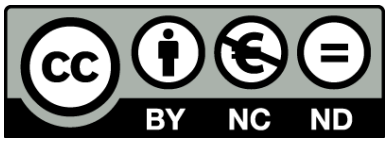

Collapse scenarios in magnetized star-forming regions

Carmen Juárez Rodríguez

Advisors: Josep M. Girart Medina & Aina Palau Puigvert
Tutor: Robert Estalella Boadella

Programa de doctorat en Física
Departament de Física Quàntica i Astrofísica

Facultat de Física

UNIVERSITAT DE
BARCELONA

This dissertation is submitted for the degree of

Doctor per la Universitat de Barcelona

April 2017

A mi madre y a Marina

Acknowledgements

I would like to thank my supervisors Josep M. Girart and Aina Palau for the opportunity of this great experience, for all the knowledge shared with me and for all the guidance throughout these years, I enjoyed very much all the projects and working with you. I want to also thank Robert Estalella, who has been a third supervisor to me. Thank you for introducing me to star formation and radioastronomy and for all the discussions throughout all the projects during all these years. I would also like to thank the people of Barcelona's radio group: Rosario López, Chema Torrelles, Angels Riera, Inma Sepúlveda, João Lin, Paula Teixeira, Gemma Busquet, Pau Frau, Alvaro Sánchez, Felipe Alves, Nacho Añez and Søren Frimann. It is a great group to work with, thank you all for the great science discussions and for providing such a great environment to work.

Thank you very much to Núria Vinyoles, Carles Moyano, Laura Delgado, Arnau Pujol, Albert Izard, Ramon Padullés, Antonia Morales, Jonatan Martín, Daniel Santos, Anna Maria Porredon, Marina Lafarga, Daniele Viganò, Hilda Rodríguez, Marina Martínez, Juan Pedro López, Fran Rivas, Manuel Moreno and everybody at ICE. Thank you for all the good moments and for all the support during these years, it was a pleasure to go to work with you every day.

Special thanks to Paul Ho, Patrick Koch, Ya-Wen Tang, Hauyu (Baobab) Liu, Naomi Hirano, Oscar Morata, Thomas Lai and everybody I met at ASIAA (Taiwan), to Javier Ballesteros, Manuel Zamora, Enrique Vázquez, Luis Felipe Rodríguez, Roberto Galván, Alba Fernández, Andrés Pérez, Bernardo Cervantes and everyone at IRyA (Mexico) and to Qizhou Zhang, Luca Ricci and all the people at the CfA (USA), who made my stays at the institutes amazing experiences.

Also special thanks to the staff and astronomers working at the CSO (Hiroko Shinnaga, Simon Radford, Lei Qian and Hua-bai Li), GBT (Sam Bates and Joe Masters), SMA (Ryan Howie) and IRAM 30m (Ignacio Ruiz, Manuel Ruiz and Albrecht Sievers) observatories while I was visiting. Thank you very much for your help during the observations, visiting the observatories was a dream come true. Special thanks to Ram Rao for helping me to reduce the SMA data at Hilo.

Thank you to Josep Guerrero and Jordi Vidal for all the help with the computers at ICE and at UB. Thank you as well to the administration team at ICE (Isabel Molto, Guadalupe Masip, Josefa López, Fina Ruiz and Angels Benet) and at the FQA department at UB (José Ramón Rodríguez and Rosa Iborra).

Thank you very much to Adri, Glori, Kim, Fabián, Kumy, Guillem and all the tico's team for all the good times and support these years!

Finally, thank you very much to my family for always supporting me, this thesis is for them. And thank you to Marina for loving me and always be by my side, these years in Barcelona have been amazing. I can't wait to see what's next. I love you.

Table of contents

List of figures

List of tables

Resumen en castellano

El campo de investigación de la tesis doctoral se enmarca dentro del área de astrofísica, específicamente en el área de la formación estelar observacional.

La turbulencia, el campo magnético y la gravedad juegan un papel importante en la formación de nuevas estrellas. Aunque se ha mostrado que el campo magnético es importante en la formación de estrellas, sólo se han llevado a cabo un número limitado de trabajos combinando el estudio del campo magnético y la cinemática del gas en regiones de formación estelar (e.g., Girart et al., 2013; Zhang et al., 2014). Este tipo de trabajos son importantes para estudiar la gravedad y la dinámica del gas y poder compararlas con el campo magnético. En este trabajo combinamos estudios de polarización a partir de la emisión del polvo, con el análisis de la cinemática del gas en diferentes regiones de formación estelar. El objetivo es estudiar las propiedades físicas a escalas de núcleos densos (< 0.1 pc), a partir de la emisión molecular y del polvo (total y polarizada), y estudiar el papel del campo magnético en la evolución dinámica de las regiones. Para ello hemos utilizado datos observacionales milimétricos y submilimétricos obtenidos con los interferómetros Plateau de Bure (PdBI) y Submillimeter Array (SMA) y con el radiotelescopio IRAM 30m. Los estudios se han realizado en 3 regiones de formación estelar de baja y alta masa en diferentes entornos y estados evolutivos.

Correlación entre química, polarización y propiedades del polvo en el núcleo pre-estelar FeSt 1-457, en la nebulosa de la Pipa

El primer proyecto de la tesis consiste en el estudio de las propiedades físicas, químicas y magnéticas del núcleo pre-estelar FeSt 1-457 (core 109). Como aún no se ha formado la protoestrella, es una región ideal para estudiar las etapas más tempranas de la formación estelar. FeSt 1-457 se encuentra en un entorno aislado y muy magnetizado en la región del "bowl" en la nebulosa de la Pipa. FeSt 1-457 tiene una masa de 4 $M_\odot$ y un tamaño de ~ 0.1 pc (e.g., Frau et al., 2010). Con datos observacionales obtenidos con el telescopio IRAM 30m y el interferómetro PdBI estudiamos en detalle la emisión de la línea molecular N_2H^+ (1–

0), la cual es buena trazadora de gas denso y por lo tanto describe bien la estructura del núcleo. A partir del ajuste hiperfino de la emisión se crearon mapas de velocidad, densidad columnar y anchura de línea. Además, detectamos más de 15 líneas moleculares y encontramos una clara diferenciación espacial química para moléculas con nitrógeno, oxígeno y azufre. Con el código de transferencia radiativa ARTIST (Brinch and Hogerheijde, 2010; Jørgensen et al., 2014; Padovani et al., 2012, 2011) estimamos la abundancia de las diferentes moléculas a partir de la comparación de los datos observacionales con mapas sintéticos de la emisión de cada una de ellas. Encontramos una clara disminución de la abundancia hacia el centro del núcleo de al menos uno o dos órdenes de magnitud para la mayoría de las moléculas detectadas.

Por otro lado, estimamos las propiedades magnéticas del core utilizando la aproximación de Chandrasekhar-Fermi (Chandrasekhar and Fermi, 1953), a partir de los datos de polarización presentados en Alves et al. (2014), y el cociente entre la masa y el flujo magnético. Obtuvimos que el núcleo es magnéticamente supercrítico, lo cual implica que el campo magnético no es suficientemente fuerte para impedir el colapso gravitatorio. Además, encontramos correlaciones interesantes entre las propiedades de polarización y la química de la región. La depleción de moléculas en los granos de polvo ocurre en el interior del núcleo denso, donde el crecimiento de los granos (Forbrich et al., 2015) y la depolarización también ocurren. Por otro lado, las asimetrías en la emisión molecular, parecen estar correlacionadas con la asimetría de la polarización submilimétrica. Ambas asimetrías pueden ser debidas a un campo de radiación interestelar desde el lado oeste del núcleo. Finalmente, a partir de la emisión de CO observamos que FeSt 1-457 se encuentra en el borde entre dos estructuras moleculares separadas por 3 km s^{-1}, posiblemente dos flujos de gas denso que convergen justo en la posición del núcleo pre-estelar y que pueden haber afectado su evolución.

Flujos de gas convergentes en NGC 6334 V

El segundo proyecto es el estudio de una región de mayor masa (NGC 6334 V), en un estado evolutivo más avanzado (con presencia de fuentes de radio e infrarrojas, másers y flujos moleculares) y en un entorno rodeado de otras regiones de formación estelar masiva. NGC 6334 V es parte de un filamento con un tamaño proyectado de ~ 20 pc y que a lo largo alberga cuatro regiones más de formación estelar masiva. Los datos forman parte del proyecto Legado de gran envergadura del SMA “Filaments, Star Formation and Magnetic Fields”.

Durante el proyecto estudiamos el campo magnético a partir de la emisión polarizada del polvo y también la cinemática del gas a partir de la emisión de los diferentes trazadores de gas denso. El tamaño y masa total de la región a partir de la emisión del polvo son ~ 0.1 pc

y $\sim$ 50 $M_\odot$, respectivamente. De la emisión molecular del gas trazando la envoltura del núcleo denso, vemos dos estructuras de velocidad diferentes separadas por 2 km s^{-1} y convergiendo hacia la región más densa. Además, el campo magnético también presenta un patrón bimodal siguiendo la distribución de las dos componentes de velocidad. Finalmente, comparamos los resultados observacionales con simulaciones numéricas magnetohidrodinámicas en 3 dimensiones de regiones de formación estelar dominadas por gravedad.

En NGC 6334 V, los resultados del estudio de la cinemática y el campo magnético, tanto en las observaciones como en las simulaciones, muestran como el gas converge desde la envoltura del núcleo a mayor escala ($\sim$ 0.1 pc) hacia la región más densa ($\sim$ 0.02 pc) a través de flujos de gas denso que arrastran el campo magnético, cuya fuerza parece haber sido superada por la gravedad.

Flujos convergentes + rotación en L1287

El último proyecto es el estudio de una región de formación estelar de menor masa, L1287. Imágenes de *Herschel* de la región muestran una estructura filamentaria con un tamaño proyectado de $\sim$ 10 pc con L1287 localizada aproximadamente en el centro. Datos del proyecto Planck muestran emisión polarizada bien alineada a lo largo del filamento.

A partir de datos obtenidos con el SMA, la estructura de la emisión de continuo del polvo muestra seis núcleos densos principales con masas entre $\sim 0.4 - 4$ $M_\odot$ y con un tamaño promedio de $\sim$ 0.03 pc. El tamaño y la masa total de la región son $\sim$ 0.1 pc y $\sim$ 25 $M_\odot$, respectivamente. Los núcleos densos de mayor masa son el núcleo central ($\sim$ 4 $M_\odot$, asociado al objeto RNO1C) y el núcleo denso asociado al objeto estelar joven IRAS 00338+6312 ($\sim$ 2 $M_\odot$). A mayor resolución angular, el núcleo denso central se divide en ocho fragmentos formando una estructura "toroidal". Sin embargo, el núcleo denso asociado a IRAS 00338+6312 no muestra fragmentación adicional.

Por otro lado, la molécula trazadora de gas denso DCN (3–2) muestra dos estructuras de velocidad separadas por 2–3 km s^{-1}, formando dos gradientes claros de velocidad, uno a gran escala centrado en el núcleo denso central y otro más compacto centrado en el núcleo denso asociado a la fuente IRAS 00338+6312. Los dos gradientes de velocidad podrían pertenecer a un mismo escenario de flujos convergentes hacia la región de más alta densidad, la fuente IRAS 00338+6312. Por lo tanto, L1287 parece presentar un escenario similar al que vemos en la región de alta masa NGC 6334 V, con dos estructuras de velocidad que parecen converger hacia el pozo de potencial de la región. Además, el flujo molecular de alta velocidad interactúa con el gas denso afectando la compleja cinemática, la química y la estructura del polvo de la región.

Conclusiones

Los estudios del núcleo pre-estelar FeSt 1-457 y la región de formación estelar de alta masa NGC 6334 V muestran como el campo magnético en ambas regiones ha sido superado por la gravedad y no es suficiente para evitar el colapso gravitatorio. En el caso de FeSt 1-457, el núcleo se encuentra en un estado evolutivo muy temprano y en un entorno aislado y muy magnetizado. La localización del núcleo, en el borde entre dos flujos de gas denso diferentes, puede haber afectado su evolución. El ajuste de una esfera de Bonnor-Ebert muestra que FeSt 1-457 es gravitacionalmente inestable. Además, el cociente entre masa y flujo magnético muestra que el núcleo denso es magnéticamente supercrítico, lo cual indica que el soporte del campo magnético no es suficiente para mantener su estabilidad. Por otro lado, NGC 6334 V es un objeto más evolucionado y de mayor masa, con varias fuentes infrarrojas y de radio, y gas de alta velocidad debido a flujos moleculares. En este caso, también observamos cómo la gravedad domina sobre el campo magnético, viendo cómo el campo magnético es arrastrado por las estructuras de gas denso convergentes.

Por otro lado, NGC 6334 V y la región de menor masa L1287 presentan escenarios muy similares con el material convergiendo desde la envoltura de gas denso a escalas grandes (~ 0.1 pc) hacia los pozos de potencial de ambas regiones a escalas más pequeñas (~ 0.02 pc) a través de flujos de gas separados por 2–3 km s^{-1}. Además, ambas regiones presentan características similares ya que albergan fuentes en diferentes estados evolutivos, tanto fuentes centimétricas e infrarrojas como también protoestrellas todavía muy embebidas. Tanto diferentes poblaciones de objetos como flujos convergentes de gas denso son características de un escenario de colapso global jerárquico, sin embargo, no se puede descartar un medio turbulento.

En un escenario parecido al de NGC 6334 V y L1287, FeSt 1-457 se encuentra justo en la zona donde parecen converger dos flujos de gas separados por 3 km s^{-1}, sin embargo, en este caso las observaciones trazan dos estructuras de gas menos densas. La posición del núcleo precisamente en el borde entre las dos estructuras puede haber afectado su evolución. Hemos observado que la presión térmica en el núcleo parece dominar sobre la presión debida a la turbulencia y que el núcleo pre-estelar está colapsando gravitacionalmente, con el campo magnético no siendo lo suficientemente fuerte para impedirlo. Contrariamente al caso de NGC 6334 V y L1287, en FeSt 1-457 sólo una de las dos estructuras de gas de baja densidad está asociada al núcleo denso. En este caso, las direcciones del campo magnético y del gradiente de velocidad son perpendiculares (al contrario que en el caso de NGC 6334 V). Aunque la gravedad es la fuerza dominante en FeSt 1-457, es posible que el campo magnético sea lo suficientemente fuerte como para que sea dinámicamente más importante que en los casos de regiones más masivas.

Chapter 1

Introduction

1.1 Star formation

1.1.1 Molecular clouds

Stars form in the densest and coldest parts of the interstellar medium, the molecular clouds. Their distribution is close to the galactic plane and they occupy a small fraction ($\sim 2\%$) of the volume of the galaxy. However, they represent half of the mass of the interstellar medium. Their typical temperature is between $10-30$ K, and their density ranges between 10^3-10^5 cm^{-3}. They consist of gas and ~ 0.1 μm size dust grains. The gas component is mostly molecular hydrogen (H_2), with traces of other molecules (CO, NH_3, CH_3OH, ...). The most abundant molecule after H_2 is CO ([CO/H_2]$\sim 10^{-6}$). The gas presents a small ionization fraction ($x_e \sim 10^{-7}$, relative to H_2; Caselli et al., 1998), which implies weak coupling of the gas to the magnetic field. On the other hand, the dust mass present in the interstellar medium is approximately 1% with respect to the gas mass. Dust particles emit thermal emission at millimeter and submillimeter wavelengths. In the regions studied in this work, only a negligible amount of the dust emission is attributable to non-thermal processes such as free-free emission.

Molecular clouds can be classified into dark clouds and giant molecular clouds (GMC) depending on their size. Dark clouds are more abundant and thus we can find them at short distances from the Sun. Their masses vary between 10^3-10^4 solar masses ($M_\odot$) and they present sizes of about $2-10$ pc. One of the closest dark clouds is the Pipe nebula, located at just 145 pc. On the other hand, GMCs are much less abundant. Their mass and size can reach up to 10^6 $M_\odot$ and 100 pc, respectively. High-mass stars ($M \gtrsim 8$ $M_\odot$) are formed inside GMCs, however, low-mass stars ($M < 8$ $M_\odot$) can be formed in both dark clouds and GMCs.

By studying the molecular clouds we can learn about the initial conditions in which stars are formed. As stars are formed by the contraction of molecular gas, the youngest stars are mostly found in the densest parts of the molecular clouds. The term *molecular clump* is generally referred to entities of ~ 1 pc spatial scales. In this thesis we are especially interested in smaller scales, specifically in $0.01 - 0.1$ pc scale entities, where *dense cores* will form one or a group of stars.

During the star formation process, the initial material of the molecular cloud contracts by the effects of gravity, increasing the density about 20 orders of magnitude and reaching temperatures up to $\sim 10^7$ K, where fusion of hydrogen begins.

1.1.2 Observational evolutionary stages

Low-mass stars

Low-mass stars form from the collapse of dense pre-stellar cores in molecular clouds. These cores are characterized by very low temperatures ($\lesssim 10$ K) and high densities $> 10^4$ cm^{-3}. During the last stage of a pre-stellar core, when the density at its center exceeds a critical value, the core becomes dynamically unstable and starts to collapse. Once the collapse has started, the protostar is formed at the center in a short timescale ($\sim 10^3 - 10^4$ years).

In the first protostellar phase (Class 0), the protostar gains mass by accreting the surrounding material from its envelope through an accretion disk. Some of the accreted material is accelerated and expelled at high-velocities perpendicularly to the disk through a jet creating molecular outflows. During the Class I phase, the outflow has cleared out some of the envelope material, the protostar has increased its temperature and becomes visible in the infrared. In the Class II phase (T Tauri phase), the envelope is almost entirely removed, the accretion decreases with time and the protostar enters the pre-main sequence stage (Class III). During this phase, the main source of energy is the stellar gravitational contraction. When the temperature at the interior of the protostar reaches $\sim 10^7$ K, fusion of hydrogen to form helium begins and a new star is born. The entire process lasts $\sim 10^7$ years.

High-mass stars

The evolutionary stages of massive stars ($M \gtrsim 8$ M$_\odot$) are still unclear. Since high-mass stars tend to form in clusters, are located at large distances from the Sun ($\gtrsim 1$ kpc), and have short evolution timescales, they are hard to observe and to study.

Infrared Dark Clouds (IRDCs), seen at infrared wavelengths as absorption features against the bright galactic background, contain thousands of solar masses of dense ($n \gtrsim 10^5$ cm^{-3}) and cold gas ($T \simeq 10 - 15$ K) and present typical sizes between 1–8 pc (Bergin

and Tafalla, 2007). They may represent the densest parts of GMCs and they are probably the birth sites for massive stars and clusters. Once a dense core in an IRDC starts to collapse, there is a large amount of gravitational energy released and a Hot Molecular Core (HMC) is formed. A HMC is considered the first protostellar stage of high-mass stars (e.g., Kurtz et al., 2000). They are compact ($\lesssim 0.1$ pc) and dense ($n \gtrsim 10^7$ cm^{-3}) objects with relatively high temperatures ($T \gtrsim 100$ K) and they are characterized by a rich chemistry of complex organic molecules (e.g., CH_3OH, CH_3OCHO, CH_3OCH_3, ...). As the temperature increases and the massive protostar reaches the hydrogen burning phase, the Lyman continuum photons ionize the surrounding medium and form a hypercompact HII (HCHII) region. The high-mass star formation timescale is so short that at this point the star is still surrounded by an envelope of dense material. When infall has decreased enough, the HCHII will begin to expand and evolve into an ultracompact HII (UCHII) region, characterized by sizes $\lesssim 0.1$ pc and densities $\gtrsim 10^4$ cm^{-3}, and later into a more evolved HII region (e.g., Hoare et al., 2007; Kurtz et al., 2000). The HII regions have temperatures around 10^4 K and produce a pressure difference between the ionized and the surrounding gas which causes the expansion of the ionized gas and pushes forward the surrounding material.

1.2 Radiation from molecules and dust

1.2.1 Molecular line emission

Molecules present 3 types of transitions, electronic, vibrational and rotational. For the typical densities and temperatures of molecular clouds, only the rotational transitions can be effectively excited. It is important to notice that molecules with null dipole moment cannot emit radiation through rotational transitions, which is the case of the homonuclear diatomic molecules such as H_2, C_2, N_2, etc. CO, for example, is an abundant molecule and a good tracer of the molecular gas.

Since star formation takes place in dense molecular cores, the densest regions of molecular clouds, the best tracers to study these regions are the so-called high-density molecular gas tracers. These are molecules with relatively high dipole moment.

To be able to observe a transition, the excitation temperature ($T_{\rm ex}$) must be higher than the background temperature ($T_{\rm bg}$), and the column density must be high enough. The line intensity can be written as

$$T_{\rm L} = (T_{\rm ex} - T_{\rm bg})(1 - e^{-\tau_v}), \tag{1.1}$$

where τ_v is the optical depth.

In order to study star formation, we are interested in dense cores with a certain range of densities and temperatures. For this we need molecular transitions with a critical density ($n_{\rm crit}$) between 10^3–10^8 cm^{-3}. For densities $n > n_{\rm crit}$, the excitation of the energy levels of a molecule is determined by collisions and follows a Boltzmann distribution. The critical density is defined by

$$n_{\rm crit} = \frac{A_{\rm ul}}{\gamma}, \tag{1.2}$$

where $A_{\rm ul}$ is the Einstein's spontaneous emission coefficient and γ is the collisional de-excitation coefficient. Some examples of molecular transitions with critical densities inside this range are hot-core tracer CH_3OH 5(1,4)–4(2,2), shock tracer SiO (5–4) and outflow tracer CO (2–1).

Molecular line emission information is important to obtain the velocity field of the dense material in addition to its physical structure. In addition, we can derive important physical parameters such as line widths, excitation temperatures and column densities. Molecular abundances also provide valuable information about the physical conditions and processes in the regions.

1.2.2 Dust thermal emission

The dust particles of about $\sim 0.01 - 1$ μm inside molecular clouds, efficiently absorb radiation at smaller wavelengths than their size and then reemit it as emission in the continuum. The resulting spectra is similar to the one of a black body modified by an absorption coefficient which depends on the frequency (gray body). The observed flux density at a specific frequency is given by

$$S_\nu = B_\nu(T_d)(1 - e^{-\tau_\nu})\Omega_S, \tag{1.3}$$

where $B_\nu(T_d)$ is the Plank function at the isothermal dust temperature T_d, Ω_S is the solid angle of the source and τ_ν is the optical depth.

At millimeter and submillimeter wavelengths the dust emission is optically thin and therefore it is a good tracer of the column density of the molecular cloud. Thus, from the dust continuum emission we can estimate the gas+dust mass based on

$$M = R\frac{d^2 S_\nu}{B_\nu(T_d)\kappa_\nu}, \tag{1.4}$$

where d is the distance to the source, κ_ν is the dust opacity and the factor R is the gas-to-dust ratio which we assume to be 100. κ_ν is related to τ_ν by $\tau_\nu = \kappa_\nu \int_{\rm los} \rho dl$, where the integral

is the gas+dust mass column density. The flux density S_ν can be given in units of Jansky (Jy; 1 Jy = 10^{-23} erg s^{-1} cm^{-2} Hz^{-1}).

In addition, as the dust thermal emission is polarized, we can extract information about the magnetic field. It is well accepted that the dust grains have a non-spherical structure and that their longest axes are aligned perpendicular to the magnetic field direction (see Hildebrand et al., 2000, for a review). The orientation of the magnetic field on the plane of the sky can then be inferred by rotating the dust linear polarization (i.e., electric field) by 90°.

1.3 Magnetic field observations

In the last years it has been studied that the magnetic field plays an important role in the formation of stars acting as a support mechanism against gravitational collapse. Previous observations have shown that the magnetic field morphology from Galactic to molecular core scales seems to be coherent, suggesting that the magnetic energy is not negligible. The orientation of the field can either be along filamentary structures, which suggests that matter is contained in magnetic flux tubes, or perpendicular, suggesting contraction along the magnetic field lines (see Crutcher, 2012; Li et al., 2014, for reviews).

Magnetic field and turbulence are the main forces that can counteract gravity and prevent the gravitational collapse. To estimate the relevance of the magnetic field, the Alfvén Mach number ($\mathscr{M}_A$) and the mass-to-flux ratio (M/Φ_B) parameters are used to compare the magnetic field strength with the turbulence and gravity, respectively (see Sec. 1.4). Moreover, an estimation of the magnetic field strength on the plane of the sky from dust polarization observations can be performed using the Chandrasekhar-Fermi technique (Chandrasekhar and Fermi, 1953), for which the projection of the mean magnetic field on the plane of the sky, B_p, can be written as

$$B_p = (4\pi\bar{\rho})^{1/2}\frac{|\delta v|}{|(\delta B/B_p)|}, \tag{1.5}$$

where $\bar{\rho}$ is the mean mass density and δv and δB are the components of the velocity and magnetic field perturbations on the plane of the sky transverse to B_p, respectively. When the dispersion of the polarization angles ($\delta\phi$) is $< 25°$, the Chandrasekhar-Fermi equation can be approximated as

$$B_p = 0.5\sqrt{4\pi\bar{\rho}}\,\delta v_{\rm los}\,\delta\phi^{-1}, \tag{1.6}$$

where $\delta v_{\rm los}$ is the velocity dispersion in the line of sight and $\delta\phi$ is the dispersion of the polarization angles (Ostriker et al., 2001).

To study the importance of the magnetic field at core scales ($\lesssim 0.1$ pc), polarization observations of dust continuum emission and the observation of gas kinematics by molecular line tracers are required at high-angular resolution. This is essential to trace both gravity and gas dynamics and be able to compare them with the magnetic field at the same spatial scales. Such studies towards low- and high-mass star-forming regions are only available from very limited case studies (e.g., Girart et al., 2009, 2006; Liu et al., 2016; Tang et al., 2009a,b).

Previous studies towards low- and high-mass star-forming regions show that the magnetic field plays an important role in their evolution and presents an hourglass morphology when gravity has overcome the magnetic support (e.g., Girart et al., 2009, 2006; Liu et al., 2016; Qiu et al., 2013, 2014; Tang et al., 2009b, 2013). However, a few cases show the magnetic field significantly tangled or with a morphology that indicates that the magnetic force has been overcome, not only by gravity, but by other processes, such as stellar feedback (e.g., G5.89-0.39, NGC 7538 IRS1: Frau et al., 2014; Tang et al., 2009a) or by a combination of turbulence and angular momentum (e.g., DR 21(OH): Girart et al., 2013).

Zhang et al. (2014) analyze the overall results towards 14 high-mass star-forming regions and provide important statistical results. They find that magnetic fields at core scales ($0.01 - 0.1$ pc) are either aligned or perpendicular to the parsec-scale magnetic fields showing that the magnetic field plays an important role during the collapse and fragmentation of parsec-scale clumps, and the formation of dense cores. Also, the outflow axis appears to be randomly oriented with respect to the magnetic field in the core, suggesting that at the scale of accretion disks ($\lesssim 10^3$ au), angular momentum and dynamic interactions dominate over magnetic fields.

1.4 Collapse models in star-forming regions

Important theoretical work has been done to analytically and numerically model the star formation process. Different scenarios have been proposed through the years. In this Section, we introduce some of these models.

1.4.1 Larson and Shu models

Larson (1969) and Shu et al. (1987) models are well established to explain the formation of low-mass stars (< 8 M$_\odot$). These models are useful for isolated cores and provided the cores self-gravity and thermal pressures are dominant over all other forces.

A condensation of gas in the molecular cloud becomes unstable to gravitational collapse if the mass is large enough so that gravity dominates over other forces. The critical mass for

this to happen is the Jeans mass and its given by

$$\left[\frac{M_{\rm J}}{M_\odot}\right] = 5\left[\frac{T_{\rm k}}{\rm K}\right]^{3/2}\left[\frac{n}{\rm cm^{-3}}\right]^{-1/2}, \tag{1.7}$$

where $T_{\rm k}$ and n are the kinetic temperature and density, respectively. Initially, the collapse is isothermal, as the energy generated is easily radiated in the far infrared. When the density increases up to densities of $\sim 10^{10}$ cm^{-3} the gas becomes optically thick and the energy cannot be radiated, increasing the temperature and pressure which stops the collapse and a first hydrostatic core (FHSC) is formed (Larson, 1969). When the temperature reaches $\sim$2,000 K, the dissociation of the H_2 molecules occurs. The dissociation of H_2 consumes energy and the collapse can continue. When all H_2 is dissociated, the pre-stellar phase finishes and the protostar is formed. During the main accretion phase, the luminosity of the protostar comes from the kinetic energy of the infalling material from the surrounding envelope. In Larson's model, the infall velocity, density and temperature distributions of the envelope are given by

$$v \propto r^{-1/2}, \quad \rho \propto r^{-3/2} \quad \text{and} \quad T \propto r^{-1/2}. \tag{1.8}$$

As the mass of the core grows, the velocity of the infalling material gets higher, which increases the luminosity of the protostar. For a 1 $M_\odot$ dense core, the maximum luminosity is achieved when the accreted mass is 0.5 $M_\odot$. Then, the luminosity decreases as the mass accretion rate slows down due to the lower density of the infalling material. When almost the entire envelope has been accreted, the pre-main sequence object becomes visible. At this stage, the luminosity of the object comes from the slow contraction of the core. The contraction continues until the fusion reaction of hydrogen begins and the object reaches the main sequence.

Shu's model assumes a density distribution following $\rho \propto r^{-2}$. The collapse is initiated at the center of the sphere, and the radius, at which the gas begins to fall, propagates outward at the sound speed ("inside out collapse"). Despite the different initial conditions adopted by Shu et al., in the last stages, when the collapse has reached the outer layers, the density and velocity distributions are indistinguishable from Larson's.

The formation of high-mass stars ($M \gtrsim 8$ $M_\odot$) presents some theoretical problems. This is mainly because the star begins its main sequence phase when it has not finished accreting all its mass yet and the radiation pressure from the newly-born star disperses the infalling material. The Kelvin-Helmholtz time describes the characteristic time of the gravitational

contraction of the protostar:

$$t_{\rm KH} \simeq \frac{GM_*^2}{R_* L_*}, \tag{1.9}$$

where G is the gravitational constant and M_*, R_* and L_* are the mass, radius and luminosity of the protostar, respectively. This time is considerably shorter for massive stars. For example, $\sim 10^4$ years for a 50 $M_\odot$ star and $\sim 3\times10^7$ years for a 1 $M_\odot$ star. On the other hand, the period of accretion of the envelope, given by the free-fall time

$$t_{\rm ff} \simeq \left(\frac{3\pi}{32G\rho}\right)^{1/2}, \tag{1.10}$$

is determined by the density ρ and is similar for low- and high-mass stars. For typical densities of $\sim 10^4$ cm^{-3}, the timescale is $\sim 4\times10^5$ years. Thus, for massive stars, $t_{\rm KH} < t_{\rm ff}$.

Different mechanisms have been proposed to explain the formation of high-mass stars. One of the models, called *monolithic collapse*, is a scaled-up version of the low-mass star model. The cavity generated by the jet would permit the radiation pressure to escape without hindering the accretion through the protostellar disk (e.g., Krumholz et al., 2005; McKee and Tan, 2002). Furthermore, high-accretion rates ($\gtrsim 10^{-3}$ $M_\odot$ yr^{-1}) could also help to avoid the radiation pressure problem (e.g., Banerjee and Pudritz, 2007). Observations of massive objects showing evidence of an ongoing accretion process (e.g., Beltrán et al., 2006; Patel et al., 2005) and high-accretion rates (e.g., Zapata et al., 2008) support this scenario. Another way of gathering more mass is by *competitive accretion*. High-mass stars are usually found in clusters. Inside a cluster, lower-mass stars accrete mass from their surroundings. The material would fall into the potential well of the whole stellar cluster, where the massive star is forming, increasing the gas reservoir for the individual star (e.g., Bonnell and Bate, 2006; Bonnell et al., 1997, 2001). In addition, for high protostellar densities ($> 10^6 - 10^8$ pc^{-3}) the merging of two or more low-mass stars can also be the mechanism for the formation of the most massive stars (e.g., Bonnell et al., 1998).

1.4.2 Ambipolar diffusion

Mestel and Spitzer (1956) were one of the firsts authors to discuss the effect of magnetic fields in the star formation process. In their work they showed that, as long as the magnetic field was frozen into the contracting cloud, the magnetic field pressure could prevent gravitational collapse. This work was followed by Mouschovias and Spitzer (1976) who proposed that magnetic forces would prevent a cloud from collapsing if

$$M/\Phi_B < (M/\Phi_B)_{\rm cr}, \tag{1.11}$$

where M is its mass and $\Phi_B = \pi < B > R^2$ is the magnetic flux through it. If the cloud's mass-to-flux ratio is below a critical value (magnetically subcritical) the magnetic support would prevent the collapse. This critical value is given by $(M/\Phi_B)_{\rm cr} = 1/(2\pi G^{1/2})$ (Nakano and Nakamura, 1978), where G is the gravitational constant.

These early studies assume that the magnetic field is frozen into the gas, but for this to happen, the gas must be sufficiently ionized. However, observational studies have shown that the gas in star-forming regions is weakly ionized (e.g., Caselli et al., 1998). In a partially ionized gas, the neutral particles are able to separate or diffuse through the ions and therefore through the magnetic field that is tied to the ions. This process is called *ambipolar diffusion* and Mestel and Spitzer (1956) proposed this as an important process favoring star formation.

Previous studies considered molecular clouds to have strongly magnetically subcritical mass-to-flux ratios (e.g., Mouschovias, 1991), implying that the time for the cores to become supercritical was very long, of the order of $10-20$ times larger than the clouds' free-fall time (e.g., Ciolek and Mouschovias, 1994). However, more recent studies have suggested that molecular clouds and their clumps are close to being magnetically critical with a moderate preference for being supercritical (Bourke et al., 2001; Troland and Crutcher, 2008). Furthermore, the mean molecular weight of ions (μ_i) has been found to be systematically lower than the usually assumed value of 20–30, approaching values of 3 at high densities. The considerably lower value of μ_i implies that ambipolar diffusion operates faster than previously thought (Tassis et al., 2012).

1.4.3 Turbulent clouds

The nature of the motions generating the supersonic line widths observed in molecular clouds and their substructures is a matter of debate. They were initially proposed to be caused by gravitational contraction by Goldreich and Kwan (1974). This was soon discarded by Zuckerman and Palmer (1974) who showed that this would imply a star formation rate (SFR) two orders of magnitude larger than the observed. Instead, they proposed that the observed supersonic line widths were produced by random small-scale supersonic turbulence and that local turbulence acts as a source of isotropic pressure which provides support to the clouds against self-gravity allowing a state of near hydrostatic equilibrium (e.g., McKee and Tan, 2003). However, this is an oversimplification of the true nature of turbulence.

Nowadays, several studies have shown that supersonic turbulent motions of a given size have a dual role in star formation. While it provides support against gravitational collapse towards scales larger than their own scale (e.g., Bonazzola et al., 1987; Chandrasekhar, 1951; McKee and Tan, 2003), it promotes the collapse at smaller scales (e.g., Padoan, 1995; Vázquez-Semadeni et al., 2003).

However, the turbulent scenario presents some problems. Numerical simulations suggest that molecular cloud turbulence dissipates in much less than the cloud lifetime, even in the presence of strong magnetic fields (e.g., Padoan and Nordlund, 1999; Stone et al., 1998). On the other hand, even though stellar feedback has been proposed as a source of turbulence in molecular clouds, it is not clear if it could disrupt the cloud before its mass is completely converted into stars (see Vázquez-Semadeni et al., 2010). In addition, the estimate of the SFR by Zuckerman & Palmer was performed assuming that the collapse is spherically symmetric and monolithic, something which is clearly not observed. Also, the implication of excessively large SFR in a collapsing cloud can be solved if the clouds are destroyed early in their life cycle by the stellar feedback and only a small fraction of their mass is converted into stars (e.g., Franco et al., 1994; Whitworth, 1979).

There are two crucial parameters for the study of turbulence in star-forming regions. First, the sonic mach number ($\mathscr{M}$) compares the 3D turbulent velocity dispersion ($\sigma_{\rm 3D,nth}$) relative to the isothermal sound speed of the medium (c_s),

$$\mathscr{M} = \frac{\sigma_{\rm 3D,nth}}{c_s}, \tag{1.12}$$

where $\sigma_{\rm 3D,nth} = \sqrt{3}\sigma_{\rm 1D,nth}$ and $c_s = \sqrt{k_{\rm B}\,T/\mu}$, where $k_{\rm B}$ is the Boltzmann constant, T is the temperature, and μ is the mean molecular mass.

Second, the Alfvén mach number ($\mathscr{M}_A$) compares the turbulence with the magnetic energy (sub- or super-Alfvénic):

$$\mathscr{M}_A = \frac{\sigma_{\rm 3D,nth}}{V_A}, \tag{1.13}$$

where $V_A = B/\sqrt{4\pi\rho}$ is the Alfvén speed at density ρ and B is the strength of the magnetic field. Thus, if a region is super-Alfvénic, the turbulent kinetic energy dominates over the magnetic pressure.

1.4.4 Global hierarchical collapse

The lack of stars of ages > 5 Myr (post-T Tauri stars) and the presence of newly formed stars in nearby molecular clouds is understood if molecular clouds have evolutionary lifetimes of a few megayears. This creates problems, as it is difficult to understand how large regions (~ 20 pc) with small velocity dispersions (~ 2 km s^{-1}) can form stars almost simultaneously throughout the cloud (Ballesteros-Paredes et al., 1999a).

If the lifetime of molecular clouds is short (several Myr), there is no need for them to maintain a quasi-equilibrium state, and it is not necessary for the turbulence to be regenerated (e.g., Ballesteros-Paredes et al., 1999b; Hartmann et al., 2001). The restrictions placed

on cloud lifetimes by stellar populations suggest that the evolution from dispersed molecular gas to protostellar cores is dynamic rather than quasi-static (e.g., Ballesteros-Paredes et al., 1999a; Hartmann et al., 2001; Klessen et al., 2000).

On the other hand, recent structural properties of clusters or groups of young stars still require an adequate theoretical model. One of these properties is the existence of a mass segregation in the clusters, with the most massive stars located towards the center of the cluster (Hillenbrand and Hartmann, 1998). A second property is the possibility of an age gradient in clusters, with the youngest stars located in the highest density regions (Kuhn et al., 2015). A global, hierarchical collapse scenario can provide a unified explanation for these properties (e.g., Vázquez-Semadeni et al., 2009). In this dynamical scheme, large-scale turbulent streams would form and collide, collecting the material they are advecting (e.g., Ballesteros-Paredes et al., 1999b; Vazquez-Semadeni et al., 1995). The warm, atomic gas undergoes a transition to the cold, dense atomic phase which becomes Jeans-unstable (Hartmann et al., 2001) and begin to collapse *globally* (e.g., Audit and Hennebelle, 2005; Heitsch and Hartmann, 2008). In this scenario, the non-thermal motions of molecular clouds, instead of consisting of random, small-scale isotropic motions that can act as pressure, would be dominated by inward motions, caused by the gravitational collapse, and the collapse would occur both at large and small scales in a *hierarchical* manner (e.g., Ballesteros-Paredes et al., 1999a; Vázquez-Semadeni et al., 2009). This would imply that the cloud would not be supported by turbulence against its self-gravity.

This scenario predicts that the SFR increases over time, as a consequence of the increase of the mean density as the molecular cloud experiences global gravitational collapse (e.g., Zamora-Avilés and Vázquez-Semadeni, 2014; Zamora-Avilés et al., 2012). Assuming that massive stars do not form until the SFR is high-enough that the initial mass function (IMF) is also sufficiently high, massive stars would form later than low-mass stars, and when they do, they would start to disrupt their parent cloud through stellar feedback, lowering back the SFR (e.g., Colín et al., 2013; Dale et al., 2015; Vazquez-Semadeni et al., 2016; Zamora-Avilés and Vázquez-Semadeni, 2014). Observational evidence favoring the increase of the SFR in molecular clouds has been found by e.g., Palla and Stahler (2000) and Beccari et al. (2010), that found that only a small fraction of the stars in young clusters are older than several Myr old.

Numerical simulations of cloud formation in the interstellar medium and in star-forming clouds also support this scenario showing that the velocity fields are in general organized at all scales, with a continuity from large scales to the interiors of clumps (e.g., Ballesteros-Paredes et al., 1999a,b; Heitsch et al., 2001; Vazquez-Semadeni et al., 1996). On the other hand, low-angular resolution molecular line surveys of star-forming regions also show evi-

dence of large-scale ($\sim 0.3 - 1$ pc) contraction (e.g., Klaassen and Wilson, 2008), which higher-angular resolution observations associate with rotation and inflow motions. Moreover, accretion flows are also seen on smaller scales (~ 0.1 pc) around individual regions (e.g., Csengeri et al., 2011; Galván-Madrid et al., 2010).

1.5 The aim and structure of the thesis

1.5.1 Goal of the thesis

As we have seen, turbulence, magnetic fields and gravity driven flows are important for the formation of new stars. Although magnetic fields have been proven to be important in the formation of stars, only a few works have been performed combining magnetic field and kinematic information (e.g., Girart et al., 2013; Zhang et al., 2014). Such studies are important to analyze both gravity and gas dynamics and be able to compare them with the magnetic field. In this thesis we will combine dust polarization studies with kinematic analysis towards different star-forming regions. We aim to study the physical properties at core scales ($\lesssim 0.1$ pc), from molecular line and dust (total and polarized) emission, and study the role of the magnetic field in their dynamic evolution. For this, we will use millimeter and submillimeter observational data taken towards low- and high-mass star-forming regions in different environments and evolutionary states.

1.5.2 Approach and strategy

Star-forming regions are located at the densest parts of molecular clouds. To be able to observe the embedded dense cores, long-wavelength high-angular resolution observations are needed. In this work we have used observational data from the Plateau de Bure (PdBI) and the Submillimeter Array (SMA) radio-interferometers. In addition, we have used the single-dish IRAM 30m telescope which recovers extended emission. From the obtained data we have studied the thermal dust continuum emission and the molecular line emission from their rotational electronic transitions. The dust continuum emission allows us to study the structure and physical properties of the cores such as mass, column density, etc. As the dust continuum emission is polarized, it also provides magnetic field information. On the other hand, the molecular line emission provides the kinematic information of the gas; we can also derive the column density, mass and other properties associated to the gas.

To carry out the goal of this thesis we have studied three regions in different physical and chemical conditions: an isolated pre-stellar core in a quiescent magnetized environment

in the Pipe nebula, a high-mass star-forming region in a more evolved evolutionary state called NGC 6334 V, and a highly-fragmented lower-mass region called L1287.

1.5.3 Outline of the thesis and status of the different works

In the following, we describe the different parts that constitute the thesis and explain the status of each work.

In Chapter 2 we present the work done towards FeSt 1-457, a pre-stellar core located in a magnetized environment in the "bowl" region of the Pipe nebula. The region was observed with the PdBI and the IRAM 30m telescope at 3 mm. This work, entitled *A correlation between chemistry, polarization, and dust properties in the Pipe nebula starless core FeSt 1-457*, and authored by C. Juárez, J.M. Girart, P. Frau, A. Palau, R. Estalella, O. Morata, F. O. Alves, M. T. Beltrán, and M. Padovani, appeared in Astronomy & Astrophysics, 2017, volume 597, page A74.

In Chapter 3 we show the spectro-polarimetric results from the intermediate/high-mass star-forming region called NGC 6334 V. The observations were done at 870 μm and are part of the Legacy project of polarization carried out with the SMA. This work, entitled *Magnetized converging flows towards the hot core in the intermediate/high-mass star-forming region NGC 6334 V*, and authored by C. Juárez, J.M. Girart, M. Zamora-Avilés, Y.-W. Tang, P. Koch, H. B. Liu, A. Palau, J. Ballesteros-Paredes, Q. Zhang, and K. Qiu, has been submitted for publication to the Astrophysical Journal.

In Chapter 4 we study a lower-mass region observed with the SMA at 1.3 mm, L1287. Images from *Herschel* towards the region show a $\sim$ 10 pc scale filament with L1287 located approximately at the center and being the main star-forming site of the filament. This work is currently in preparation for publication and will be submitted to Astronomy & Astrophysics.

Finally, in Chapter 5 we discuss the global results and summarize the main conclusions derived from this work.

Chapter 2

A correlation between chemistry, polarization and dust properties in the Pipe nebula starless core FeSt 1-457

2.1 General overview

Pre-stellar cores within molecular clouds constitute the stage previous to the star formation process. They provide the very initial conditions in which stars are formed. They are typically cold ($\leq$ 10 K) with temperature gradients decreasing towards the center (e.g., Launhardt et al., 2013; Ruoskanen et al., 2011; Wilcock et al., 2012), and densities $> 10^4$ cm^{-3}, with a chemistry affected by molecular freeze-out onto dust grains (e.g., Marsh et al., 2014; Tafalla et al., 2002). Their physical structure can be well explained through a Bonnor-Ebert profile (Bonnor, 1956; Ebert, 1955), i.e., the profile corresponding to an isothermal gas sphere in hydrostatic equilibrium (e.g., Evans et al., 2001; Kandori et al., 2005; Roy et al., 2014). However, their density and temperature gradient structures are still under debate (e.g., Hardegree-Ullman et al., 2013; Sipilä et al., 2011) and the implications of heavy molecular depletion on other physical properties, such as dust grain properties and polarization, are not clear.

FeSt 1-457 (Feitzinger and Stuewe, 1984), also known as Core 109 in Lombardi et al. (2006) catalogue, is a prototypical starless core, as previous studies have shown that this core is quiescent with no IRAS nor Spitzer Space Telescope point sources associated (Ascenso et al., 2013; Forbrich et al., 2015, 2009). Indeed, the internal luminosity, estimated using the non-detection from the 70 μm *Herschel*[1] image ($3 \times \mathrm{rms} = 0.02$ Jy pixel^{-1}) and using

[1] *Herschel* is an ESA space observatory with science instruments provided by European-led Principal Investigator consortia and with important participation from NASA.

the relation between the 70 μm flux and the internal luminosity (Dunham et al., 2008), is $L_{int} < 0.004\ L_{\odot}$. It is also the most chemically evolved starless core among those isolated, embedded in the most pristine part of the Pipe nebula, the bowl, at a distance of 145 pc (Alves and Franco, 2007). Frau et al. (2015) suggest the presence of two filaments with north-south and east-west directions colliding along the northwest-southeast direction at the bowl region, just where FeSt 1-457 is located.

Frau et al. (2012a) carried out a 15 GHz bandwidth molecular survey at 3 mm towards FeSt 1-457 with the Institute of Millimeter Radioastronomy (IRAM) 30m telescope. They find a rich chemistry (especially compared with most of the other Pipe starless cores): many lines are detected from early- (C_3H_2, HCN, CS, $C^{34}S$ and CN) and late-time (N_2H^+, N_2D^+ and DCO^+) molecules, suggesting that FeSt 1-457 is an evolved starless core. Aguti et al. (2007) observed the 3 mm lines of N_2H^+, HCO^+, CS and $C^{18}O$ with the IRAM 30m. They find evidence of CO and HCO^+ depletion in the center of the core. However, the N_2H^+ $(1-0)$ may be undepleted to depths of $\lesssim 40$ mag of visual extinction.

FeSt 1-457 has a mass of $\sim 4\ M_{\odot}$ (Frau et al., 2010; Román-Zúñiga et al., 2010), quasi spherical and compact structure and shows signs of gravitational instability (Frau et al., 2010; Kandori et al., 2005). Aguti et al. (2007) find that FeSt 1-457 might be pulsating, based on expansions of the outer layers. However, their Jeans mass measurement is compatible with the mass of the core and they propose a quasi-stable state near hydrodynamic equilibrium.

The core is embedded in a magnetised medium (Alves et al., 2008, 2014; Franco et al., 2010), which suggests that the magnetic field could be a source of external support. Alves et al. (2014), in a multi scale polarization study towards FeSt 1-457, find a polarization 'hole' for radii $\lesssim 55''$ which they propose to be the result of loss of grain alignment with the magnetic field due to the lack of an internal source of radiation.

In this Chapter we study the starless core FeSt 1-457 through N_2H^+ $(1-0)$ observations obtained with the IRAM 30m and Plateau de Bure Interferometer (PdBI) telescopes[2]. N_2H^+ is known to be a very good tracer of the densest inner parts of dense cores as it is not expected to be depleted until densities $> 10^5$ cm^{-3} (e.g., Bergin and Tafalla, 2007). In addition, we present mapping information of 15 molecular lines detected at 3 mm within a frequency range spanning 30 GHz obtained with the IRAM 30m which allowed us also to perform a detailed study of the abundance radial profiles and to relate them to the known grain growth and depolarization in the center.

[2]IRAM is supported by INSU/CNRS (France), MPG (Germany) and IGN (Spain).

2.2 Observations

2.2.1 IRAM 30m

Line observations

The observations were carried out on July 2012 at the IRAM 30m telescope in Granada, Spain. We used the Eight MIxer Receiver (EMIR) in the E090 configuration. The backend used was the FTS spectrometer with a channel resolution of 195 kHz (0.6 km s^{-1} at 3 mm), which provided a total bandwidth of 30 GHz covering the frequency ranges from 78.6 to 86.4 GHz, from 87.6 to 102.0 GHz and from 103.2 to 111.0 GHz (see Table 2.1). In addition, the VESPA (Versatile Spectrometer Array) correlator was used simultaneously with the FTS in order to observe the N_2H^+ (1−0) line with a better channel resolution, 20 kHz (corresponding to 0.063 km s^{-1}), with a total bandwidth of 40 MHz. The observations were done using the frequency-switching mode with a frequency throw of ∼7 MHz. The maps were done in on-the-fly (OTF) mode covering a region of 4.5 arcmin × 4.5 arcmin centered at RA(J2000)= $17^h35^m47.70^s$, Dec(J2000)= $-25°32'52.9''$. In the OTF mode, the maps were done with scans either along the right ascension or either along the declination (with Nyquist separation between scans). This allows to have a better sampling on the observed region. The maps were combined and regrided to have a final pixel size of $6''$. Pointing and focusing were done following the recommended procedure at the telescope, which should give a pointing accuracy of $\sim 2''$. Absolute calibration accuracy with EMIR is better than 10%. We present the spectra in main beam brightness temperature scale, which was obtained by using the efficiencies reported on the IRAM website. The weather conditions were good with system temperatures of 125–192 K and zenith opacities around 0.07. The reduction of the final maps and most of the figures have been done with the GILDAS[3] software. Given the highly distorted baselines generated in the frequency switching mode, the spectral baselines were subtracted only over a small frequency range around a given line. The typical rms noise per channel for the VESPA spectral map is $\Delta T_{\rm mb} \simeq 0.18$ K. The half power beam width (HPBW) for each frequency is given in Table 2.1.

Continuum observations

FeSt 1-457 was observed on April and May 2009 and on January 2010 with the 117-receiver Max-Planck Millimetre Bolometer (MAMBO-II) of the IRAM 30m telescope (previously described in Frau et al., 2010).

[3] http://www.iram.fr/IRAMFR/GILDAS/

Table 2.1 FTS molecular transitions.

Molecule	Transition	Frequency (GHz)	HPBW[a] ($''$)	E_U[b] (K)	n_{crit}[c] (cm^{-3})
U[d]	–	80.5599	30.5	–	–
HC_3N	(9−8)	81.8816	30.0	19.6	4.2×10^5
C_3H_2	$(2_{0,2}-1_{1,1})$	82.0935	30.0	6.4	–
C_3H_2	$(2_{1,2}-1_{0,1})$	85.3388	28.8	6.4	–
C_4H	(9−8, J=17/2−15/2)	85.6725	28.7	4.1	–
NH_2D	$(1_{1,1}-1_{0,1})$	85.9262	28.6	20.7	–
$H^{13}CN$	(1−0)	86.3399	28.5	4.1	2.0×10^6
HCN	(1−0)	88.6318	27.8	4.2	2.2×10^6
HCO^+	(1−0)	89.1885	27.6	4.3	1.6×10^5
HNC	(1−0)	90.6635	27.1	4.4	2.8×10^5
N_2H^+	(1−0)	93.1734	26.4	4.5	1.4×10^5
$C^{34}S$	(2−1)	96.4129	25.5	6.2	–
CH_3OH	$(2_{-1,2}-1_{-1,1})$	96.7393	25.4	12.5	–
CH_3OH	$(2_{0,2}-1_{0,1})$	96.7413	25.4	7.0	–
^{34}SO	(3_2-2_1)	97.7153	25.2	9.1	–
CS	(2−1)	97.9809	25.1	7.1	3.3×10^5
SO	(3_2-2_1)	99.2998	24.8	9.2	–
HC_3N	(11−10)	100.076	24.6	28.8	8.8×10^5
$C^{18}O$	(1−0)	109.7821	22.3	5.3	1.9×10^3
U[d]	–	109.9531	22.4	–	–
^{13}CO	(1−0)	110.2013	22.3	5.3	1.9×10^3

[a] $[\mathrm{HPBW}/('')] = 2460\times[\mathrm{freq/GHz}]^{-1}$.

[b] E_U is the energy of the upper level of the transition.

[c] $n_{crit}=A_{ul}/\gamma$, where A_{ul} is the Einstein spontaneous emission coefficient and $\gamma=\sigma<v>$ is the collisional rate where σ is the cross section of the collision for each transition and $<v>\approx(3kT/m)^{1/2}$ is the average velocity of the collisional particles. As H_2 is the most abundant molecule it is used as the dominant collisional particle. We assume T=10 K. The Einstein spontaneous emission coefficients and γ values are taken from LAMDA database (http://home.strw.leidenuniv.nl/∼moldata/).

[d] Unidentified line.

2.2.2 PdBI

The PdBI observations of N_2H^+ (1−0) were performed on several runs in October and November 2011, and March 2012, in the C array configuration, which provides a baseline range from 24 m to 176 m (7.5–55 kλ at 3.2 mm). The observations were done in mosaic mode with an hexagonal pattern of 12 pointings and with a separation of $\sim 18''$. This allows to uniformly cover an area of $\sim 102'' \times 102''$ centered on RA(J2000)= $17^h35^m47.804^s$, Dec(J2000)= $-25°33'01.10''$. The primary beam at 3.2 mm is $\sim 54''$. The quasars J1733−130 and J1743−169 were used as gain calibrators and 3C273, J2015+371, 3C454.3 and J1751+096 as bandpass calibrators. Absolute flux calibration was performed on MWC349 and on the suitable solar system object available at the time of the observations. The absolute flux accuracy is ∼10%. The N_2H^+ (1−0) line was observed in a spectral window of 20 MHz with 512 channels, which provides a spectral resolution of 0.039 MHz (0.125 km s^{-1}). The system temperatures and the precipitable water vapor values were between $\sim$ 100–300 K and $\sim$ 2–6 mm respectively. The data were reduced using CLIC and MAPPING packages of the GILDAS software using the standard procedures. The rms noise per channel achieved was 25 mJy $beam^{-1}$. The synthesized beam was $10.6'' \times 5.7''$, with a P.A. of 11.94°.

2.2.3 PdBI+IRAM 30m

We combined the N_2H^+ single dish data taken with the IRAM 30m telescope (with an rms noise per channel of $\sim$ 180 mK) with the PdBI data (rms noise per channel of $\sim$ 53 mK) to add the short-spacing information not detected by the millimetre interferometer. We used the short-spacing processing widget of the MAPPING package of the GILDAS software which produces visibilities from the single dish observations with the PdBI spectral resolution and merges them with the PdBI data. After trying different single dish weight factors, we found the best value to be 0.1. This value was the best compromise between adding excessive noise from the PdBI data due to the weak signal and giving to much weight to the single dish data not being able to see the contribution of the interferometer data.

When creating the dirty map we used a *uv*-taper of 65 m (20.3 kλ) to avoid the noise contribution of the longer *uv*-distances and to obtain a good signal-to-noise ratio. For the cleaning process we used the Steer, Dewdney and Ito (SDI) algorithm (Steer et al., 1984) to improve some strips that appeared using the Högbom algorithm due to the extended emission. The velocity resolution of the channel maps was 0.12 km s^{-1} as in the PdBI observations and the cutoff value to stop the cleaning was 1.5 times the rms, 0.06 Jy $beam^{-1}$. The synthesized beam was $10.78'' \times 6.11''$, with a P.A. of 11°.

2.2.4 Extinction data

We have made use of the high angular resolution extinction maps by Román-Zúñiga et al. (2010, 2009). These maps were constructed from a concerted deep near-infrared imaging survey using several telescopes (ESO-VLT, ESO-NTT and CAHA 3.5 m) as well as the 2MASS data. These maps have a resolution three times higher than the previous extinction map of this cloud by Lombardi et al. (2006), allowing to resolve structures down to ∼2,000 au.

2.3 Results

2.3.1 N_2H^+ (1−0)

VESPA IRAM 30m

In Fig. 2.1a we present the moment-zero map (i.e., velocity integrated intensity map) of the N_2H^+ line emission observed with the IRAM 30m telescope. The moment-zero emission was computed in the $4-8$ km s^{-1} velocity range, which covers the three central hyperfine lines. The structure is compact with a size of $\sim 2'$ (∼19,000 au) and the intensity increases towards the center of the map up to 2 K km s^{-1}.

In order to infer the physical and chemical properties in FeSt 1-457 from the N_2H^+ (1−0) IRAM 30m data, we used the HfS tool[4] (Estalella, 2016) to fit the hyperfine structure of our spectra. With the HfS_fit_cube procedure we could fit all the spectra of our data cube pixel-by-pixel. The fit was done only for the spectra with a peak intensity larger than five times the rms noise. We obtained the physical parameters $v_{\rm LSR}$, Δv and τ and derived the excitation temperature $T_{\rm ex}$ and the column density N following Caselli et al. (2002).

The procedure used for fitting the hyperfine structure of N_2H^+ (1–0) assumes local thermodynamic equilibrium (LTE) for all the seven hyperfine lines of the transition. However, it has been found that the hyperfine lines F_1, F=1,0→1,1 and 1,2→1,2 can be out of LTE. This is the case of the quiescent core L1512, where these excitation anomalies are attributed to collisional pumping, if the collisional coefficients of the hyperfines were different, or to radiative trapping effects depending on the different optical depth of the hyperfines (Caselli et al., 1995; Daniel et al., 2006). Thus, in order to avoid this problem, we performed the fit of the hyperfine structure of N_2H^+ (1–0) using only the five hyperfine components without excitation anomalies. In Fig. 2.2 and Table 2.2 we show the results from the fit for six selected positions (shown in Fig. 2.1c) of FeSt 1-457. As can be seen in Fig. 2.2, although

[4] http://ascl.net/1607.011

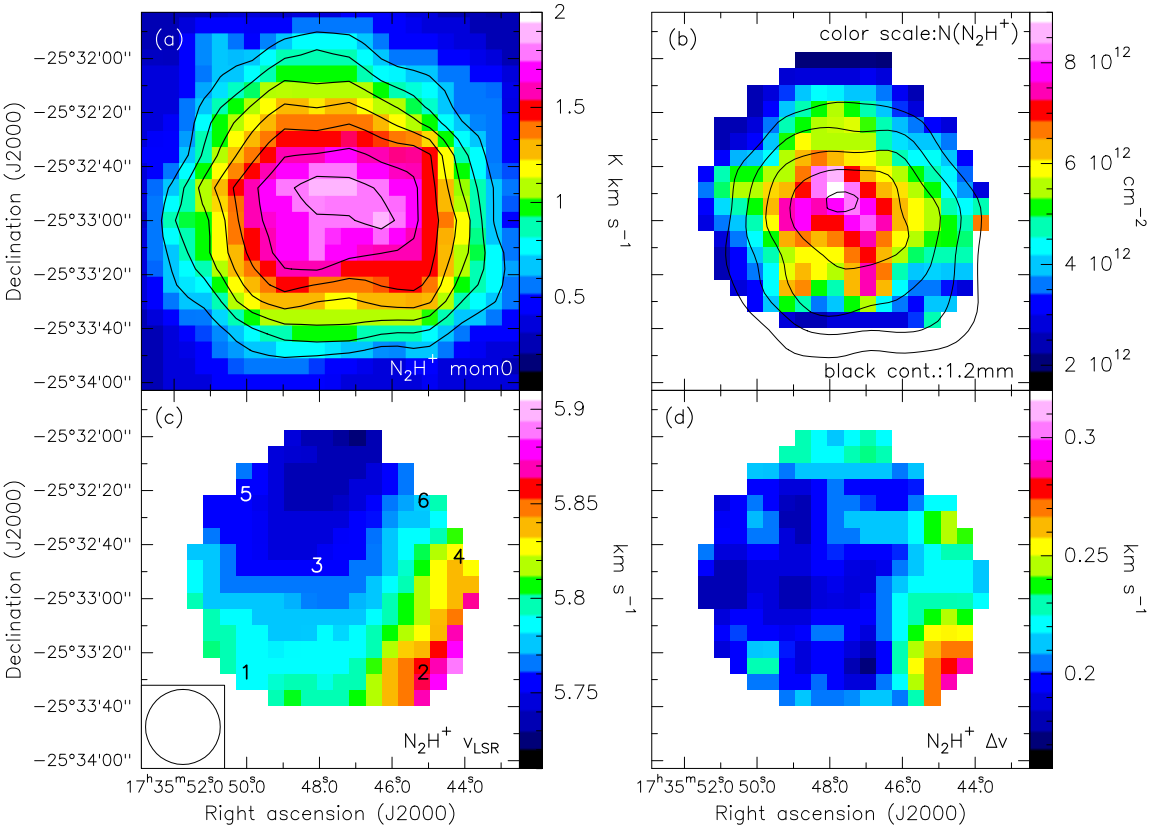

Fig. 2.1 N_2H^+ (1−0) IRAM 30m VESPA data. *Panel (a)*: Moment-zero map (using the three central hyperfine lines) of the IRAM 30m data. Contours are 35, 45, ..., 95 percent of the value of the peak, 1.9 K km s^{-1}. *Panel (b)*: Color scale: column density map. Black contours: IRAM 30m MAMBO-II 1.2 mm dust continuum emission at an angular resolution of 21″. Contour levels are 30, 40, 50, 60, 70 and 80 percent of the peak value, 122 mJy $beam^{-1}$. *Panel (c)*: Velocity map. *Panel (d)*: line width map resulting from the hyperfine fit. Numbers in panel (c) indicate the position of the fitted spectra shown in Fig. 2.2 and Table 2.2. The HPBW of 27.8″ is shown at bottom left corner of panel (c).

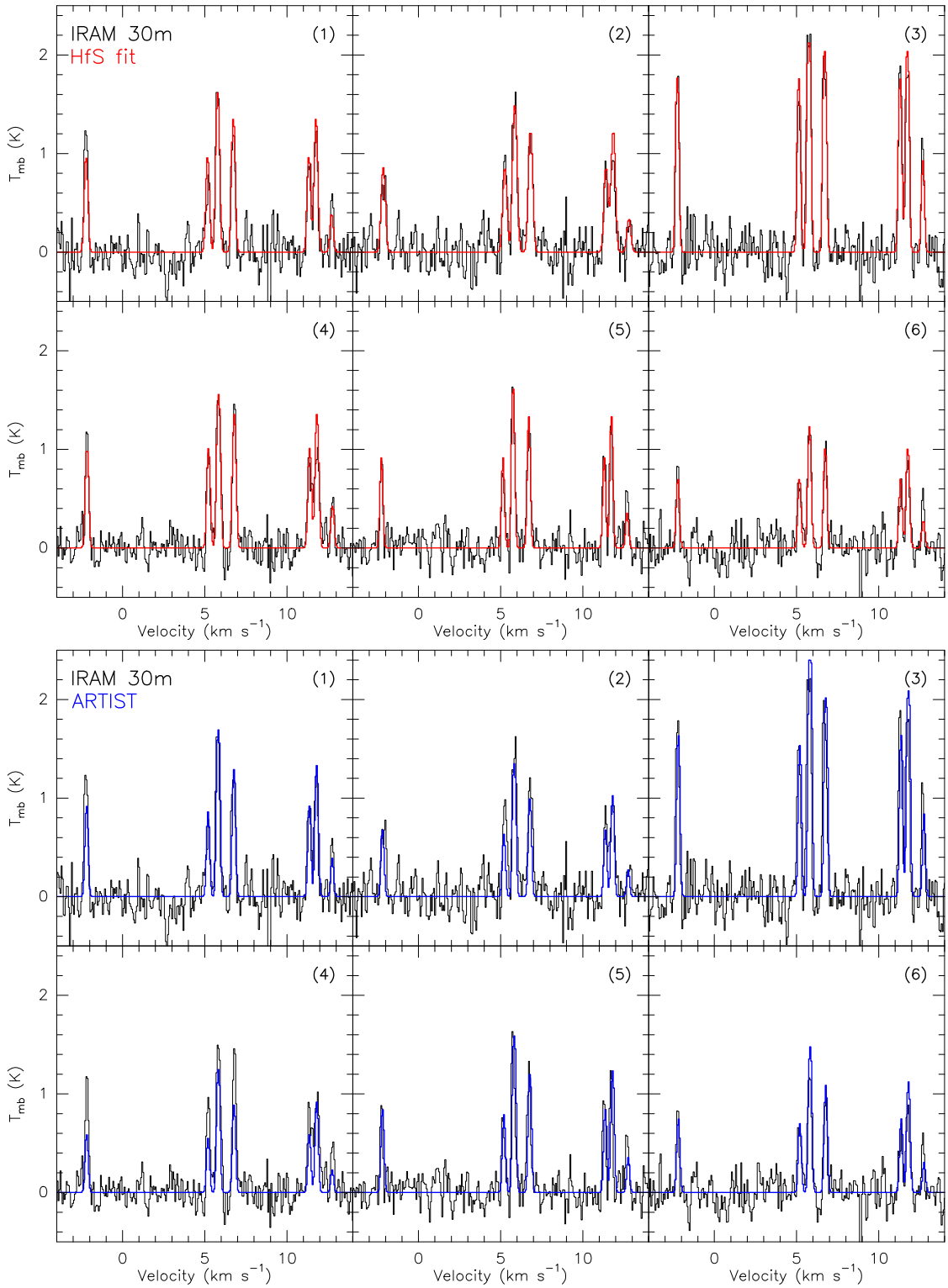

Fig. 2.2 *Upper pannels:* HfS fit of the hyperfine structure of N_2H^+ (1−0) IRAM 30m spectral data at different positions of the core (labeled in Fig. 2.1c). Black and red lines are the observational data and the fit, respectively. *Lower panels*: ARTIST simulated N_2H^+ (1−0) spectral data (see Sec. 2.4.2). Black and blue lines are the observational and simulated data, respectively. Note that the simulated core from ARTIST is spherically symmetric. The discrepancies between the observational and the simulated spectra in panel (4) may be due to the slightly elongated shape of the core towards the west.

Table 2.2 HfS fit parameters at different positions of FeSt 1-457.

$A\times\tau_m$ [a] (K)	v_{LSR} [b] (km s^{-1})	Δv [c] (km s^{-1})	τ_m [d]	rms (K)	Position (see Fig. 2.1c)
3.1±0.6	5.785±0.012	0.231±0.019	1.4±0.4	0.176	1
2.5±0.5	5.863±0.014	0.277±0.022	1.1±0.4	0.166	2
8.7±1.1	5.752±0.007	0.200±0.009	4.0±0.5	0.166	3
3.5±0.4	5.839±0.008	0.220±0.013	1.9±0.3	0.124	4
2.7±0.4	5.755±0.008	0.199±0.014	1.1±0.3	0.130	5
2.2±0.5	5.788±0.014	0.210±0.022	1.2±0.5	0.156	6

[a] $A\times\tau_m$, product of the amplitude ($A= f[J_\nu(T_{ex})-J_\nu(T_{bg})]$, where f is the filling factor, $J_\nu(T)$ is the Planck function in units of temperature, T_{ex} is the excitation temperature and T_{bg} is the cosmic microwave background temperature) times the optical depth of the main component.

[b] v_{LSR}, central velocity of the main component.

[c] Δv, linewidth of the hyperfine components.

[d] τ_m, optical depth of the main component. (See Estalella, 2016, for further details of the HfS fitting procedure.)

there are some slight discrepancies in the amplitudes of the two hyperfine lines out of LTE (the two with the highest velocity), the synthetic spectra (assuming LTE) fit very well the observed spectra.

In Fig. 2.1b we show the resulting N_2H^+ column density map overlapped with the 1.2 mm dust continuum emission. The values range from 3×10^{12} cm^{-2} at the edges to 9.0×10^{12} cm^{-2} towards the center, with hints of an arc-like structure near the continuum peak marginally resolved (see Sec. 2.3.1 below).

The velocity map shown in Fig. 2.1c presents a very smooth gradient in the northeast-southwest direction. The velocity ranges from 5.72±0.01 km s^{-1} at the northeast to 5.90 ± 0.01 km s^{-1} at the southwest. Excluding the southwesternmost region, the velocity gradient along the northeast-southwest direction is ≃1.8 km s^{-1} pc^{-1}. Aguti et al. (2007) find a similar velocity pattern in the $C^{18}O$ (1−0) and (2−1) channel maps.

The typical line widths (see Fig. 2.1d) are 0.17–0.23 (±0.03 km s^{-1}), except in the southwesternmost region, where it raises up to 0.30±0.03 km s^{-1} (also in agreement with the results from Aguti et al., 2007). Note that the eastern side of the core shows the lowest line widths. The thermal line width for N_2H^+ has a value of 0.12 km s^{-1}, for a kinetic temperature of 10 K. Thus, the three-dimensional non thermal dispersion ($\sigma_{3D,nth}$) ranges between 0.09 and 0.21 km s^{-1}. The isothermal sound speed value c_s is 0.19 km s^{-1}, which

gives a Mach number (defined as $\sigma_{3D,nth}/c_s$) between 0.46 to 1.1 (following Palau et al., 2015). These values indicate that the non thermal motions seem to be subsonic (as reported by Alves et al., 2014; Frau et al., 2010, 2012b) and the thermal pressure seems to be dominant over the turbulent pressure in the core (in agreement with Aguti et al., 2007) except at the southwestern corner where the ratio seems to be more balanced.

PdBI data

In Fig. 2.3 we show a section of the channel map showing the N_2H^+ (1−0) emission detected with the PdB interferometer. The weak emission (6σ) is better detected in the second panel corresponding to the strongest line of the three central hyperfine lines, at a velocity of 5.80 km s^{-1}. The last panel of Fig. 2.3 shows the spectra (in red) at the position of the 6σ detection. The IRAM 30m spectra (in black) is also shown as comparison, and we can see that the hyperfine structure is also seen in the PdBI spectrum indicating that indeed there is a real N_2H^+ detection from the PdBI. The emission filtered out by the PdBI with respect to the IRAM 30m is estimated to be $\sim 98\%$, from a comparison of the PdBI spectra (convolved with a Gaussian to obtain the IRAM 30m beam size) and the IRAM 30m spectra at the peak position. Given the smallest antenna baseline of PdBI observations, the largest angular scale detectable by the PdBI observations is $\sim 12''$ or $\sim 1,700$ au (following Appendix of Palau et al., 2010). Thus, about 98% of the emission detected with the IRAM 30m comes from structures at scales $\geq 1,700$ au.

IRAM 30m+PdBI

In Fig. 2.4 we show the moment-zero map of the merged IRAM 30m and PdBI data (see Sec. 2.2.3), overlapped with IRAM 30m MAMBO-II map of the dust continuum emission at 1.2 mm. The peak is 1 Jy beam^{-1} km s^{-1} and the arc structure hinted at the column-density single-dish map (panel (b) of Fig.2.1) is now clearly seen.

2.3.2 Chemical survey (FTS)

In this Section, we describe the maps of 15 molecular lines detected with the IRAM 30m FTS spectrometer towards FeSt 1-457 (see Fig. 2.5 and Table 2.1). To generate the maps we performed a gaussian smoothing of 3 pixels and we used the MAP_AVER task of GREG software to average the intensity of only the channels with detected emission to obtain a better signal-to-noise ratio and to better characterize the structure of the faintest lines. As presented in previous works (Frau et al., 2010, 2012b) we observed a rich chemistry with emission from early- (e.g., C_3H_2, HCN, CS) and late-time molecules (e.g., N_2H^+). For the

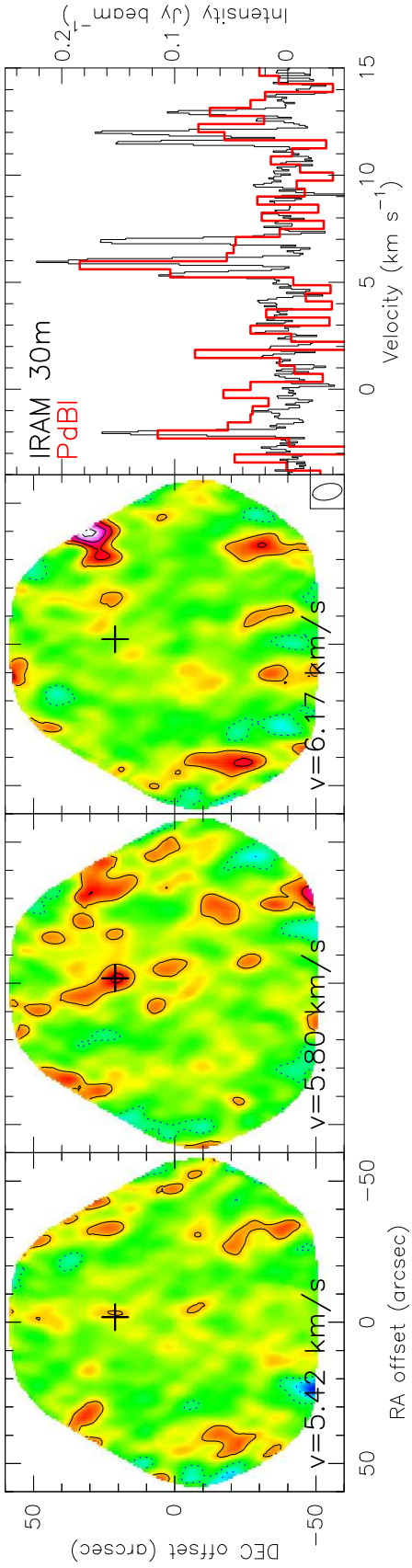

Fig. 2.3 PdBI channel map of N_2H^+ (1–0). Contours are −6, −3, 3, 6, 9, 12 times the rms level of the map, 25 mJy beam^{-1} ($\sim$ 53 mK). The synthesized beam located at the bottom right corner of the third panel is $10.6'' \times 5.74''$, with a P.A. of 11.94°. Note that the rms noise increases at the edge of the images. Last panel shows the PdBI spectrum (red line) at the position of the cross. The IRAM 30m N_2H^+ spectrum (black) has been divided by a factor of 5 to compare the hyperfine structure with the PdBI spectrum.

nitrogen-bearing molecules (e.g., HNC and N_2H^+; panels (a) to (f)) the gas emission is very compact and the peak coincides well with the peak of the 1.2 mm dust continuum emission. A similar behavior is seen in C_3H_2 (panels (g) and (h)). However, for C_4H and molecules containing oxygen in our sample (e.g., HCO^+, CH_3OH; panels (i) to (k)) the emission is shifted $\sim 44''$ towards the southwest with respect to the dust. An extreme case of this would be the $C^{18}O$ and ^{13}CO molecules, which present strong extended emission peaking to the southwest, at $\sim 120''$ and $\sim 60''$ of the dust continuum, respectively (panels (l) and (m)). For the molecules containing sulphur (CS and SO, panels (o) and (p)) the emission is located to the east with respect to the dust peak, $\sim 35''$ and $\sim 25''$, respectively. The peak offsets of the molecular lines with respect to the 1.2 mm dust continuum peak are comparable to the beam sizes of the gaussian smoothed integrated intensity maps ($\sim 45''$; see Table 2.3) and therefore significant. Panel (n) shows the emission of a second (and fainter) velocity component of the ^{13}CO emission at 3 km s^{-1}.

Regarding the intensity of the lines, apart from the ^{13}CO and $C^{18}O$ which do not trace the core well, the brightest lines are HNC, HCO^+ and N_2H^+. We found the weaker lines to be C_4H, NH_2D and $H^{13}CN$. This is in agreement with the previous observations by Aguti et al. (2007). However, they find the morphology of N_2H^+ more compact compared to our data. This difference could be due to the better S/N of our observations which allowed us to detect weaker extended emission. As the FTS backend has poor spectral resolution, the specific values of the line intensities cannot be compared with other works due to the spectral dilution. This does not affect the relative positions as the lines are narrow throughout the core. Note that the VESPA and FTS N_2H^+ maps present very similar structure (see Figs. 2.1a and 2.5e).

2.4 Analysis

2.4.1 The Bonnor-Ebert sphere model fit

The physical structure of starless cores can be well explained through a Bonnor-Ebert profile (Bonnor, 1956; Ebert, 1955), i.e., the profile corresponding to an isothermal gas sphere in hydrostatic equilibrium. The density profile can be derived solving the Lane-Emden equation

$$\frac{1}{\xi^2}\frac{d}{d\xi}\left(\xi^2\frac{d\phi}{d\xi}\right) = e^{-\phi}, \tag{2.1}$$

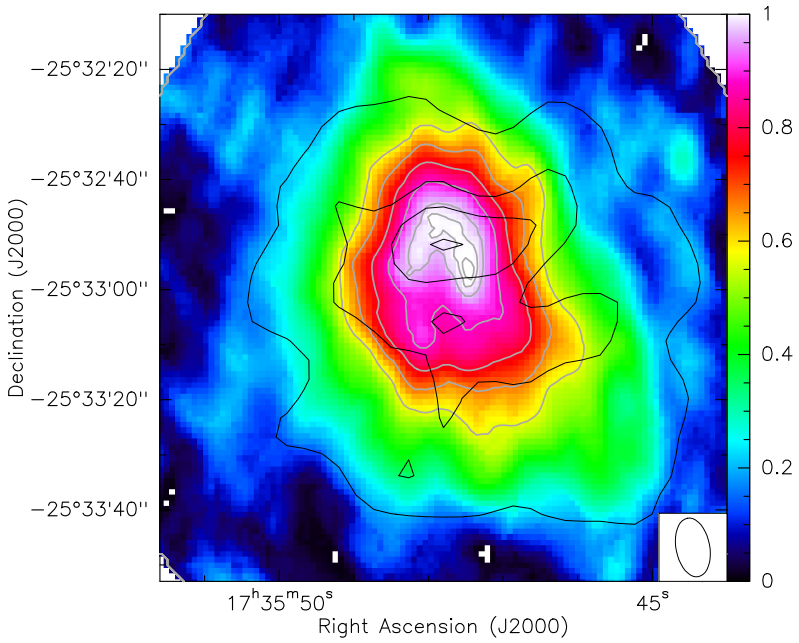

Fig. 2.4 *Color scale*: Moment-zero map of the IRAM 30m and PdBI combined data. Contours are 57, 67, 77, 88, 97, 99.5, 100 percent of the peak, 1 Jy beam^{-1} km s^{-1}. The synthesized beam located at bottom right is $10.8'' \times 6.11''$, with a P.A. of 10.79°. *Black contours*: MAMBO-II 1.2 mm dust continuum emission at an angular resolution of $15''$. Contours are 59, 79, 89, 99 percent of the peak, 57 mJy beam^{-1}.

where ξ is the non-dimensional radius,

$$\xi = r\frac{\sqrt{4\pi G\rho}}{c_s}, \tag{2.2}$$

where r, ρ, G and c_s are the radius, the volume density, the gravitational constant, and the sound speed, respectively. ϕ is the logarithm of the density contrast and is given by

$$\phi = \ln\left(\frac{\rho_c}{\rho}\right), \tag{2.3}$$

where ρ_c is the central volume density. The sound speed, c_s, is defined as $c_s = \sqrt{kT/\mu}$, where k, T, and μ are the Boltzmann constant, the temperature, and the mean molecular mass, assumed to be 2.33. Imposing the density at the core center to be ρ_c and its derivative to be 0 (i.e., $\rho = \rho_c$ and $d\rho/dr = 0$ at $r = 0$), Eq. (2.1) can be solved numerically. An important parameter characterizes the Bonnor-Ebert solution. This is the $\xi_{\max}$ parameter given by $\xi_{\max} = (R_{\rm out}/c_s)\sqrt{4\pi G\rho}$, where $R_{\rm out}$ is the outer radius where the outer confining pressure, $P_{\rm out}$, is exerted. $\xi_{\max} = 6.5$, which corresponds to $(\rho_c/\rho)_{\max} = 14.1$, is the critical value. For values larger than $\xi_{\max}$ the equilibrium is unstable to gravitational collapse.

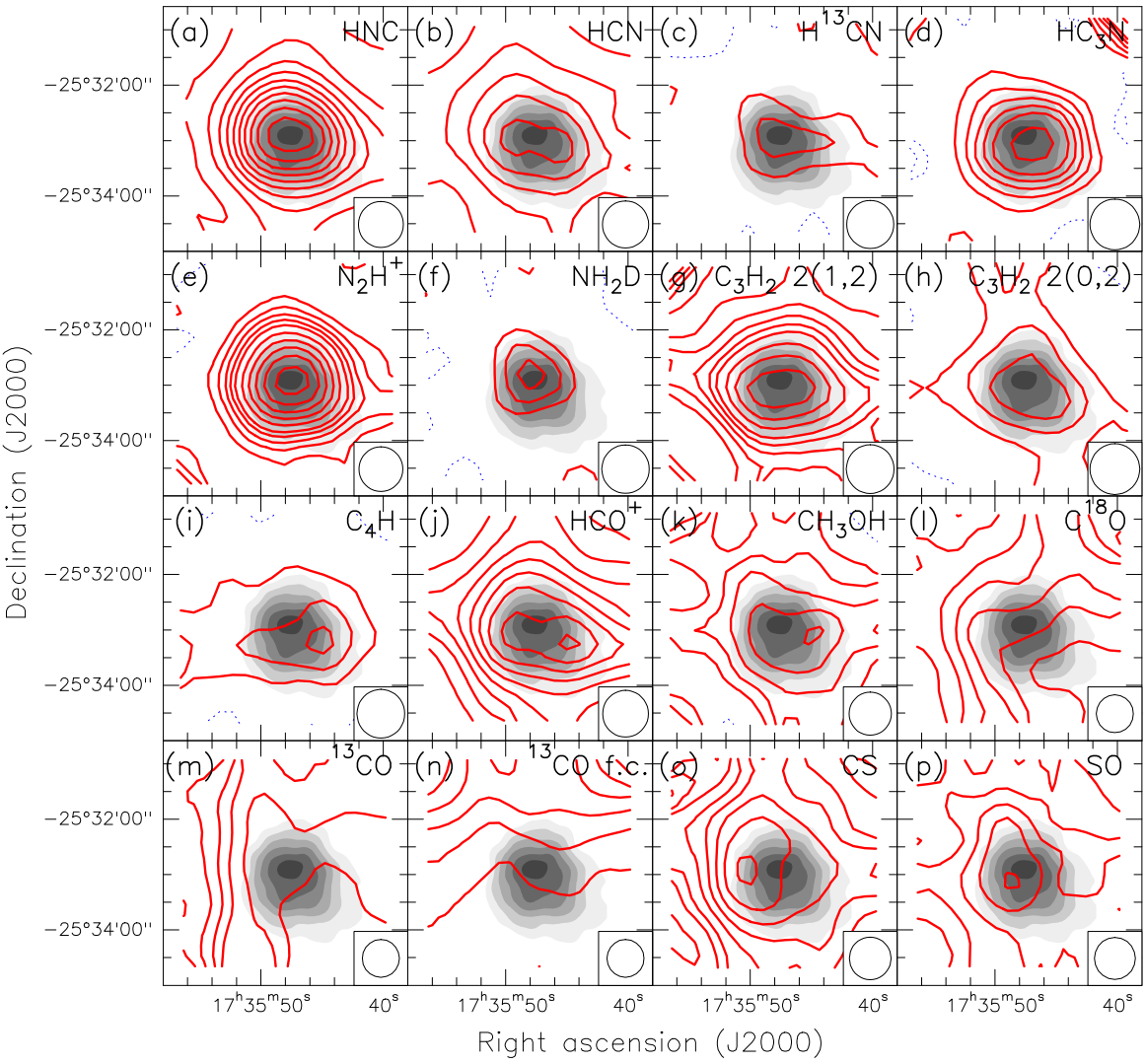

Fig. 2.5 *Red contours*: averaged intensity maps of the observed molecular transition indicated in each panel. Contours in (a), (j) and (l) are 10, 20, 30, ... times the rms of the maps, 8, 6 and 9 mK, respectively. In panels (m) and (n) contours are 20, 23, 26, ... and −3, 3, 6, 9, ... times the rms, 53 mK, respectively. In panels (b) and (h), (k) and (p) countours are −3, 3, 6, 9, 12, 15, 20, ... times the rms, 21 mK and 16 mK, respectively. In the rest of the maps contours are −3, 3, 6, 9, 12, 15, 20, 25, 30, 35, ... times the rms, 10 mK. Panel (n) shows a fainter component of the ^{13}CO molecular line. The beam size of each molecular line is shown at the bottom right corner of each panel. *Gray scale*: IRAM 30m MAMBO-II map of the dust continuum emission at 1.2 mm at an angular resolution of 21″.

To fit the observational data of FeSt 1-457, Frau (2012, PhD thesis) generated synthetic 3D cores with density profiles fulfilling the numerical integration of a Bonnor-Ebert sphere (Eqs. (2.1), (2.2), and (2.3)) with a given set of parameters. Then, the emission was integrated along the line of sight to generate 2D synthetic maps following a similar recipe as in

Table 2.3 Chemical differentiation.

Molecule	θ^{a} ($''$)	S/N	Peak shift[b] ($''$)	σ_s^{c} ($''$)
HNC	49.8	106	7	0.2
HCN	51.0	16	21, 26	1.4
$H^{13}CN$	52.1	8	10	3.1
HC_3N	55.0	20	14	1.3
N_2H^+	48.4	52	10	0.4
NH_2D	52.5	10	7	2.3
C_3H_2 2(1,2)	52.8	33	13	0.7
C_3H_2 2(0,2)	55.0	12	33	2.1
C_4H	52.8	9	43	2.6
HCO^+	50.6	103	43	0.2
CH_3OH	46.6	14	45	1.5
$C^{18}O$	41.0	81	119	0.2
^{13}CO	41.0	41	58	0.4
CS	46.2	41	33	0.5
SO	45.4	15	24	1.4

[a] Beam size after a Gaussian smoothing of 3 pixels (pixel size $\sim 13''$).

[b] Peak shift with respect to the 1.2 mm dust continuum peak.

[c] Position uncertainty given by $\sigma_s = (\frac{4}{\pi})^{1/4} \times \frac{\theta}{\sqrt{8\ln 2}}/(S/N)$ (Reid et al., 1988).

Frau et al. (2011). The presence of the molecular cloud surrounding the core was taken into account by adding a term in the extinction data, A_v^{bg}, which is constant along the extinction map. Since the IRAM 30m bolometer filters out the extended emission, it was assumed that the molecular cloud does not contribute to the 1.2 mm continuum emission. Two maps were generated, a visual extinction map and a 1.2 mm dust continuum emission map, convolved to the respective observational beams ($20''$ and $21.5''$ from Frau et al., 2010, 2012b; Román-Zúñiga et al., 2010, respectively). A dust opacity of $\kappa_{250GHz} = 0.007$ cm^2 g^{-1} was adopted for dust grains with thin ice mantles and for gas density $< 10^6$ cm^{-3} (Ossenkopf and Henning, 1994). Finally, radial profiles of the observed and synthetic maps were obtained using the ELLINT task from the MIRIAD software (Sault et al., 1995). This task averages the intensity in concentric annuli. The quality of the fit was assessed by computing the χ^2 residual fit of the two radial profiles. Figure 2.6 shows the comparison between the observational

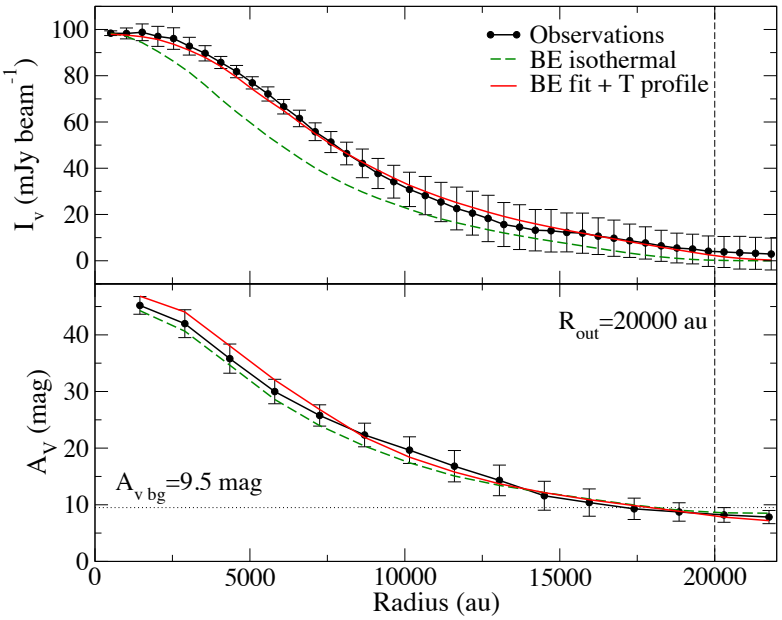

Fig. 2.6 *Upper panel:* Intensity profile from the 1.2 mm dust continuum emission map (Frau et al., 2010, 2012b). Black line and dots: observed values with vertical bars depicting the ± 1-σ range. Green (long-dashed) line: isothermal Bonnor-Ebert fit (Frau 2012, PhD thesis). Red (solid) line: fitted Bonnor-Ebert profile adding the temperature profile shown in the upper panel of Fig. 2.7. The best fitting central density is $\rho_c = 2 \times 10^5$ cm^{-3}. The fitted core boundary radius, $R_{\rm out} = 20,000$ au is marked by a vertical dashed line. *Lower panel:* $A_{\rm V}$ profile from the dust extinction map (Román-Zúñiga et al., 2010, 2009). Black, green (long-dashed) and red (solid) lines as in upper panel. The fitted core boundary radius, $R_{\rm out} = 20,000$ au, and $A_{\rm V}$ value of the surrounding medium, $A_{\rm V}^{\rm bg} = 9.5$ mag, are labeled and marked by a vertical dashed line and horizontal dotted line, respectively.

(black lines and dots) and synthetic Bonnor-Ebert (green long-dashed lines) emission radial profiles.

The best fit was obtained for the values shown in Table 2.4 (Frau 2012, PhD thesis). The first row lists the fitted parameters of the Bonnor-Ebert profile (ρ_c, $R_{\rm out}$, and T), the physical parameters derived ($\xi_{\rm max}$, ρ_c/ρ_R, $P_{\rm out}$, and mass), the fitted background visual extinction coming from the surrounding ambient medium ($A_{\rm V}^{\rm bg}$), the gravitational stability status, and an age estimate (Aikawa et al., 2005). There is no degeneracy between the fitted parameters ρ_c, $R_{\rm out}$, and T as the visual extinction map does not depend on temperature and ρ_c and $R_{\rm out}$ modify the height and width of the radial profile, respectively. The temperature only modifies the 1.2 mm dust continuum emission map. The temperature derived from the Bonnor-Ebert fit (10.5 ± 0.1 K) was found in fair agreement with the temperature derived from ammonia observations (9.5 ± 0.1 K; Rathborne et al., 2008). The value obtained for the

Table 2.4 Bonnor-Ebert fit parameters of FeSt 1-457.

Model	ρ_c (10^3 cm^{-3})	$R_{\rm out}$ (10^3 au)	T[b] (K)	$\xi_{\rm max}$	ρ_c/ρ_R	$P_{\rm out}$ (10^5 K cm^{-3})	Mass ($M_\odot$)	$A_V^{\rm bg}$ (mag)	Stable?	Age[c] (yr)
BE isothermal[a]	200 ± 20	20 ± 1	10.5 ± 0.1	10.5 ± 0.7	47 ± 5	0.6 ± 0.1	2.7	9.5	No	9.6×10^5
BE + $T_{\rm profile}$[d]	200 ± 20	20 ± 1	12.0 ± 0.1	9.8 ± 0.7	40 ± 5	0.8 ± 0.1	2.7	9.5	No	9.6×10^5

[a] Parameters fitted for the isothermal BE model (Frau 2012, PhD thesis). The uncertainties of the fitted parameters ρ_c, $R_{\rm out}$ and T were estimated by analyzing the increase of the χ^2 residual fit by varying the parameters. The uncertainties of the derived physical parameters $\xi_{\rm max}$, ρ_c/ρ_R and $P_{\rm out}$ were assessed through error propagation analysis.

[b] Temperature used to determine the sound speed value, c_s.

[c] Based on Aikawa et al. (2005) results following the evolution of a marginally unstable Bonnor-Ebert sphere ($T = 10$ K, $\alpha = 1.1$, where α is the internal gravity to pressure ratio).

[d] Modified Bonnor-Ebert model using the temperature profile of the upper panel of Fig. 2.7. The uncertainties are the same as in the isothermal model because the new temperature profile does not modify the Bonnor-Ebert density profile, it only modifies the resulting 1.2 mm emission (see Sec. 2.4.1).

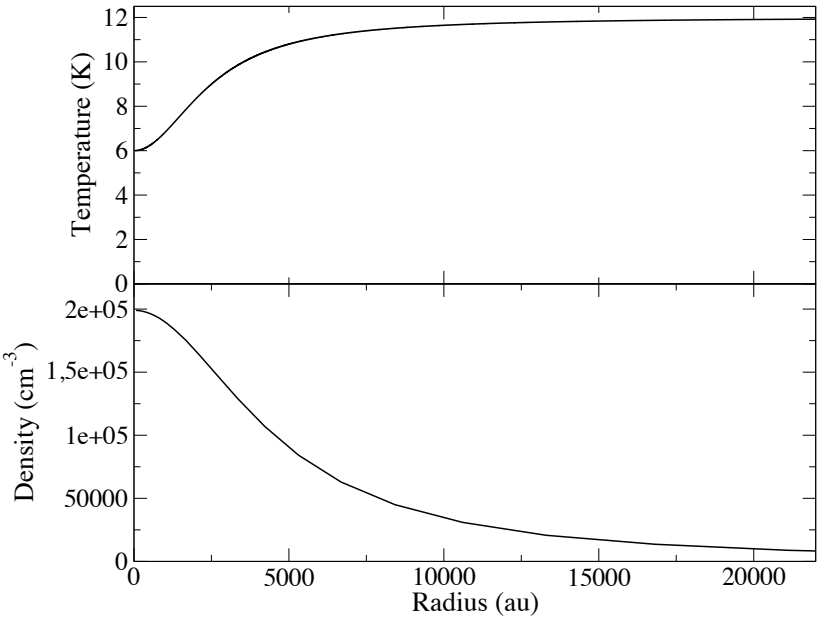

Fig. 2.7 Temperature profile (*upper panel*) and Bonnor-Ebert density profile (*lower panel*) used in this work (see Sec. 2.4.1).

derived parameter $\xi_{\max}$ was 10.5 ± 0.7. The error was estimated through error propagation analysis, being ρ_c and $R_{\rm out}$ the main contributors to its uncertainty (see Table 2.4). This value is significantly higher than the critical value (6.5), thus the core is gravitationally unstable, in accordance with Kandori et al. (2005) results.

FeSt 1-457 is observed with an excellent signal-to-noise to test the Bonnor-Ebert scenario. Using the isothermal Bonnor-Ebert sphere, Frau (2012, PhD thesis) found a good fit for the visual extinction map but non-negligible differences in the 1.2 mm dust continuum emission profile (see green long-dashed line in Fig. 2.6). This can be interpreted as a departure from the isothermal approximation because the extinction map ($A_{\rm V}$), contrary to the dust continuum emission, is only sensitive to the column density and does not depend on temperature. Earlier studies (e.g., Crapsi et al., 2007) show that starless cores with $n_{H_2} > 10^5$ cm^{-3} may have an inner temperature gradient. These cores can reach temperatures as low as 6 K at their centers, while at the outer shells are warmer as they may be heated by the interstellar radiation field (e.g., Marsh et al., 2014). In this work we tested different temperature profiles to check whether the fits improved. We found that a temperature profile following:

$$T(r) = T_{\rm out} - \frac{(T_{\rm out} - T_{\rm in})}{(1 + (r/r_{\rm in})^2)} \tag{2.4}$$

($r_{\rm in} = 2,500$ au), with $T_{\rm in} = 6$ K at the center of the core and increasing until $T_{\rm out} = 12$ K at a radius of 9,000 au, fitted much better the data. The second row of Table 2.4 shows the best fit parameters of the Bonnor-Ebert+temperature gradient model. Figure 2.7 shows the Bonnor-Ebert density and temperature profiles that appear to fit best the data. In addition, the red line in Fig. 2.6 shows the predicted 1.2 mm dust intensity and extinction radial profiles from this Bonnor-Ebert+temperature gradient model. Forbrich et al. (2015) also find a clear decrease of the effective dust temperature towards the center of FeSt 1-457 from *Herschel* observations. However, they find the lowest value at the center to be 13.5 K, higher than kinetic gas temperature derived from ammonia (9.5 K; Rathborne et al., 2008) and higher than the temperature at the center of the core adopted by us. They argue this difference could be related to the effect of averaging the emission from *Herschel* along the line of sight which would take into account dust from the cloud at higher temperatures. Note that the temperature profile we found fits well the FeSt 1-457 core is similar to the one found for the L1544 core (Crapsi et al., 2007), a core with significantly higher density, but also to core 16 from Marsh et al. (2014), which has a density similar to that of FeSt1-457.

Even though we did not modify the Bonnor-Ebert density profile (lower panel of Fig. 2.7), which assumes a constant temperature, we finally considered the temperature profile shown in the upper panel of Fig. 2.7 to generate the synthetic maps. This apparent inconsistency is not important in our case. Sipilä et al. (2011) show that the isothermal and non-isothermal Bonnor-Ebert density profiles are fairly similar. In addition, as the gas pressure is proportional to the temperature, reducing the temperature by half, reduces the pressure by half as well, which makes the core even more unstable against gravity. Therefore, this model is good enough to say that FeSt 1-457 has a density profile of a very young core, it is gravitationally unstable and seems to be colder at the center than in the outer parts.

2.4.2 ARTIST

Once the physical model of temperature and density of the core was determined (see previous Section), we estimated the abundances for the molecular lines detected with the IRAM 30m observations.

We used the Adaptable Radiative Transfer Innovations for Submillimeter Telescopes (ARTIST; Brinch and Hogerheijde, 2010; Jørgensen et al., 2014; Padovani et al., 2012, 2011) software to generate a synthetic spectral cube of the molecular lines detected. We assume that the source is spherically symmetric with the density and temperature radial profiles derived from the Bonnor-Ebert model derived in the previous Section.

For the simulations we assumed the dust temperature equal to the gas temperature. We assumed no velocity field in the core. The velocity gradient in the core is very small ($\lesssim$

0.05 km s^{-1} $beam^{-1}$ at the center of the core), so this does not affect the results. Initially, the only free parameter used in ARTIST was the abundance. First, we assumed a constant value for the abundance. If the model did not fit well the observed intensity profile, we used a step function with two or three different abundances to obtain more accurate fits. We systematically tried different values for the radius at which there was a change in abundance, until obtaining the smallest χ^2 parameter. One or two step functions (at a radius of $55''$ ($\sim 8,000$ au) and $100''$ (14,500 au)) for the abundance was necessary to obtain good fits for 10 out of the 12 molecules, in which a constant abundance value did not fit well the observed data. We made use of the Leiden Atomic and Molecular Database (LAMDA)[5] to load the collisional coefficients of the observed molecules (Chandra and Kegel, 2000; Daniel et al., 2005; Flower, 1999; Green and Chapman, 1978; Green and Thaddeus, 1974; Lique et al., 2006a,b; Rabli and Flower, 2010; Yang et al., 2010). The spectral cube generated with ARTIST was convolved with a Gaussian to mimic the angular resolution of each molecular line observed. The output from ARTIST is given in units of brightness temperature.

In order to compare both the observed and the synthetic molecular line maps, we generated line intensity profiles for both data sets in the same way using the MIRIAD software. We first computed integrated intensity maps (moment-zero) using the MOMENT task over a velocity range that included all the emission. Then, we used the ELLINT task for the integrated intensity maps to compute the line radial profiles with annuli of $10''$ width, which is a value between one third and one fifth of the angular resolution of the observed molecular lines.

Figures 2.8 and 2.9 show the annuli averaged integrated intensity (moment-zero) vs. the annuli radius for the observed (open circles) and ARTIST produced data.

N_2H^+ abundance fit

To obtain the moment-zero map of N_2H^+ (see Fig. 2.1a), we only included the three central hyperfine lines to avoid the anomalous hyperfine lines (see Sec. 2.3.1) and we obtained a good fit of the data. The high spectral resolution ARTIST fit is shown in the lower panel of Fig. 2.2 (note that ARTIST handles line overlapping: Brinch and Hogerheijde, 2010). We first used a constant abundance (with respect to H_2) to fit the radial profile. A value of 2.5×10^{-10} fitted well the data except for the outer radius where the model gave slightly higher values (blue dashed line of Fig. 2.8). Thus, we used a step function varying the radius at which there was a change in abundance systematically in steps of $10''$, and a better fit was obtained with values of 2.5×10^{-10} and 1.5×10^{-10} for smaller and larger radius than $55''$ ($\sim 8,000$ au), respectively (red line of Fig. 2.8). The error of the radius where the abundance

[5] http://home.strw.leidenuniv.nl/∼moldata/

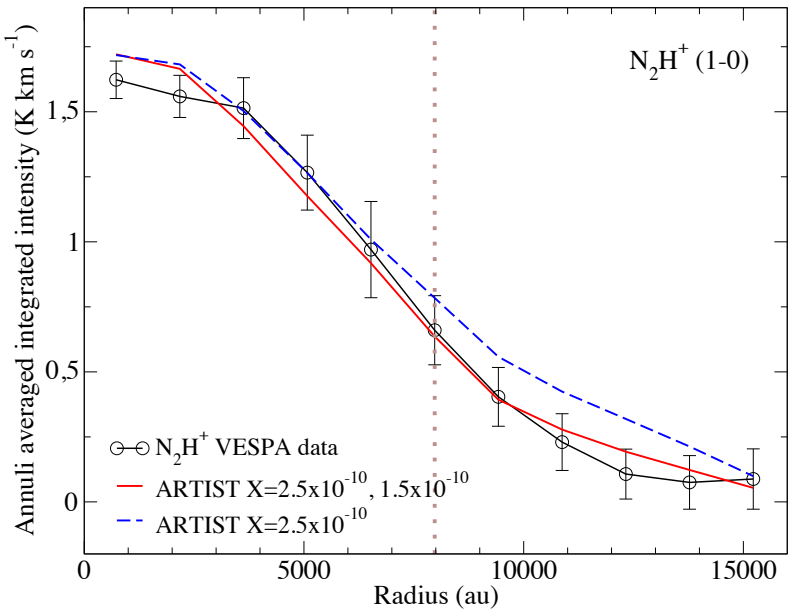

Fig. 2.8 N_2H^+ ARTIST abundance estimate. Annuli averaged integrated intensity vs. annuli radius. *Black line*: IRAM 30m VESPA data. *Blue dashed line*: ARTIST radial integrated intensity profile for a constant abundance of 2.5×10^{-10}. *Red line*: ARTIST radial integrated intensity profile with a step function abundance of 2.5×10^{-10} and 1.5×10^{-10} for smaller and larger radius than $\sim 8,000$ au ($55''$; indicated by the brown vertical dotted line), respectively.

changes is $\pm 15''$, estimated from a χ^2 analysis (e.g., Gibb et al., 2000). We also estimated the abundance uncertainty for the N_2H^+ line to be less than $\sim 15\%$. This uncertainty was estimated from a χ^2 analysis using different values of the abundance at the same range of radii of the core.

FTS molecular lines abundance fits

We followed the same procedure used for N_2H^+ to fit the other molecular lines detected with the FTS spectrometer, except for C_4H for which the collisional coefficients file was not available in the LAMDA catalogue. $H^{13}CN$ and C_3H_2 2(0,2)−1(1,1) were not fitted as they present weak emission and we had better signal to noise in the similar molecules/transitions HCN and C_3H_2 2(1,2)−1(0,1). The observed intensity profiles are presented in Fig. 2.9 (open circles). Our ARTIST modeling indicated that some molecular lines are well fitted with just one abundance value. This is the case of HC_3N and C_3H_2 2(1,2) (see panels (c) and (e) of Fig. 2.9). HNC and NH_2D are well fitted with a one step function, one value at the

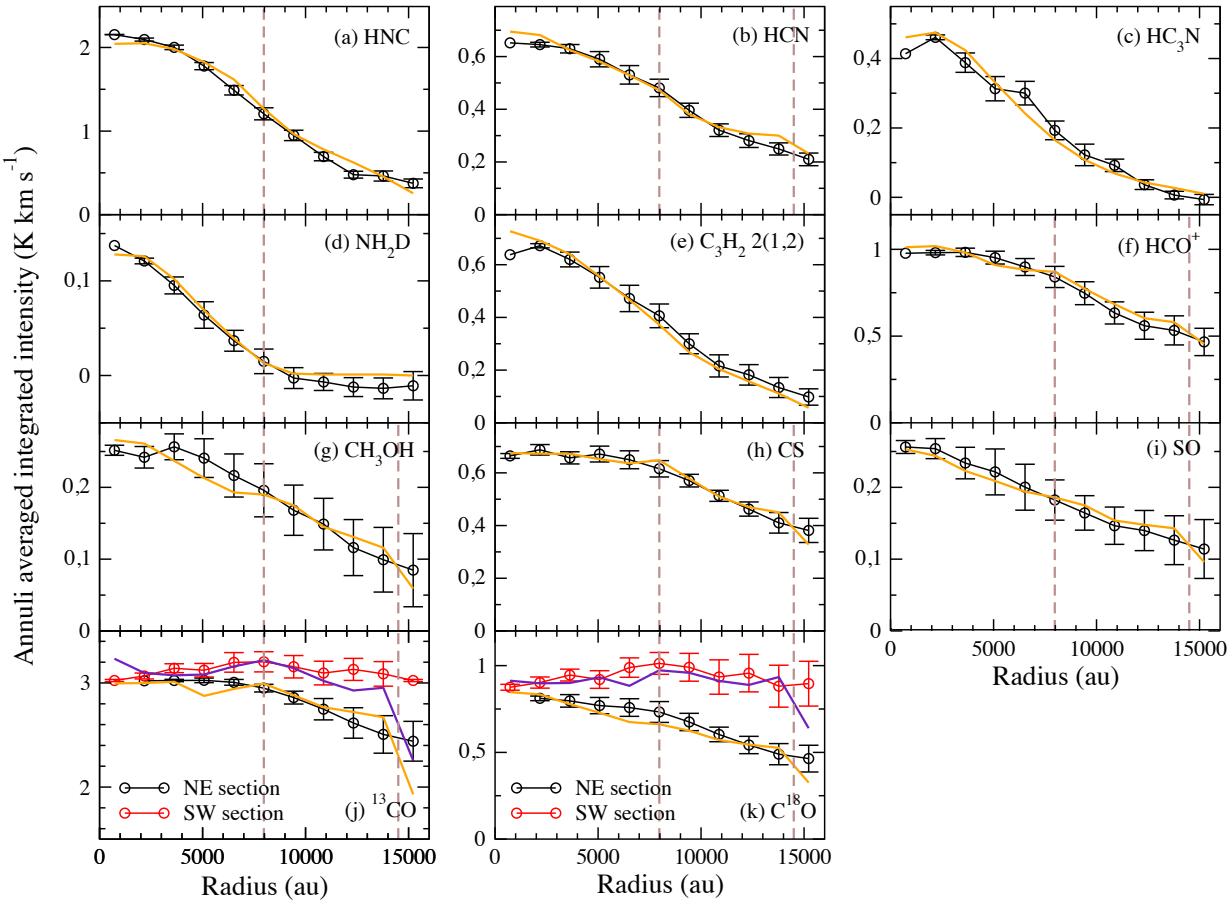

Fig. 2.9 FTS molecular lines abundance fits. Annuli averaged integrated intensity vs. annuli radius. *Black and red lines*: FTS data profiles. *Orange and violet lines*: ARTIST data profiles with estimated abundances. Brown vertical dashed lines indicate the radius where there is a change in abundance (see Table 2.5).

Table 2.5 Estimated molecular abundances using ARTIST.

Molecule	$0'' - 55''$ $0 - 8,000$ (au)[a]	$55'' - 100''$ $8,000 - 14,500$ (au)[a]	$> 100''$ $> 14,500$ (au)[a]
N_2H^+	2.5×10^{-10}	1.5×10^{-10}	1.5×10^{-10}
HNC	1.5×10^{-9}	6.0×10^{-10}	6.0×10^{-10}
HCN	3.0×10^{-10}	4.0×10^{-10}	2.0×10^{-9}
HC_3N	4.5×10^{-10}	4.5×10^{-10}	4.5×10^{-10}
NH_2D	3.0×10^{-10}	$< 10^{-11}$	$< 10^{-11}$
C_3H_2	4.0×10^{-10}	4.0×10^{-10}	4.0×10^{-10}
HCO^+	5.0×10^{-11}	1.5×10^{-10}	7.0×10^{-10}
CS	1.5×10^{-10}	8.0×10^{-10}	4.0×10^{-9}
SO	6.0×10^{-11}	2.0×10^{-10}	2.0×10^{-9}
CH_3OH	1.2×10^{-10}	2.5×10^{-10}	1.0×10^{-9}
$C^{18}O$ NE	1.5×10^{-8}	4.0×10^{-8}	2.0×10^{-7}
$C^{18}O$ SW	4.0×10^{-9}	6.0×10^{-8}	4.0×10^{-7}
^{13}CO NE	8.0×10^{-8}	3.5×10^{-7}	2.0×10^{-6}
^{13}CO SW	4.0×10^{-8}	4.0×10^{-7}	3.0×10^{-6}

[a] Annuli radius.

inner part of the core until $55''$ ($\sim 8,000$ au) radius and a smaller value at larger radii (see panels (a) and (d) of Fig. 2.9). However, our ARTIST model revealed that most of the lines needed 3 different abundance values changing at $55''$ and $100''$ ($\sim 8,000$ and 14,500 au) radius to obtain a good fit (radii where we assumed a change in abundance are marked in Fig. 2.9 by vertical dashed lines).

We estimated the abundance uncertainty for the CH_3OH (one of the molecules with the lowest signal-to-noise ratio) and HCN (one of the molecules with the highest signal-to-noise ratio) following the same procedure as with the N_2H^+ giving similar results.

In all cases where we introduced a 2 step function profile in the abundance, values are higher in the outer part of the core and decrease towards the center. We consider a slightly different analysis for the abundances of $C^{18}O$ and ^{13}CO lines. As their emission is very asymmetric presenting their peak at the southwest part with respect to the dust continuum (see panels (l) and (m) in Fig. 2.5), we divided the image in two sections, one including the strongest emission (southwest) and the other including the faintest emission to the north-eastern part, which resembles more the emission pattern of the other species. Thus this part should trace more reliably the behavior of this molecule in the core. We performed the same

procedure for the two sections separately. Both molecular lines show very flat profiles fitted with a 2 step function for the abundance as the emission is very extended (see panels (j) and (k) of Fig. 2.9). Table 2.5 summarizes the abundances for each molecule. Note that by using the main beam brightness temperature scale the intensity of the lines with extended emission, namely $C^{18}O$ and especially ^{13}CO, may be overestimated. This may result in some overestimation of their abundances but not of the observed relative drop within the core.

2.4.3 Estimation of the magnetic field strength

We made use of the polarization data presented in Alves et al. (2014) to estimate the magnetic field strength on the plane of the sky. The observations were performed at the APEX 12m telescope at 345 GHz obtaining a FWHM of $\sim 20''$. The magnetic field lines are relatively uniform with a weighted mean position angle of 130° (from north to east direction).

Using the Chandrasekhar-Fermi technique we are able to estimate the magnetic field strength. We used the Ostriker et al. (2001) approximation for estimates of the plane-of-sky field strength under strong-field cases ($\delta\phi \leq 25°$). The projected field strength ($B_{\rm pos}$) is given by:

$$B_{\rm pos} = 8.5 \frac{\sqrt{n_{\rm H_2}/(10^6\ {\rm cm^{-3}})}\Delta v/({\rm km\ s^{-1}})^{-1}}{\delta\phi\ {\rm deg}^{-1}}\ {\rm mG}, \tag{2.5}$$

where the number density of molecular hydrogen $n_{\rm H_2}$ is taken as $2.33 m_{\rm H} n_{\rm H}$, Δv is the observed line width and $\delta\phi$ is the dispersion of the polarization angles.

The observed dispersion $\delta\phi_{\rm obs}$, is produced by contributions from the measurement uncertainty of the polarization angle $\sigma_{\rm PA}$ and the intrinsic dispersion $\delta\phi_{\rm int}$. Taking into account every pair of polarization angles (PA) and their uncertainties $\sigma_{\rm PA}$ according to the equation

$$\delta\phi^2_{\rm int} = \frac{\sum\limits_{i,j} \left({\rm PA}_i - {\rm PA}_j\right)^2 - \left(\sigma^2_{{\rm PA}_i} + \sigma^2_{{\rm PA}_j}\right)}{N}, \tag{2.6}$$

where N is the number of data pairs, we obtained $\delta\phi_{\rm int} = 9°.22$

Frau et al. (2010) obtain $n_{\rm H_2} = 4\times10^5\ {\rm cm^{-3}}$, however, we adopted $n_{\rm H_2} = 6\times10^4\ {\rm cm^{-3}}$, as Alves et al. (2014) find depolarization at higher densities. From our N_2H^+ (1–0) observations, $\Delta v \sim 0.2$ km s^{-1}. Thus, we obtained $B_{\rm pos} \sim 45.2\ \mu$G and assumed to be uncertain by a factor of two.

2.5 Discussion

2.5.1 Molecular depletion

After our analysis with ARTIST (see Sec. 2.4.2), we found that molecular abundances are well fitted with three values, presenting a decrease of abundance towards the inner region of the core in most of the molecules detected (7 out of 12). The simplest explanation for the decrease of molecular abundance is that the molecules are depleted onto the dust grains once the density of the core increases and the temperature decreases. Some of these molecules are strongly depleted in the core interior with a decrease of abundances by at least 1 or 2 orders of magnitude. The strongest depletion is found in ^{13}CO and C^{18}O with a difference in abundance of 2 orders of magnitude, from $\sim 10^{-6}$ to $\sim 10^{-8}$ and $\sim 10^{-7}$ to $\sim 10^{-9}$, respectively. Aguti et al. (2007) find CO is depleted only by a factor of ~ 5 but by averaging the abundance along the line of sight. CS and SO also present strong depletion with a decrease of abundance of a factor of ~ 30 (it is known that sulphurated molecules tend to deplete quite fast in chemical models of dense cores, e.g., Ruffle et al., 1999). Similar results are found in Tafalla et al. (2004, 2002) in several starless cores. We also found a decrease in abundance of 1 order of magnitude in HCN and HCO$^+$. The HCN shows emission peaks at both sides of the continuum peak in an east-west strip. The decrease of emission around the continuum peak is probably an indication of heavily depletion at that position. Curiously, the shape of the HCN and HNC emissions are quite different close to the continuum peak. Loison et al. (2014) found that the HCN/HNC ratio tends to decrease when carbon atoms or CO are depleted, due to isomerisation of HCN into HNC. In fact, we see an increase of abundance of a factor of ~ 2 of HNC at the inner region of the core. Thus, the combination of depletion of HCN plus the conversion of HCN into HNC could be enough to explain the observed difference in emission.

Our best studied molecule, N_2H^+, is well fitted with two abundance values with a small increase towards the interior of the core (see Sec. 2.4.2). The abundance value $\sim 10^{-10}$ is in agreement with Aguti et al. (2007) results. In Sec. 2.3.1, we showed that the N_2H^+ column density follows an arc-structure around the 1.2 mm continuum peak (see Fig. 2.1b) which is clearly seen using the combined emission of IRAM 30m and PdBI (see Figure 2.4). This might not be seen in the ARTIST analysis because we averaged the emission in concentric annuli and the feature is only present at a very small scale of $5''$ or 725 au, suggesting that N_2H^+ might be frozen-out onto the dust grains at this scale, which corresponds to a density of $\sim 2 \times 10^5$ cm^{-3}. Aguti et al. (2007) also suggest posible depletion of N_2H^+ in FeSt 1-457 at depths > 40 mag of visual extinction, which corresponds to radii $\lesssim 3,350$ au and densities $\gtrsim 1.3 \times 10^5$ cm^{-3}. Our results are consistent with previous observations towards

starless cores, where N_2H^+ is depleted at densities $> 5 \times 10^5$ cm^{-3} (e.g., Belloche and André, 2004; Pagani et al., 2007). The arc-like structure is not likely due to opacity effects as in the calculation of the column density we already took opacity into account. Higher angular resolution and with even better sensitivity observations are needed to discard other explanations for the arc structure seen in N_2H^+ (such as a real physical structure).

NH_2D appears to have a significant abundance only in the inner region of the core, at radius $\lesssim 55''$ ($\lesssim 8,000$ au). Previous observational studies have shown evidence of NH_2D abundance increase towards starless cores (e.g., Busquet et al., 2010; Masqué et al., 2013). Deuterated ammonia is expected to be abundant in the coldest and densest parts of starless cores, where the depletion of CO enhances the deuterium fractionation through a combination of gas phase (e.g., Hatchell et al., 2013; Roberts et al., 2004) and surface reactions (e.g., Fedoseev et al., 2015; Fontani et al., 2015).

Finally, HC_3N and C_3H_2 are well fitted with a constant abundance value throughout the core. Tafalla et al. (2006) study the molecular abundances of two starless cores (L1498 and L1517B) and find depletion of 1 order of magnitude of HC_3N towards the center of L1498 and of only a factor of 2 in L1517B. However, they find that HC_3N seems to survive in the gas phase to higher densities than other species as CO and SO. They also find a similar behavior in L1498 for C_3H_2 and suggest that the chemistry of C_3H_2 and HC_3N could be related. In our case, we can only see some depletion effect in the molecular profiles of HC_3N and C_3H_2 in the innermost position closer to the center of the core ($\lesssim 20''$, see panels (c) and (e) of Fig. 2.9).

In summary, for most of the molecules detected in our sample (HCN, HCO^+, CH_3OH, CS, SO, ^{13}CO and C^{18}O), we found a clear decrease in their abundance towards the inner region of the core.

2.5.2 Chemical differentiation in the core's outskirts

As we have seen in Sec. 2.3.2, FeSt 1-457 presents a clear chemical differentiation for nitrogen, oxygen and sulphurated molecules. Their emission appears with different offsets with respect to the peak of the 1.2 mm dust continuum emission (see Sec. 2.3.2 and Table 2.3).

We computed the CS/C^{34}S, SO/^{34}SO and ^{13}CO/C^{18}O line intensity ratios from the integrated spectra of an area of $30''$ radius around the position where the main isotopologue line is brighter. Because these ratios are done for the same rotational transition, they depend only on the optical depth and abundance ratio of the isotopologues (we adopted an abundance ratio of 5.6 for ^{13}CO/C^{18}O and 24 for ^{32}S/^{34}S: Chin et al., 1995; Wilson and Matteucci, 1992). The optical depth for CS (2−1), SO 3(2)−2(1) and ^{13}CO (1−0) transitions is 1.54, 2.11 and 2.14, respectively. We expect this value to decrease as we go away from the peak. Thus, the

observed different morphologies are not likely due to opacity. In addition, the critical densities and energies of the upper level of N_2H^+ (1−0), CS (2−1) and HCO^+ (1−0) are similar, $\sim 10^5$ cm^{-3} and $4-7$ K, respectively (from LAMDA database; see Table 2.1). Therefore, we can exclude different excitation conditions as well. This suggests that different types of molecules are tracing different chemical conditions in the core.

The characteristic asymmetries in the emission of C_4H, HCO^+ and CH_3OH, peaking (south)west of the dust peak, could be evidence of the penetration of UV radiation into FeSt 1-457.

Moreover, $H^{13}CN$ and HC_3N also show a slight displacement of their emission peak towards the southwest. This may be a similar situation to the emission enhancement of these molecules in PDRs (photo-dominated regions) and in molecular condensations ahead of Herbig-Haro objects (e.g., Girart et al., 1998, 2002; Hollenbach and Tielens, 1997; Viti et al., 2006). In the second case, chemical models show that this enhancement is due to the UV radiation arising from the Herbig-Haro objects (Viti et al., 2003; Viti and Williams, 1999). Viti et al. (2003) find that the UV radiation affects the chemistry enhancing HCO^+ and CH_3OH for $A_V < 4$ mag, meaning that the enhanced emission should trace the most outer layer of the core. Additionally, PDR models show that C_4H reach higher abundances at somewhat less deep layers (lower A_V values) than HCN. Indeed, C_4H has been found to peak close to the edge of PDRs as its production is enhanced by the UV radiation field in a relatively narrow range of visual extinction values (e.g., Morata and Herbst, 2008; Pety et al., 2005; Rimmer et al., 2012). Moreover, in some PDR models (e.g., Morata and Herbst, 2008; Rimmer et al., 2012), HC_3N also has an abundance peak at similar layers to HCO^+.

FeSt 1-457 is, in projection, embedded in a diffuse molecular cloud with average $A_V^{bg} \sim 9.5$ mag. Thus, the enhanced C_4H, HCO^+ and CH_3OH emission could only happen if the core is near the border of the molecular cloud, such that one side of the core is exposed to the interstellar UV radiation without much absorption. We do not expect the penetration of the UV photons to be too large, but it is probably strong enough to produce some differences in the distribution of the molecular emission. Infrared extinction maps show that FeSt 1-457 is surrounded by gas with relatively low extinction, $A_V = 5-10$ mag (Román-Zúñiga et al., 2010). If the medium around FeSt 1-457 is not homogeneous, some UV radiation from a nearby OB star or the interstellar radiation field could be penetrating quite deep into the (western side of the) core. Indeed, Gritschneder and Lin (2012) proposed that the Pipe Nebula might be an H II region shell swept by the nearby θ Ophiuchi (a B2 IV β Cephei star). θ Ophiuchi lies in a direction approximately west-northwest of FeSt 1-457 and might be the source of the UV radiation required to explain the morphology of the emission of C_4H, HCO^+ and CH_3OH. Future works must be done to confirm this possible scenario.

Regarding the asymmetries of CS and SO emission (see panels (o) and (p) in Fig. 2.5, respectively), it has been studied that in PDRs (see Morata and Herbst, 2008) CS has a relatively shallow abundance closer to the edge of the PDR (around or inwards the C_4H peak) and a higher abundance in inner layers, while SO has high abundances in even deeper layers into the PDR. The combination of depletion and the influence of the UV field could explain the shape of the emission of these maps. If the eastern side of the core is more shielded from the radiation, these molecules will reach higher abundances and have their emission peaks there, while they will have lower abundances on the western side of the core (more markedly for SO), and they will be depleted towards the center of the core. Finally, N_2H^+ and deuterated molecules, from both the observational and chemical point of view, are supposed to be abundant in the inner and most shielded parts of the cloud (e.g., Crapsi et al., 2005; Roberts et al., 2003), which is what our emission maps show (see Fig. 2.5 and 2.9).

2.5.3 A correlation between depletion, grain growth and polarization

As we have seen in Sec. 2.4.2, and discussed in Sec. 2.5.1, molecular abundances are well fitted with two or three values, presenting a decrease of abundance towards the inner region of the core in most of the molecules detected. This change in the chemical properties suggests FeSt 1-457 experiences a variation in the physical properties of its inner region.

It is interesting to note that Forbrich et al. (2015) find evidence of grain growth at the inner region of the core from *Herschel*-derived dust opacity results and near-infrared extinction measurements. Depletion of the molecular gas onto the dust grains due to a decrease of temperature and increase of density in the center of the core could make easier for the grains to stick together and contribute to the grain growth seen by Forbrich et al. (2015). This is supported by the fact that we found a depletion radius very similar to the radius where Forbrich et al. find grain growth. It has been studied that water ice on the surface of dust particles enhance grain-grain adhesion favoring grain growth (e.g., Gundlach and Blum, 2015; Wang et al., 2005). Furthermore, Liu et al. (2013b) find that CO depletion positively correlates with a decrease of the dust emissivity index, which could be related to the size of the dust grains (e.g., Lommen et al., 2007; Piétu et al., 2014; Ricci et al., 2012). This also agrees with our results of low abundance of CO at the center of the core (see Fig. 2.5) and the grain growth seen by Forbrich et al. (2015).

In a different work, Alves et al. (2014) present a study of the polarization properties in FeSt 1-457 at different wavelengths and find that the emission is more polarized to the western side of the core (see Alves et al., 2014, Fig. 1). It is globally accepted that non-spherical dust grains are aligned perpendicularly with respect to magnetic field lines pro-

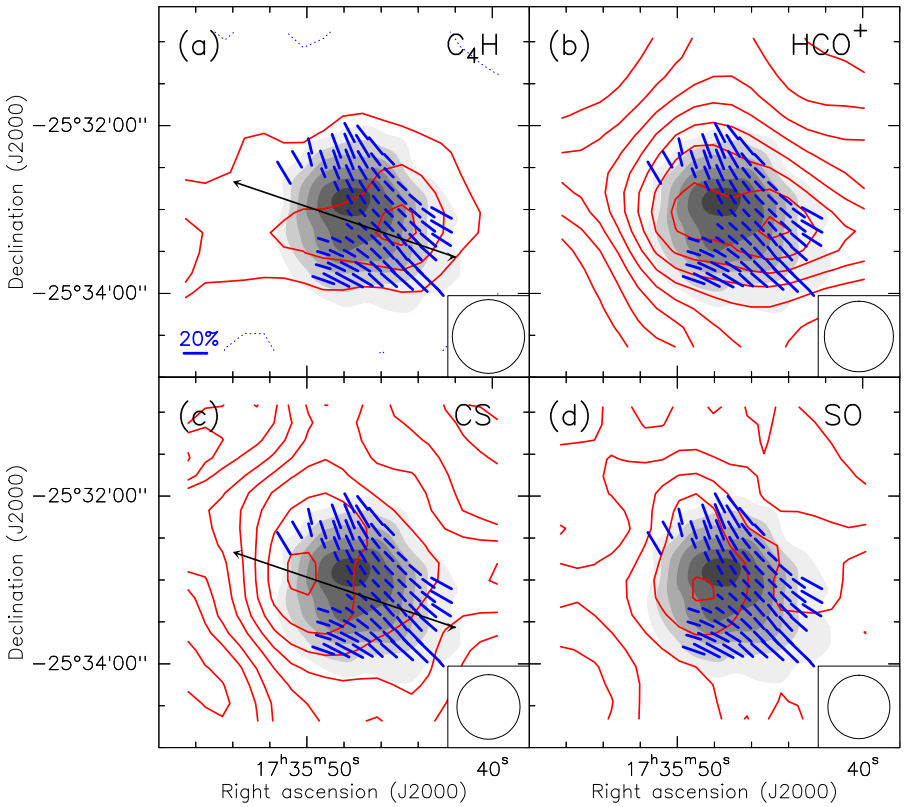

Fig. 2.10 Polarization maps. *Red contours*: averaged intensity maps of (a) C_4H, (b) HCO^+, (c) CS and (d) SO. Contours in panels (a) and (c) are $-3, 3, 6, 9, 12, 15, 20, 25, 30, ...$ times the rms of the maps, 10 mK. Contours in panel (b) and (d) are $10, 20, 30, ...$ and $-3, 3, 6, 9, 12, 15$ times the rms of the maps, 6, and 16 mK. The beam size of each molecular line is shown at the bottom right corner of each panel. *Gray scale*: IRAM 30m MAMBO-II map of the dust continuum emission at 1.2 mm. *Blue segments*: Position angle of the linearly polarized data from Alves et al. (2014). The length of the segments is proportional to the polarization fraction. Black arrows in panels (a) and (c) indicate the 1-D slice shown in Fig. 2.11.

ducing linearly polarized thermal continuum emission (Davis and Greenstein, 1951; Hildebrand, 1988). One of the most important theories for the dust grain alignment is via radiative torques (Dolginov and Mitrofanov, 1976; Draine and Weingartner, 1996, 1997; Lazarian and Hoang, 2007). Thus, the stronger polarized emission to the west also supports the idea of a UV radiation field penetrating into the core from the west which would be affecting not only the polarization properties but also the chemistry in the core (see previous Section).

In Fig. 2.10 we show the emission of 4 molecules peaking to the southwest (C_4H and HCO^+) and to the east (CS and SO) of the dust peak, overlaid with the position angles of the polarization data from Alves et al. (2014). The C_4H and HCO^+ emission seem to correlate with the stronger polarized emission towards the west. On the other hand, the

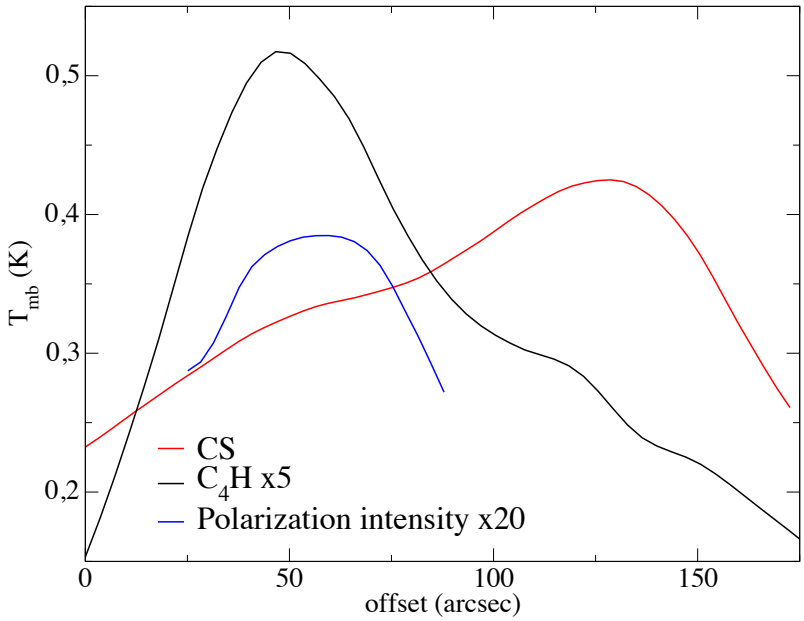

Fig. 2.11 Intensity from CS *(red)*, C_4H *(black)* and polarization intensity *(blue)* along a 1-D slice from the southwest part of the core towards the east passing through the C_4H and CS peaks (see panels (a) and (c) of Fig. 2.10). Both C_4H and the polarization intensity increase at the same positions in the core along the slice. CS shows an anti-correlation with the polarization intensity.

emission peaks of CS and SO seem to present an anti-correlation with the polarized emission. To study further these possible correlations, we performed a 1-D slice across the core passing through the C_4H and CS peaks (black arrows in Fig. 2.10). In Fig. 2.11 we show the polarization intensity (blue) and the emission of C_4H (black) and CS (red) along the slice. The polarization intensity presents a similar distribution and seems to correlate well with the C_4H emission and anti-correlate with the CS emission. To quantify these correlations we performed the statistical tests Kendall's τ and Spearman's ρ[6] and found a good correlation ($\tau = 0.647$, $\rho = 0.804$) between C_4H emission and polarization intensity and anti-correlation values ($\tau = -0.062$, $\rho = -0.058$) between CS and polarization intensity. More observations are necessary to further study these results.

On the other hand, Alves et al. (2014) also find a steep decrease in the polarization efficiency at visual extinctions (A_V) larger than 30 mag. Alves et al. (2014) propose the lack of an internal source of radiation results in a loss of grain alignment with the magnetic field, which is consistent with the theory of dust grain alignment via radiative torques. Our work suggests that depolarization could be produced as a combination of lack of internal source

[6]http://www.statsoft.com/textbook/nonparametric-statistics/

and dust grain growth possibly affected by molecular depletion. Due to the 'grain clustering' yielding to larger grains, the elongated shape of the grains could be distorted. The paramagnetic nuclei of the grains would be surrounded by a thick layer of ice (unpolarized) and the alignment of the grains could be harder to achieve resulting in a depolarized inner region as seen by Alves et al. (2014).

Therefore, we conclude that depletion, grain growth and depolarization seem to be correlated in FeSt 1-457.

2.5.4 Magnetic properties of FeSt 1-457

Previous studies in star-forming cores have shown that magnetic fields can play an important role in their evolution (e.g., Girart et al., 2006).

Magnetic forces could prevent a cloud from collapsing if its mass-to-flux ratio is below the critical value,

$$M/\Phi_B < (M/\Phi_B)_{\rm cr}, \tag{2.7}$$

where M is its mass and $\Phi_B = \pi < B > R^2$ is the magnetic flux through it, derived from the mean magnetic field and the radius of the cloud cross-section perpendicular to the magnetic field. The critical mass-to-flux ratio is $(M/\Phi_B)_{\rm cr} = 1/(2\pi G^{1/2})$ (Nakano and Nakamura, 1978), where G is the gravitational constant. We used the ratio in terms of the column density following Eq. (7) of Pillai et al. (2015)

$$\frac{(M/\Phi_B)}{(M/\Phi_B)_{\rm cr}} = 0.76 \left(\frac{N_{H_2}}{10^{23}\ {\rm cm}^{-2}}\right) \left(\frac{B_{\rm tot}}{1000\ \mu G}\right)^{-1}. \tag{2.8}$$

Frau et al. (2010) obtain a core+cloud column density $N_{H_2} = 47.6 \times 10^{21}$ cm^{-2}. From our Bonnor-Ebert model fit (see Sec. 2.4.1) we found the background visual extinction arising from the surrounding medium ($A_{\rm V}^{\rm bg}$) to be 9.5 mag which corresponds to a column density of 8.9×10^{21} cm^{-2}. Thus, we adopted a column density for the core of 38.7×10^{21} cm^{-2}. On the other hand, we assumed $B_{\rm pos} \sim B_{\rm tot} \sim 45.2$ μG as Alves et al. (2014) find the magnetic field direction mainly onto the plane of sky. We obtained a ratio of 6.5 (magnetically supercritical) which implies that gravity dominates over the magnetic support. Our Bonnor-Ebert model fit showed that the core is gravitationally unstable (see Sec. 2.4.1). Finally, we can see that the magnetic field is not enough to avoid the collapse.

2.5.5 Converging flows at the edge of FeSt 1-457

In panels (m) and (n) of Fig. 2.5 we showed the emission of ^{13}CO (1–0) molecular line. The two panels show two different velocity components. Panel (m), with the velocity component associated to the core (5.8 km s^{-1}), shows a structure very similar to the emission of C^{18}O (1–0) (panel (l)) with strong emission peaking towards the southwest of the core. The other component (panel n) at 3.0 km s^{-1} presents strong emission towards the north and fades away just at the northern edge of the core. In a previous work, Frau et al. (2015) find two filaments with different orientations and velocities colliding at the "bowl" region of the Pipe nebula. The two filaments are oriented with east-west and north-south orientations and at $2-4$ and $6-7$ km s^{-1}, respectively. The two velocity components detected from ^{13}CO (1–0) emission seem to trace the two filaments. Thus, FeSt 1-457 seems to be located just at the converging site of the two filaments and could be the result of such collision.

2.6 Summary

We have used the IRAM 30m telescope and the PdBI to study the chemical and physical properties of the starless core FeSt 1-457 (Core 109) in the Pipe nebula. Our main conclusions are as follows:

1. We fit the hyperfine structure of the N_2H^+ $(1-0)$ IRAM 30m data. This allows to measure with high precision the velocity field and line widths in the core. The N_2H^+ emission shows a clear southwest-northeast velocity gradient of 1.78 km s^{-1} pc^{-1}, and larger line widths (0.3 km s^{-1}) at the southwest part of the map. The typical line widths are $0.17-0.23$ km s^{-1}. The column density map presents an arc-structure around the the 1.2 mm dust continuum peak.

2. Combining both IRAM 30m and PdBI N_2H^+ $(1-0)$ data we can resolve the arc-like structure hinted at the single dish map.

3. The core presents a rich chemistry with emission from early (C_3H_2, HCN, CS) and late-time molecules (e.g., N_2H^+), with a clear chemical spatial differentiation for nitrogen (centrally peaked), oxygen (peaking to the southwest) and sulphurated molecules (peaking to the east).

4. The chemical difference in the core could be due to an external UV radiation field penetrating into the core from the (south)west which could be also affecting the polarization properties. This implies that the core should be close to the edge of the molecular cloud.

5. FeSt 1-457 is well fitted with a Bonnor-Ebert sphere model and introducing a temperature gradient decreasing towards the center from 12 to 6 K. We found the core is gravitationally unstable and that the magnetic field is not enough to stop the collapse.

6. We have analyzed the abundances of the molecular lines using the ARTIST software. For most of the molecules detected (HCN, HCO^+, CH_3OH, CS, SO, ^{13}CO and $C^{18}O$), abundances are best fitted with three values, presenting a clear decrease of abundance of at least 1 or 2 orders of magnitude towards the inner region of the core. This is consistent with chemical models of starless cores, that show that there is a significant depletion of molecules onto the dust grains. On the other hand, N_2H^+, HC_3N and C_3H_2 are well fitted with a constant abundance throughout the core and the abundance of HNC and NH_2D increases in the inner region of the core (at radius $\lesssim 55''$).

Finally, we have seen that depletion of molecules onto the dust grains, grain growth and depolarization take place at the inner region of the core. This strongly suggests that these properties could be correlated in FeSt 1-457.

Chapter 3

Magnetized converging flows towards the hot core in the intermediate/high-mass star-forming region NGC 6334 V

3.1 General overview

Previous observations have led to the consensus that the magnetic (B) field strength is non-negligible during the formation of molecular gas clouds and dense gas filaments, for low- and high-mass star- and cluster-forming regions (e.g., Matthews et al. 2009; Crutcher et al. 2010; Koch et al. 2014; Fissel et al. 2016; Soler et al. 2016; see Li et al. 2014 for a review). However, the role of the magnetic field in the formation and evolution of dense molecular cores (which have sizes of ~ 0.1 pc) is still a matter of debate (e.g., Bertram et al., 2012; Crutcher, 2012; Körtgen and Banerjee, 2015; Li et al., 2014; Vázquez-Semadeni et al., 2011). Its role can be studied observationally by combining high angular resolution ($\sim$few arcseconds) observations of molecular lines with polarimetric observations of dust continuum (e.g., Girart et al., 2013; Hull et al., 2014; Zhang et al., 2014). However, this type of studies has been done only towards a limited sample of star-forming cores. Within this sample, there are cases where the magnetic field is consistent with an hourglass morphology, which is an indication of strong magnetic fields in infalling cores (Fiedler and Mouschovias, 1993; Frau et al., 2011; Galli and Shu, 1993a,b; Nakamura and Li, 2005). Examples include the low- and high-mass star-forming regions NGC1333 IRAS4A (Frau et al., 2011; Girart et al., 2006; Liu et al., 2016), G31.41+0.31 (Girart et al., 2009), W51e2 (Tang et al., 2009b), W51 North (Tang et al., 2013), G35.2-0.74N (Qiu et al., 2013), G240.31+0.07 (Qiu et al., 2014), W43-MM1 (Cortes et al., 2016).

NGC 6334 is one of the nearest high-mass star-forming regions, located at a distance of 1.3 kpc (Chibueze et al., 2014; Reid et al., 2014). The dense molecular gas is dominated by a ∼20 pc long filamentary structure oriented along northeast-southwest direction. Along the filament there are several parsec-scale sites of active star formation (e.g., Li et al., 2015, and references therein). Previous optical and submillimeter polarimetric observations found a coherent magnetic field from cloud to core scales with its main direction approximately perpendicular to the long axis of the dense filament. This led Li et al. (2015) to suggest that NGC 6334 undergoes self-similar fragmentation regulated by the magnetic field.

NGC 6334 V is the southernmost active star-forming site along the large-scale northeast-southwest dense gas filament of NGC 6334. This region was not covered by the multi-scale studies of Li et al. (2015). NGC 6334 V is located at the intersection between the main filament and a smaller filament that extends along the northwest-southeast direction (e.g., André et al., 2016). This characteristic makes the NGC 6334 V star-forming core different from other cores along the main filament. Therefore, the study of this core, at scales similar to Li et al. (2015), can be used to test whether the physical properties of NGC 6334 V are affected by the convergence of these two filaments.

Signposts of recent and ongoing star formation in NGC 6334 V include its high far-infrared luminosity ($L_{bol} \sim 10^4$ $L_\odot$), a CO molecular outflow (Fischer et al., 1982; Kraemer and Jackson, 1995; Zhang et al., 2014) and H_2O and OH masers (Brooks and Whiteoak, 2001; Forster and Caswell, 1989; Raimond and Eliasson, 1969). It also harbors several infrared sources (Harvey and Gatley, 1983; Harvey and Wilking, 1984; Kraemer et al., 1999; Simon et al., 1985) and three faint associated radio sources (Rengarajan and Ho, 1996). Previous studies (Hashimoto et al., 2007; Simpson et al., 2009) suggest the existence of two independent outflows in NGC 6334 V, one oriented east-west along the line of sight and the other with a north-south orientation almost on the plane of the sky. These two outflows could be powered by the infrared sources KDJ3 and KDJ4 (Kraemer et al., 1999).

In this Chapter, we present Submillimeter Array (SMA)[1] spectro-polarimetric observations towards NGC 6334 V at 345 GHz. These observations covered a frequency range that allows us to detect the dust emission with a high signal-to-noise ratio together with linear polarization from the dust emission. Within the frequency range there are various molecular lines (see Section below for more details on the specific lines): dense gas tracers (i. e., sensitive to densities of $\gtrsim 10^6$ cm^{-3} and temperature $\gtrsim 100$ K) and tracers of outflows or shocks. This allows us to characterize the physical properties of the core, and in particular to shed light on the role of the magnetic field.

[1]The Submillimeter Array is a joint project between the Smithsonian Astrophysical Observatory and the Academia Sinica Institute of Astronomy and Astrophysics (Ho et al., 2004).

The details of our observations are given in Sec. 3.2. The observational results are shown in Sec. 3.3. In Sec. 3.4 we present magneto-hydrodynamic (MHD) simulations. Radiative transfer analysis and convolution with the SMA response are performed to properly compare with the observations. Discussion and a summary of the results are given in Sec. 3.5 and 3.6, respectively.

3.2 SMA observations and data reduction

NGC 6334 V was observed with the SMA in the subcompact, compact and extended configurations. These observations were part of the polarization legacy project carried out between 2008 and 2012 in the 345 GHz band to observe the polarization emission of a sample of 21 massive star-forming regions (for an overview of this survey see Zhang et al., 2014). Table 3.1 shows the basic observational parameters and lists the calibrators used during the three tracks. The combined three configurations sample visibilities between $\sim$6 kλ to $\sim$200 kλ. This makes the observations sensitive to scales between $1''$ and $15''$. The phase and pointing center of the observations was RA(J2000)= $17^{\rm h}19^{\rm m}57.40^{\rm s}$, Dec(J2000)= $-35°57'46.0''$. The frequency was approximately centered on the CO (3$-$2) line (345.79599 GHz) in the upper sideband (USB). The correlator consisted of 48 chunks with a bandwidth of 104 MHz each. This provided a total bandwidth (including the USB and the lower side band - LSB) of $\sim$ 8 GHz. We set the correlator to yield a uniform spectral resolution of 128 channels per chunk, providing a channel width of 0.8 MHz or 0.7 km s^{-1} at the observing frequency.

Polarization observations were carried out using quarter-wave plates which convert linear polarization signals to circular ones (see Marrone et al., 2006; Marrone and Rao, 2008, for a more detailed description of the SMA polarimeter and the calibration process). The polarization leakages were measured to an accuracy of 0.1% (Marrone and Rao, 2008). The calibration for absolute flux, passband, and gains were carried out using the MIR IDL software package (Scoville et al., 1993). The images were created using the MIRIAD software package (Sault et al., 1995). We averaged the line-free channels in the LSB and USB to generate the 870 μm continuum. The 870 μm maps were obtained combining the three configurations. We set the ROBUST visibility weighting parameter to 0.5 (Briggs, 1995), which provides a good compromise between angular resolution and sensitivity. The rms noise level of the resulting continuum map (Fig. 3.1) is 5.5 mJy beam^{-1} and the synthesized beam is $2''.15 \times 1''.49$, P.A. $= -2.92°$. To generate the polarization maps we used the IMPOL task in MIRIAD which computes the linearly bias-corrected polarized intensity and position angle from Stokes Q and U (QU) images. We used 3σ as the cutoff for Stokes QU

Table 3.1 SMA observations summary.

Array configuration	subcompact	compact	extended
Observing date	2011 July 2	2011 June 18	2011 July 21
$\tau_{225\mathrm{GHz}}$	0.09	0.06–0.1	0.05
Number of antennas	7	7	8
Flux calibrator	Callisto	Uranus	Callisto
Passband calibrator	3C 279/3C 454.3	3C 279/3C 454.3	3C 279/3C 454.3
Gain calibrator	1733-130	1733-130	1733-130
Polarization calibrator	3C 279/3C 454.3	3C 279/3C 454.3	3C 279/3C 454.3
uv range ($k\lambda$)	6–42	8–80	24–206

(Vaillancourt, 2006) and I images. The rms level for Stokes QU is 3.1 mJy beam^{-1}. The different molecular line maps were also generated using a ROBUST parameter of 0.5, except for the SiO (8−7) line. This line is strong and compact. Thus, we used a ROBUST parameter of −2 (uniform weighting), which provides the best possible angular resolution.

3.3 Results

3.3.1 Morphology

Dust continuum

The upper panel of Fig. 3.1 shows the 870 μm dust continuum emission image. Overplotted are associated infrared and radio sources, as well as OH and H_2O masers. This continuum image reveals asymmetric dense gas structures. They form a well resolved $\sim$ 0.07 pc ($\sim$14,000 au) scale arc-like structure along the east-west direction (measured from the 8σ contour from the 870 μm dust continuum emission), with three distinguishable peaks surrounding a lower density cavity, labeled as N (North), SE (South-East) and HC (Hot Core; see Sec. 3.3.1). Positions, deconvolved sizes, peak intensities, flux densities and mass estimates of the three main peaks are listed in Table 3.2.

Most of the known infrared and radio sources are located either around the 870 μm peak (hot core; e.g., IRS V3 and radio source R E-3), or are inside the cavity.

Based on the VLA observations of the centimeter free-free continuum emission presented in Rengarajan and Ho (1996), we constrain the 870 μm free-free emission to be < 4.7 mJy towards R-E1, R-E2 and R-E3, which is negligible as compared to the detected emission level in Fig. 3.1 (see Table 3.2). Assuming that the 870 μm dust emission is

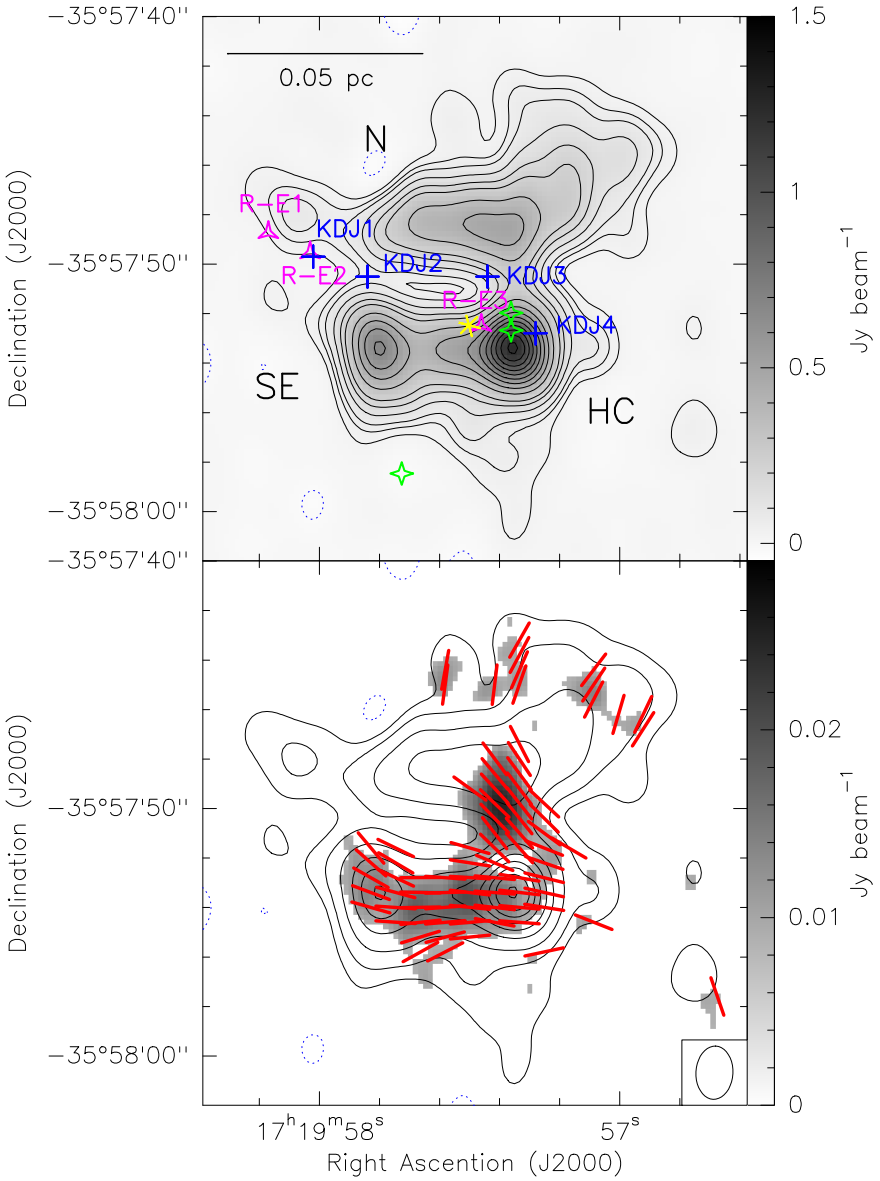

Fig. 3.1 Images of 870 μm continuum observations on NGC 6334 V. *Upper panel*: The gray image and the contours show the 870 μm dust continuum emission. Contour levels are -8, -4, 4, 8, 12, 20, 30, 40, 60, 80, ..., 220 times the rms noise level of the map, 5.5 mJy beam^{-1}. The three main peaks are labeled as N (north), SE (southeast) and HC (hot core). Blue crosses, pink triangles, green stars and yellow asterisk show the positions of infrared (Kraemer et al., 1999), radio (Rengarajan and Ho, 1996), OH maser (Brooks and Whiteoak, 2001; Raimond and Eliasson, 1969) and H_2O maser sources (Forster and Caswell, 1989), respectively. The intensity scale bar (in Jy beam^{-1}) is located at the right side. A scale bar is located at the upper left corner. *Lower panel*: Gray scale image of the 870 μm dust polarization emission overlaid with the contour map of the 870 μm dust continuum emission. Gray scale shows the polarization intensity in Jy beam^{-1}. Red segments are the inferred magnetic field orientations projected on the plane of the sky (i.e., B-segments) using a Nyquist sampling. The synthesized beam is located at the bottom right corner. Polarization intensity and B-segments are only presented where the polarization intensity shows a $>3\sigma$ detection.

optically thin, we estimated the gas+dust masses according to

$$M = R\frac{d^2 S_\nu}{B_\nu(T_d)\kappa_\nu}, \tag{3.1}$$

where d is the distance, S_ν is the flux density, $B_\nu(T_d)$ is the Planck function at the isothermal dust temperature T_d, κ_ν is the dust opacity and the factor R is the gas-to-dust ratio which we assumed to be 100 (Hildebrand, 1983; Lis et al., 1998). We adopted $\kappa_\nu = 2.03$ cm^{2}g^{-1} for thin ice mantles after 10^5 years of coagulation at a gas number density of 10^6 cm^{-3} and for the frequency of our observations (Ossenkopf and Henning, 1994) and we assumed $T_d = 50 - 100$ K (hot core temperatures $\gtrsim 100$ K; e.g., Palau et al., 2011) for the hot core and 30 K for the north (N) and southeast (SE) cores (the average temperature in protostellar cores; e.g., Faúndez et al., 2004; Sánchez-Monge et al., 2013, see Sec. 3.3.2). The resulting masses are given in Table 3.2.

The mass derived from the total 870 μm flux density detected by the SMA is ~ 50 M$_\odot$ for a $T_d = 30$ K. This value is <10% of the mass estimated by Muñoz et al. (2007) based on 1.2 mm dust continuum emission obtained with the SEST SIMBA bolometer array. There are two reasons for this difference. We might be missing some flux due to the interferometric filtering of extended emission, and Muñoz et al. (2007) use an integration area for the flux calculation approximately ten times larger than our work (using an effective radius of 0.86 pc).

Polarization data

It is generally accepted that non-spherical interstellar dust grains are locally aligned with the B-field, with their longest axes being perpendicular to the B-field directions (see Hildebrand et al., 2000, for a review). Therefore, the projected orientation of the B-field can be inferred by rotating the dust linear polarization (i.e., electric field) by 90 degrees (hereafter B-segment for the 90° rotated linear polarization).

The lower panel of Fig. 3.1 shows the polarization map from the 870 μm continuum observations.

The projected magnetic field shows an east-west orientation following the dust morphology, from the south-east (SE) continuum peak towards the hot core region. There are also several detections at the northern part of the dust continuum emission showing a near north-south orientation. This northern component of the magnetic field seems to connect to the hot core position through several detections presenting a northeast-southwest orientation.

The histogram of the B-segment position angles (see upper panel of Fig. 3.2) shows a disperse distribution due to the changes in the morphology of the magnetic field. We

Table 3.2 Parameters of the sources detected with the SMA at 870 μm dust continuum emission.

Source	Position[a]		Deconv.ang.size[a]	P.A.[a]	$I_\nu^{\rm peak}$ [a]	S_ν [a,b]	Mass[c]
	α(J2000)	δ(J2000)	($''\times''$)	($^\circ$)	(Jy Beam^{-1})	(Jy)	($M_\odot$)
HC	17:19:57.364	−35:57:53.47	$2.9\pm0.6\times1.66\pm0.6$	-89 ± 41	1.27 ± 0.16	3.6 ± 0.7	4-9
N core	17:19:57.408	−35:57:48.55	$6.2\pm2.3\times2.62\pm1.2$	85 ± 18	0.50 ± 0.02	3.3 ± 0.7	16
SE core	17:19:57.792	−35:57:53.50	$2.4\pm0.4\times1.78\pm0.3$	45 ± 20	0.80 ± 0.04	1.9 ± 0.4	9

[a] Position, deconvolved size, position angle (P.A.), peak intensity, flux density and the respective uncertainties derived from fitting a 2D Gaussian to each source using the IMFIT task from MIRIAD. Peak intensities and flux densities are corrected for the primary beam response.

[b] Error in flux density is calculated as $\sqrt{(\sigma\,\theta_{\rm source}/\theta_{\rm beam})^2+(\sigma_{\rm flux-scale})^2}$ (Beltrán et al., 2001; Palau et al., 2013), where σ is the rms of the map, $\theta_{\rm source}$ and $\theta_{\rm beam}$ are the sizes of the source and the beam, respectively, and $\sigma_{\rm flux-scale}$ is the error in the flux scale, which takes into account the uncertainty on the calibration applied to the flux density of the source ($S_\nu\times\%_{\rm uncertainty}$) which we assumed to be 20%.

[c] Masses derived assuming a dust mass opacity coefficient of 2.03 cm^{-2}g^{-1} (for thin ice mantles after 10^5 years of coagulation at a gas density of 10^6 cm^{-3}, Ossenkopf and Henning, 1994), a dust temperature of 50 and 100 K for the hot core (HC) and 30 K for the north (N) and southeast (SE) cores. The uncertainty in the masses due to the opacity law and temperature is estimated to be a factor of 4.

identified two major orientations, at $\sim 90^\circ$ (east-west component) and $\sim 50^\circ$ (northeast-southwest component) which seem to be converging at the hot core region. The northern component at $\sim 160^\circ$ (north-south) is also apparent as a separate peak.

Molecular lines

We have detected 24 molecular lines in the 8 GHz band. Table 3.3 lists the frequency and the energy of the upper level (E_U) for each transition. We found that the emission from several molecular transitions with E_U between $\sim 100-400$ K spatially coincides with the strongest dust continuum peak (see Fig. 3.3 and Fig. 3.5), including transitions from SO_2, $^{34}SO_2$, HC_3N, CH_3OH, CH_3OCH_3 and CH_3OCHO. Thus, these molecular transitions likely trace a hot molecular core.

In Fig. 3.3 we present the moment 0 (integrated intensity) maps of $H^{13}CO^+$ (4–3), CH_3OH 7(1,7)−6(1,6), and CH_3OCHO 31(0,31)−30(1,30), which have upper level energies of 41 K, 79 K, and 260 K, respectively. The very different excitation conditions for these molecular line transitions trace different regions in the molecular gas, which show a variety of morphologies. $H^{13}CO^+$ (4−3) (upper panel) is a good tracer of the dense and relatively cold gas and traces the extended dense core of NGC 6334 V. It shows two main peaks forming a ring-like structure with lack of emission at the center of the ring, coinciding with the dust continuum cavity. CH_3OH 7(1,7)−6(1,6) (middle panel) traces warmer gas, and it is generally a good hot core tracer. It presents strong emission at the hot core position and also traces a more compact region of the dense core, forming a ring-like structure, as the $H^{13}CO^+$ molecular line.

Many of the infrared and radio sources found in the region are located where we find a deficit of molecular emission in both $H^{13}CO^+$ and CH_3OH (center of the ring). In addition, the cavity is filled with 4.5 μm emission (see Fig. 3.4). The origin of this extended emission is unclear. Possible emission mechanisms could be scattered continuum emission in outflow cavities (e.g., Qiu et al., 2008; Takami et al., 2012), H_2 emission and CO emission from shocks (e.g., Davis et al., 2007; Noriega-Crespo et al., 2004; Smith et al., 2006; Takami et al., 2012). In any case, the 4.5 μm emission is likely to be a signpost of a cavity generated by a still active outflow.

Finally, in the lower panel of Fig. 3.3, we present a high-excitation transition (E_U=260 K) of CH_3OCHO which shows more compact emission elongated along an east-west direction, centered only at the hot core region.

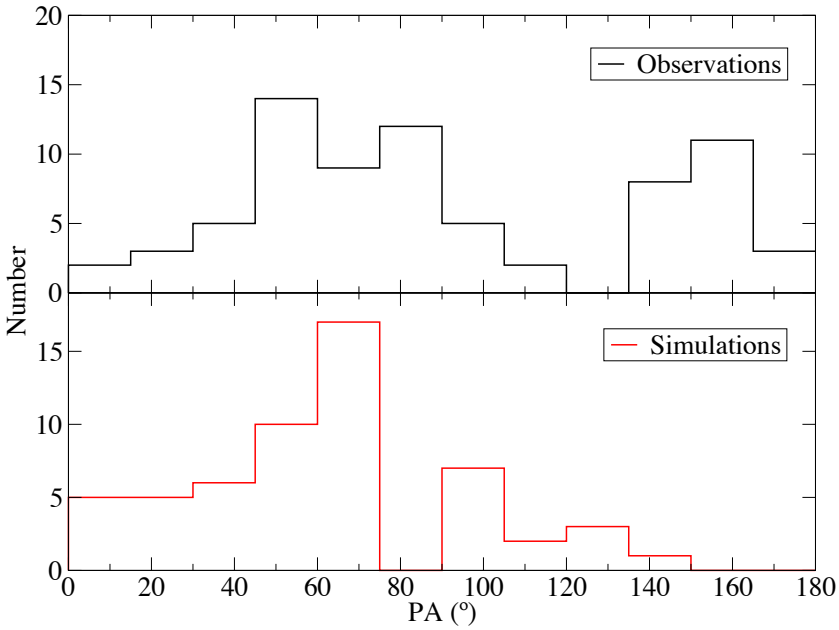

Fig. 3.2 *Upper panel*: Distribution of position angles of the magnetic field segments shown in Fig. 3.1 for a polarized emission cutoff of 3σ. *Lower panel*: Distribution of position angles of the magnetic field segments produced by the simulations (see lower panel of Fig. 3.8).

3.3.2 Kinematics

A Gaussian fit to the averaged spectrum of $H^{13}CO^+$ (4−3) suggests that the systemic velocity of NGC 6334 V is -5.7 km s^{-1}. Therefore, we use this value for the following kinematic analysis.

Velocity gradients and mass estimates

A comparison between the different gas tracers can provide clues about the kinematics from larger (extended dense core) to smaller (hot core) scales. Figure 3.5 shows the intensity-weighted averaged velocity maps (i.e., moment 1 maps) of the same molecular lines shown in Fig. 3.3. The extended dense core tracers $H^{13}CO^+$ and CH_3OH (upper and middle panels, respectively) present a clear east-west velocity gradient from -8 to -5 km s^{-1}. The velocity structure presents a certain symmetry centered at the hot core region. To know if the observed gas belongs to a gravitationally bound system, we estimate the needed minimum mass associated to the observed velocity gradient. The maximum velocity for an object accelerated in a gravitationally bound system is given by $v_{\rm max} = (2GM/R)^{1/2}$ where G is the gravitational constant, R is the distance to the gravitational center and M is its mass.

Table 3.3 Molecular lines.

Molecular line	Transition	Frequency (GHz)	E_U (K)
Hot core tracers			
SO_2	21(2,20)−21(1,21)	332.09143	220
SO_2	16(4,12)−16(3,13)	346.52388	164
SO_2	19(1,19)−18(0,18)	346.65217	168
$^{34}SO_2$	16(4,12)−16(3,13)	332.83622	163
$^{34}SO_2$	19(1,19)−18(0,18)	344.58104	168
$^{34}SO_2$	11(4,8)−11(3,9)	344.99816	99
$^{34}SO_2$	8(4,4)−8(3,5)	345.16866	71
^{34}SO	7(8)−6(7)	333.90098	80
CH_3OH	18(2,16)−17(3,14)	344.10913	419
CH_3OH	19(1,19)−18(2,16)++	344.44390	451
CH_3OCHO	31(0,31)−30(1,30)	333.44902	260
CH_3OCH_3	19(1,19)−18(0,18)AA	344.35806	167
CH_3OCH_3	11(3,9)−10(2,8)EE	344.51538	73
HC_3N	J=38−37	345.60901	323
Dense core tracers			
SO	8(8)−7(7)	344.31061	87
SO_2	4(3,1)−3(2,2)	332.50524	31
SO_2	13(2,12)−12(1,11)	345.33854	93
CH_3OH	7(1,7)−6(1,6)	335.58200	79
$HC^{15}N$	(4−3)	344.20011	41
NS	J=15/2−13/2	346.22116	71
$H^{13}CO^+$	(4−3)	346.99835	41
Outflow tracers			
CO	(3−2)	345.7959	33
SiO	(8−7)	347.33058	75

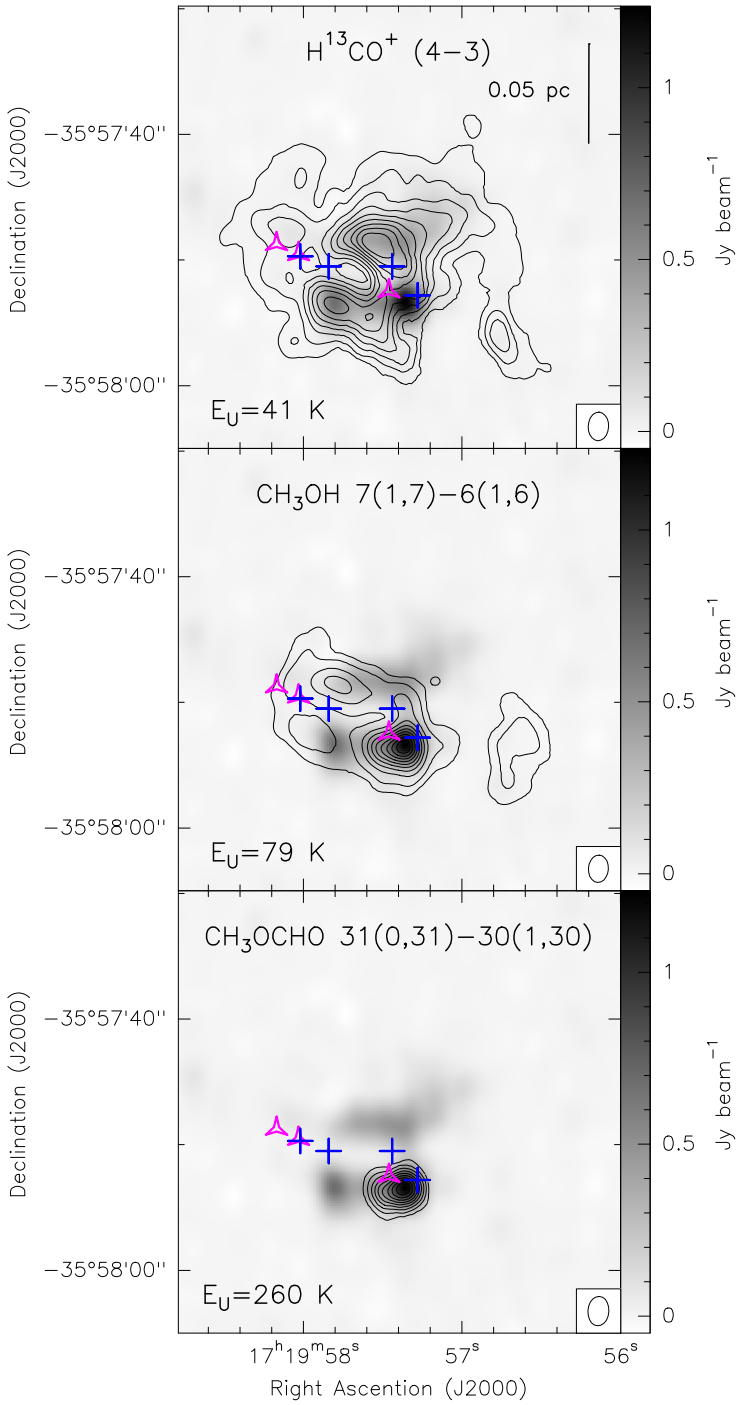

Fig. 3.3 Gray scale image of the 870 μm dust continuum emission overlaid with the contour maps of the velocity integrated emission (i.e., moment 0 maps) of selected molecular line tracers. *Upper panel*: Contours: $H^{13}CO^+$ (4−3). Contour levels are 10, 20, 30, ..., 90 percent of the peak value, 11.2 Jy beam^{-1} km s^{-1}. The synthesized beam located at the bottom right is $2.28'' \times 1.57''$, P.A.$= -2.72°$. *Middle panel*: Contours: CH_3OH 7(1,7)−6(1,6). Contour levels are 5, 10, 20, 30, ..., 90 percent of the peak value, 37.1 Jy beam^{-1} km s^{-1}. The synthesized beam located at the bottom right is $2.19'' \times 1.54''$, P.A.$= -3.45°$. *Lower panel*: Contours: CH_3OCHO 31(0,31)−30(1,30). Contour levels are 10, 20, 30, ..., 90 percent of the peak value, 11.1 Jy beam^{-1} km s^{-1}. The synthesized beam located at the bottom right is $2.35'' \times 1.62''$, P.A.$= -3.17°$. Blue crosses and pink triangles are labeled as in Fig 3.1.

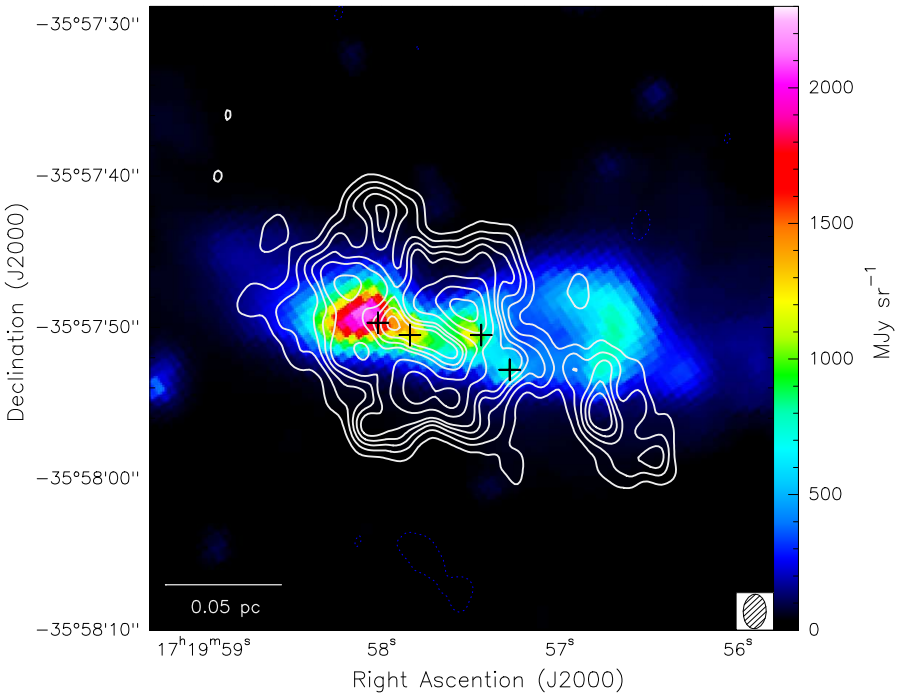

Fig. 3.4 *Color scale*: Spitzer 4.5 μm image. *Contours*: intensity of $H^{13}CO^+$ (4−3) at the systemic velocity, −5.7 km s^{-1}. Contour levels are −4, 4, 8, 12, 16, 20, 30, 40, 50, 60 times the rms noise level, 0.06 Jy beam^{-1}. The synthesized beam located at the bottom right corner is $2''.28 \times 1''.57$, P.A.$= -2.72°$. Black crosses show the positions of infrared sources (Kraemer et al., 1999).

Adopting the gravitational center as the center of the velocity gradient located at the hot core position and using a distance of $6''$ and a velocity of 2 km s^{-1} from the observed velocity gradient, we derive a mass of ~ 18 M$_\odot$. Note that the radial velocity is a lower limit of the total velocity. This mass is lower than the mass estimated from the dust continuum emission, which is a lower limit considering that we are filtering extended emission with the SMA (see Sec. 3.3.1), and thus, we consider the system to be gravitationally bound.

The hot core tracer CH_3OCHO also presents a clear velocity gradient following the orientation of the larger-scale velocity field. The intermediate velocity −6.5 km s^{-1} is shifted from the dust peak position $0.5''$ or 650 au towards the east (several transitions of CH_3OH, CH_3OCH_3, $^{34}SO_2$ and SO_2 also present the same velocity field). The velocity gradient is also compatible with a gravitationally bound system, with an enclosed mass of ~ 6 M$_\odot$ (using $R = 2''$ and $v = 2$ km s^{-1}). The lower limit of the hot core mass obtained from the dust continuum emission is ∼4–9 M$_\odot$.

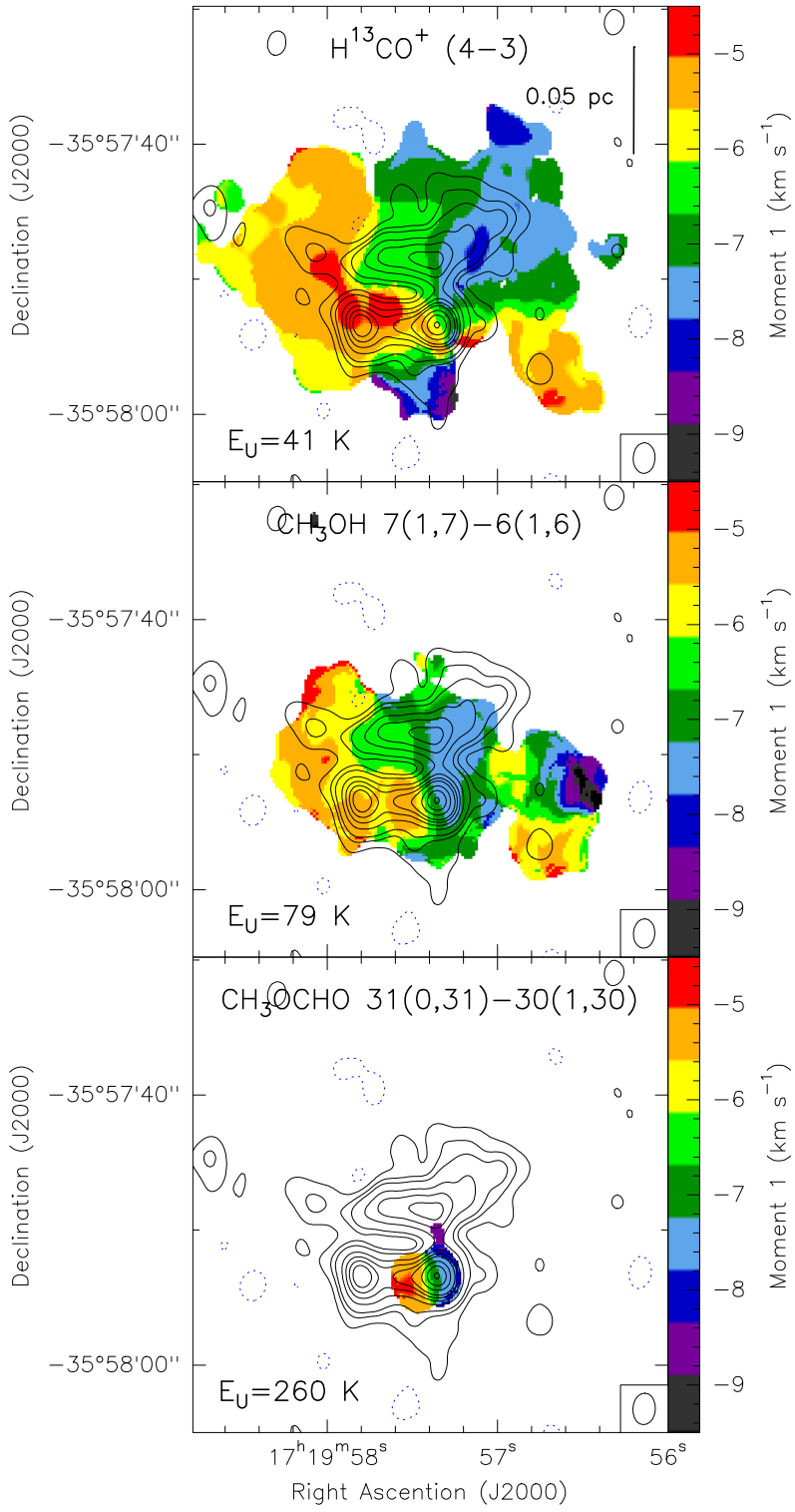

Fig. 3.5 Contour map of the 870 μm dust continuum emission overlaid with the intensity-weighted average velocity (i.e., moment 1) images (color scale) of the following molecular lines: $H^{13}CO^+$ (4−3) (*upper panel*), CH_3OH 7(1,7)−6(1,6) (*middle panel*) and of CH_3OCHO 31(0,31)−30(1,30) (*lower panel*). Synthesized beams of the molecular line images are shown in the bottom right corners of the panels.

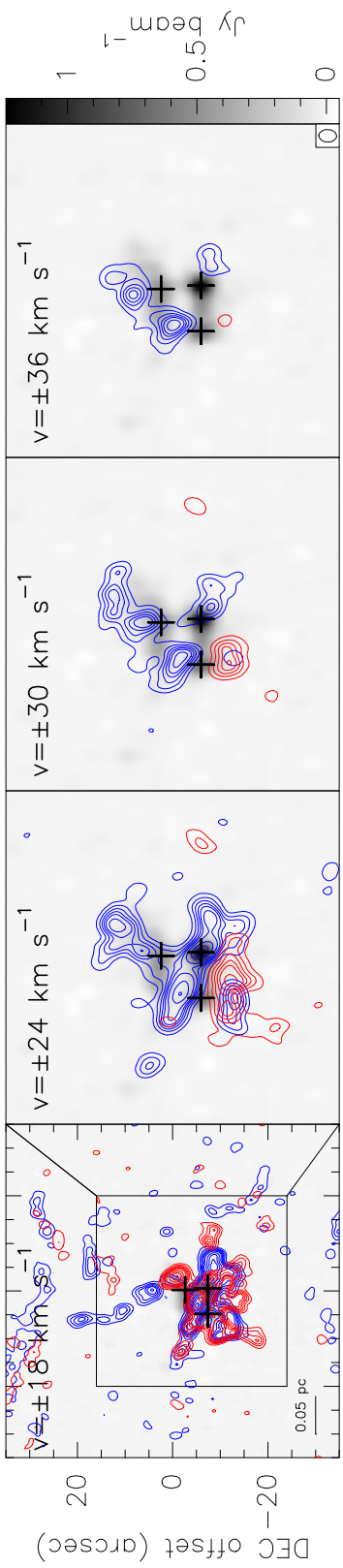

Fig. 3.6 Velocity channel maps of CO (3–2). *Red and blue contours*: CO (3–2) emission. Individual panels present emission at various velocities relative to the systemic velocity v_{lsr}=−5.7 km s^{-1}. Contour levels are −3, 3, 6, 9, 12, 15, 20, 30, 40, ..., 70 times the rms noise level 90 mJy beam^{-1}. The synthesized beam located at the bottom right corner of the last panel is 2.13″ × 1.50″, P.A.= −2.16°. *Gray scale:* 870 μm dust continuum image. The black crosses indicate the three dust continuum peaks (N, SE and HC). A scale bar is located at the left bottom of the first panel. The black square in the first panel indicates the field of view of the rest of the panels.

High-velocity gas

Figure 3.6 shows the red- and blue-shifted CO (3−2) emission at velocities of ±18, ±24, ±30 and ±36 km s^{-1} from the systemic velocity, −5.7 km s^{-1}. At these high velocities, the CO (3−2) is tracing molecular outflows. The first panel (±18 km s^{-1}) shows a very complicated structure with red- and blue-shifted emission spread all over the dust continuum. In the second panel (±24 km s^{-1}), we can distinguish collimated blue-shifted emission along the dust continuum cavity. This emission suggests that the high-velocity gas may have produced the observed cavity. Furthermore, in this panel, we observe blue- and red-shifted emission extended towards the north and south of the hot core position, respectively, in agreement with the larger-scale previously reported CO outflow (Kraemer and Jackson, 1995; Zhang et al., 2014). This emission is oriented almost perpendicular to the velocity gradient seen at the hot core region (see bottom panel of Fig. 3.5). Note that outflow powering source candidates, KDJ3 and KDJ4 (Hashimoto et al., 2007; Kraemer et al., 1999; Simpson et al., 2009), are located close to the hot core position (see Fig. 3.1). KDJ3 does not have dust continuum emission associated as it is located near the dust cavity. On the other hand, KDJ4 seems to be a younger object than KDJ3 and a better outflow powering source candidate as it coincides well with the hot core dust continuum peak. The highest outflow velocities, at ±30 and ±36 km s^{-1} in the last two panels of Fig. 3.6, show red-shifted emission near the southeast continuum peak (SE) and blue-shifted emission towards the hot core region, the northern continuum peak and the dust cavity. Especially in the third panel (at ±30 km s^{-1}), it seems that the southeast (SE) and north (N) cores are associated with high-velocity gas. Thus, even though the CO high-velocity emission presents a very complicated structure, it suggests the presence of at least two or three independent outflows. Multiple molecular outflows associated with a massive dense core have been previously reported in several high-mass star-forming regions (e.g. Fernández-López et al., 2013; Girart et al., 2013; Naranjo-Romero et al., 2012).

3.4 Analysis

3.4.1 Converging flows

As we have seen in Sec. 3.3.2, the molecular dense core traced by $H^{13}CO^+$ and CH_3OH presents a velocity gradient with a certain symmetry centered at the hot core region (see upper and middle panels in Fig. 3.5). Figure 3.7a shows the blue- and red-shifted integrated emission of $H^{13}CO^+$ (4–3) showing two filamentary structures at the eastern and northern parts of the hot core. Both velocity structures seem to converge to the hot core. At the

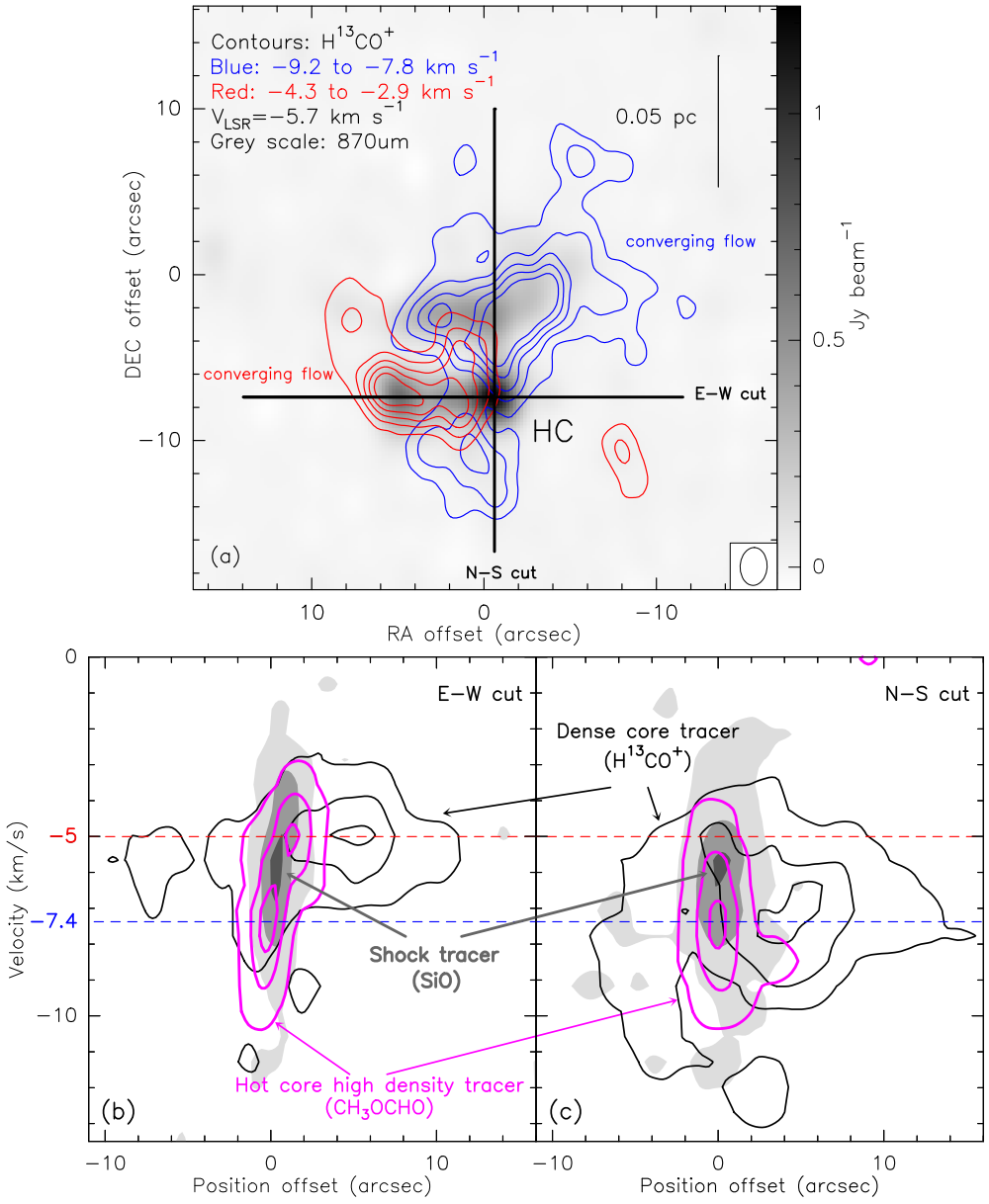

Fig. 3.7 *Panel (a)*: Blue and red contours: averaged emission from blue and redshifted channels of $H^{13}CO^+$ (4–3) displaying the two flow components. Contours are 4, 8, 12, 16, 20 times the rms noise level of the map, 60 mJy beam^{-1}. The synthesized beam is located at the bottom right corner. Black solid lines show position-velocity cuts that are shown in panels (b) and (c). We can see that $H^{13}CO^+$ does not trace the hot core as seen also in other studies (e.g., Girart et al. 2013). Gray scale: 870 μm dust continuum emission. *Panel (b)*: E-W position velocity cuts along the $H^{13}CO^+$ (4–3) (blue), CH_3OCHO 31(0,31)−30(1,30) (pink) and SiO (8–7) (gray scale) line emission passing through the hot core. Contours are 10, 50 and 90 percent of the peak values 4.0 Jy beam^{-1} ($H^{13}CO^+$), 2.9 Jy beam^{-1} (CH_3OCHO) and 1.5 Jy beam^{-1} (SiO). *Panel (c)*: same as panel (b) but along N-S position velocity cuts. Dashed horizontal lines indicate the two velocity components at −5 and −7.4 km s^{-1}.

hot core region, the velocity gradient follows the orientation of the larger-scale velocity field (see Fig. 3.5). As the center of the velocity gradient is shifted from the dust peak, it is probably not only due to rotation but other motions that can affect it, such as infalling motions.

In Fig. 3.7b and c we show two position-velocity diagrams, along the east-west and north-south direction centered at the hot core region, to compare the kinematics from the extended dense core (traced by $H^{13}CO^+$) and the hot core region (traced by CH_3OCHO). Both dense core and hot core tracers show the same two distinctive velocity components, one at -5.0 km s^{-1} and another one at -7.4 km s^{-1}. In addition, we did the same position-velocity cuts towards the shock tracer SiO (8–7). The SiO emission is a signpost of strong shocks. It has, however, also been detected at velocities close to the systemic velocity without a clear association to protostellar outflow activity (Jiménez-Serra et al., 2010; Nguyen-Lu'o'ng et al., 2013). In these cases, SiO can be produced in low-velocity shocks (e.g. Duarte-Cabral et al., 2014; Girart et al., 2016). As shown in gray scale in Fig. 3.7b and c, SiO presents a velocity component just at an intermediate velocity of ~ -6.0 km s^{-1} and at the dust continuum peak position, suggesting that there could be interaction between the two filamentary structures precisely at the hot core region. Such a converging flow toward a hot core was also reported in W33A by Galván-Madrid et al. (2010).

Furthermore, the magnetic field distribution described in Sec. 3.3.1 also shows a "bimodal converging" pattern towards the hot core. In the upper panel of Fig. 3.8 we overlaid the moment 1 map of $H^{13}CO^+$ with the magnetic field distribution. We used the polarization detections from only compact and subcompact configurations as the polarized emission is stronger than with all three configurations combined. The morphology of the magnetic field is very well correlated with the two velocity components shown by the $H^{13}CO^+$ velocity field, suggesting that the magnetic field could be being dragged by the gas dynamics. Previous observations of the B-type binary-forming region G192.16-3.84 (Liu et al., 2013a) have shown that the magnetic field is also dragged by the gravitationally dominant infall and rotational motions, where the magnetic field orientation is approximately parallel to the velocity gradient of the gas.

The combination of these results shows how the gas seems to be infalling from the larger-scale dense core of NGC 6334 V towards the higher-density hot core region through two distinctive converging flows dragging along the magnetic field whose strength seems to have been overcome by gravity.

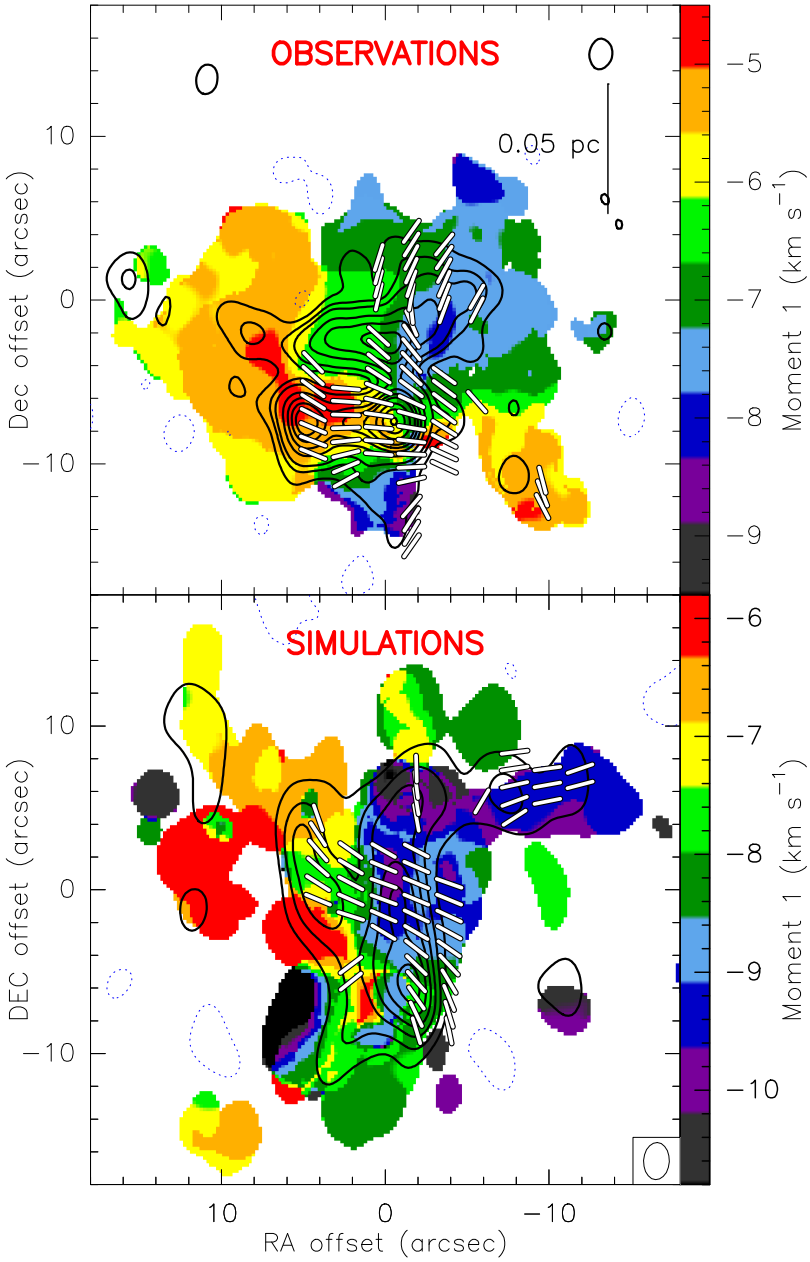

Fig. 3.8 A comparison of the observed dense gas distribution, the velocity field, and the B-segment orientations, with the simulated ones. *Upper panel*: SMA observations. White segments: Magnetic field orientations projected on the plane of the sky (only compact and subcompact configurations). Color scale: Moment 1 map of $H^{13}CO^+$ (4−3). Black contours: 870 μm dust continuum emission. *Lower panel*: Simulations convolved with SMA response. Color scale: $H^{13}CO^+$ (4−3) moment 1 map (velocity field) from ARTIST. The synthesized beam is located at the bottom right corner. White segments: Magnetic field orientations obtained with the DustPol module of ARTIST. Black contours: Simulated 870 μm dust continuum emission.

3.4.2 Synthetic observations

Our observational analysis so far points out that the gas is converging towards the hot core through two main infalling flow components, suggesting that gravity could play a major role in the dynamics of intermediate/massive star-forming regions. However, our interpretation can be biased due to several observational effects. First, certain information has been lost when projecting a 3-dimensional density distribution onto a 2-dimensional plane. In addition, the vector fields (e.g., B-field, mean velocity, etc) were smeared due to the integration along the line of sight. Moreover, the interferometric observations of molecular lines are biased by the excitation conditions and the incomplete sampling in the Fourier domain. To facilitate the test of whether or not the observational results are indeed consistent with our interpretation, we have carried out 3-D numerical magnetohydrodynamic (MHD) simulations for massive star-forming regions which are dominated by gravity. We produced synthetic observational results based on these simulations, to make a consistent comparison with the observational results of SMA.

Numerical simulation

We carry out a 3-D numerical simulation of a massive, compact molecular cloud, similar to that presented in Ballesteros-Paredes et al. (2015), although with a different numerical scheme: rather than the Lagrangian smoothed particle hydrodynamical code used before, we use the Eulerian adaptive mesh refinement (AMR) FLASH (version 2.5) code (Fryxell et al., 2000) in a magneto-hydrodynamical regime. As in Ballesteros-Paredes et al. (2015), we include self-gravity, and the formation of sink particles, in an initially turbulent velocity field which is let to evolve freely, i.e., no turbulent forcing is imposed. The simulation is isothermal in order to isolate the thermal effects on the cloud evolution. We also did not include radiative feedback or stellar heating from the sink particles in order to understand the very early stages of the molecular cloud collapse.

The initial conditions are as follows. We consider a numerical box of 1 pc per side containing 1,000 $M_\odot$ of molecular gas. The mass in the box is distributed homogeneously, with a number density of $n_0 = 1.7 \times 10^4\,\mathrm{cm}^{-3}$. The free-fall time for this configuration is 256,000 yr. Following the prescription by, e.g., Stone et al. (1998), we included a pure rotational velocity spectrum with random phases and amplitudes that peak at wave numbers $k = 4\pi/L_0$, where L_0 is the linear size of the box. The resulting initial velocity field was, thus, an incompressible supersonic turbulent fluid, with an rms Mach number of $\mathscr{M}_{\mathrm{rms}} = 8$. No forcing at later times is imposed.

The magnetic field is initially uniform along the x-direction with a strength of $50\,\mu$G, which is consistent with magnetic field intensities at densities of the order of n_0 (see e.g., Crutcher, 2012). Our box is, thus, magnetically supercritical, with a mass-to-flux ratio, μ, 6.7 times the critical value, $\mu_{\rm crit} = (4\pi^2 G)^{-1/2}$ (see e.g., Nakano and Nakamura, 1978), and prone to gravitational collapse as soon as the initial turbulent field is dissipated.

For the dynamical mesh refinement, we use a Jeans criterion in which we resolve the local Jeans length with at least 8 grid cells in order to prevent spurious fragmentation (Truelove et al., 1997). Thus, the numerical grid is refined to reach a maximum resolution of $\Delta x \sim 9.8 \times 10^{-4}\,$pc ($\sim 201\,$au). Once the maximum refinement level is reached in a given cell, no further refinement is performed and a sink particle can be formed when the density in this cell exceeds a threshold density, $n_{\rm thr} = 1.7 \times 10^7\,{\rm cm}^{-3}$. The sink particles can then accrete mass from their surroundings (within an accretion radius of $\sim 2.5\Delta x$), increasing their mass. The numerical scheme for creation of sinks and further mass accretion is that of Federrath et al. (2010).

We run the simulation until 0.9 times the free-fall time ($t_{\rm ff}$) and we compare the numerical model with the observations at this point, because gravity dominates the gas dynamics. In general terms, the evolution can be considered quite similar to that shown in Ballesteros-Paredes et al. (2015): the initial supersonic velocity fluctuations shock and rapidly dissipate their kinetic energy, the gas then collapses in a global but hierarchical and chaotic way forming a complex network of cores and filaments, carrying with them the magnetic field lines. The time evolution of the simulation is illustrated in Fig. 3.9, which shows column density maps in the $x-y$ plane at $t = 0.1, 0.3, 0.6$ and $0.9\ t_{\rm ff}$. As it can be seen, the first time steps are dominated by density fluctuations that grow in mass and merge as collapse proceeds. These density fluctuations are elongated mostly in the y-direction because the initial magnetic field is aligned along constant values of x, allowing the mass to flow in the y-direction more freely than in the perpendicular directions (in contrast to the initial fluctuations of the non-magnetic simulations presented earlier in Ballesteros-Paredes et al., 2015). Nevertheless, as the collapse proceeds, no preferred elongation is seen in the column density maps, and the final structure is quite similar to the non-magnetic case (see Fig. 1 in Ballesteros-Paredes et al., 2015), suggesting that, indeed, gravity is driving the dynamics of the dense collapsing core.

The onset of star formation (sink formation) occurs at $0.75\,t_{\rm ff}$, once the cloud is globally collapsing. We compare the stellar content from both the simulation and observations in Sec. 3.5.1.

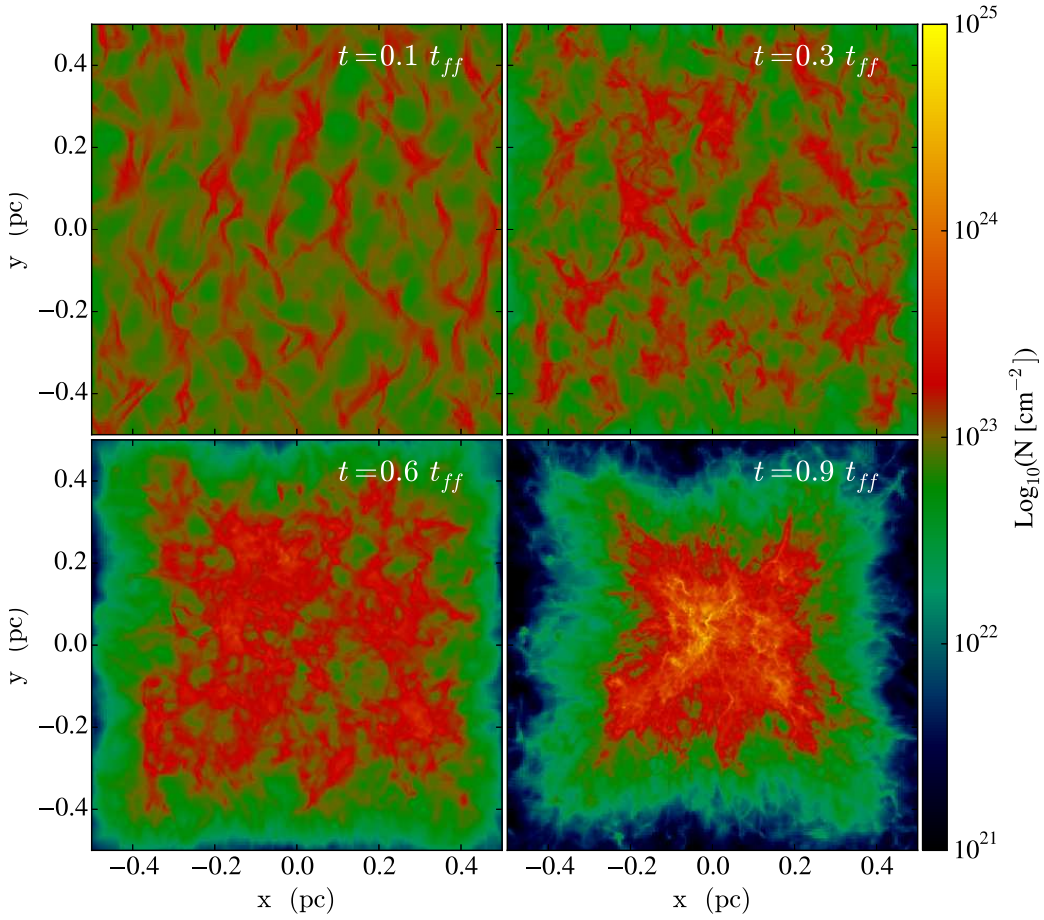

Fig. 3.9 Column density maps at 0.1, 0.3, 0.6 and 0.9 free-fall times ($t_{\rm ff}$). Note that the early evolution is dominated by turbulent motions, which dissipate energy through shocks, forming thus filamentary structures. Once the turbulence is dissipated, the gravity takes over and the gas is in free-fall dragging the magnetic field lines. Note that the sinks particles (which start to form at 0.75 $t_{\rm ff}$) are not shown at 0.9 $t_{\rm ff}$ in order to appreciate better the complex structure of the collapsing gas.

Finally, to compare the numerical model with the simulations, we extract, at $0.9\,t_{\rm ff}$, the central cubic subregion of 0.3 pc per side in order to match the angular size with the observations (see Fig. 3.10).

ARTIST

We utilize ARTIST[2] (Adaptable Radiative Transfer Innovations for Submillimetre Telescopes; Brinch and Hogerheijde, 2010) to generate a synthetic intensity cube (RA, DEC, $v_{\rm LSR}$) of the (4–3) transition of $H^{13}CO^+$ from the 3-D structure generated in the numerical

[2]URL: http://youngstars.nbi.dk/artist/Welcome.html

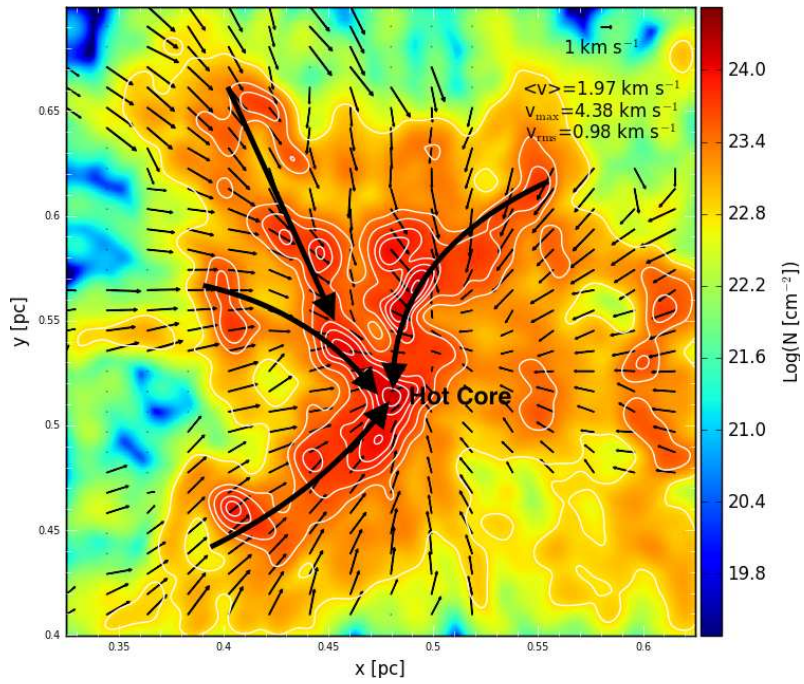

Fig. 3.10 Column density map of the central 0.3 pc subregion of the numerical simulation at $0.9\,t_{\rm ff}$ (see the lower right panel of Fig. 3.9). Note that the column density is convolved at the resolution of the observations. The thin black arrows represent the integrated velocity field (weighted by density) along the line of sight (z-direction), whereas the thick black arrows highlight the filamentary structures converging at the densest "hot core" region.

simulation. We take a fractional abundance of 3×10^{-11} with respect to the H_2 density (see e.g., Girart et al., 2000), and we assume a dust temperature of 30 K, a source distance of 1.3 kpc, and no inclination/rotation, i.e., face-on view. The angular resolution is $0.05''$.

Additionally, we utilize the DustPol module of ARTIST (Padovani et al., 2012), to generate a synthetic map of the dust polarized emission at 870 μm on the plane of the sky from the density distribution of the magnetic field generated in the numerical simulation.

SMA response

The numerical simulations and the $H^{13}CO^+$ (4−3) ARTIST spectral cube were convolved with the SMA interferometric response for a realistic comparison with the observations. This was done using the UVMODEL task in MIRIAD by converting the modeled maps to visibilities using the same distribution of the visibilities in the (u, v)-plane as in the NGC 6334 V SMA observations. Later, the same parameters were used to create the final maps (e.g., pixel size, ROBUST parameter, ...). For the simulated maps, the procedure was followed independently for Stokes I, Q, and U. Once the synthetic SMA-like Stokes I, Q, U maps were

obtained, the polarization intensity and position angles were obtained in the same way as for the SMA data.

3.4.3 Observations vs. simulation: polarization angular dispersion function comparison

From dust polarization observations we are able to estimate the magnetic field strength on the plane of the sky using the Chandrasekhar-Fermi (CF) equation (Chandrasekhar and Fermi, 1953),

$$\frac{\delta B}{B} \simeq \frac{\sigma_v}{V_A}, \tag{3.2}$$

where B is the strength of the magnetic field, δB the variation of B, $V_A = B/\sqrt{4\pi\rho}$ is the Alfvén speed at mass density ρ, and σ_v is the velocity dispersion along the line of sight. Different statistical methods have been developed in order to avoid some of the CF method caveats (Franco et al., 2010; Hildebrand et al., 2009; Houde et al., 2011, 2009; Koch et al., 2010).

Assuming two statistically independent components of B (the large-scale magnetic field B_0 and the turbulent magnetic field B_t), Houde et al. (2009) suggest that the ratio of B_t to B_0 can be evaluated from the angular dispersion function that accounts for the polarization angle differences ($\Delta\Phi$) as a function of the distance (l) between the measured positions.

The angular dispersion function can be written as

$$1 - \langle \cos[\Delta\Phi(l)] \rangle \simeq \frac{\langle B_t^2 \rangle}{\langle B_0^2 \rangle} \frac{1}{N} \left[1 - \mathrm{e}^{-l^2/2(\delta^2+2W^2)} \right] + \sum_{j=1}^{\infty} a'_{2j}\, l^{2j}, \tag{3.3}$$

where

$$N = \left[\frac{(\delta^2 + 2W^2)\Delta'}{\sqrt{2\pi}\delta^3} \right] \tag{3.4}$$

is the number of turbulent cells along the line of sight, δ is the magnetic field turbulent correlation length (assumed to be much smaller than the thickness of the cloud Δ'), W is the synthesized beam (i.e., FWHM/$\sqrt{8\, ln(2)}$), and the summation is a Taylor expansion representing the large-scale magnetic field component which does not involve turbulence. For displacements l less than a few times W we keep only the first l^2 term in the Taylor expansion. We do not use Houde et al. (2016) approximation which takes into account the interferometer filtering effect, as we want to simplify the variables to perform a qualitative comparison between the observational data and the simulation. In addition, the simulation

Table 3.4 Angular dispersion function fit parameters.

Parameters	SMA observations	Simulations
δ[a] (mpc)	17, 25	17, 25
$f_{\rm NC}$[b]	0.29, 0.52	0.13, 0.28
Δ' (pc)	0.07	0.07
n (cm^{-3})	6.1×10^5	6.1×10^5
σ_v (km s^{-1})	0.6	0.6
$\langle B_t^2 \rangle / \langle B_0^2 \rangle$[b]	$\simeq 0.67, 0.68$	$\simeq 0.31, 0.37$
$\langle B \rangle_{pos}$ (mG)	$\simeq 0.7$	$\simeq 1.1$

[a] We used two fixed values of the parameter δ.

[b] The two values correspond to the results using the two fixed values of δ.

has been convolved by the SMA response (see Sec. 3.4.2), thus, the effect should be the same as in the observational data.

The first term on the right hand side in Eq. (3.3) contains the integrated turbulent magnetic field contribution, while the second (exponential) term represents the correlation by the combined effect of the beam (W) and the turbulent magnetic field (δ). The value of the correlated component at the origin $l = 0$, $f_{\rm NC}(0)$, allows us to estimate the turbulent to large-scale magnetic field strength ratio as

$$\frac{\langle B_t^2 \rangle}{\langle B_0^2 \rangle} = N \, f_{\rm NC}(0). \tag{3.5}$$

To fit the angular dispersion function to our results and to be able to perform a qualitative comparison between the observations and the numerical simulations, we used two fixed values of the parameter δ, 17 mpc (from Girart et al., 2013) and 25 mpc which produced a better fit (see Fig. 3.11). The derived value of the correlated component at the origin is $f_{\rm NC} \simeq 0.29, 0.52$ and $\simeq 0.13, 0.28$ for both values of δ and the observations and simulations respectively (see Table 3.4). A reasonable approximation to the core's effective thickness, Δ', is to assume that it is similar to the average diameter of the dense core measured on the plane of the sky with the SMA (Koch et al., 2010), which in our case is $\simeq 0.07$ pc (see Sec. 3.3.1). Using Eqs. (3.4) and (3.5) $\langle B_t^2 \rangle / \langle B_0^2 \rangle$ is $\simeq 0.7$ for the observations, i.e., it is close to equipartition between the turbulent and ordered magnetic field energies. This is similar to the results obtained towards the high-mass star-forming region DR21(OH) (Girart et al.,

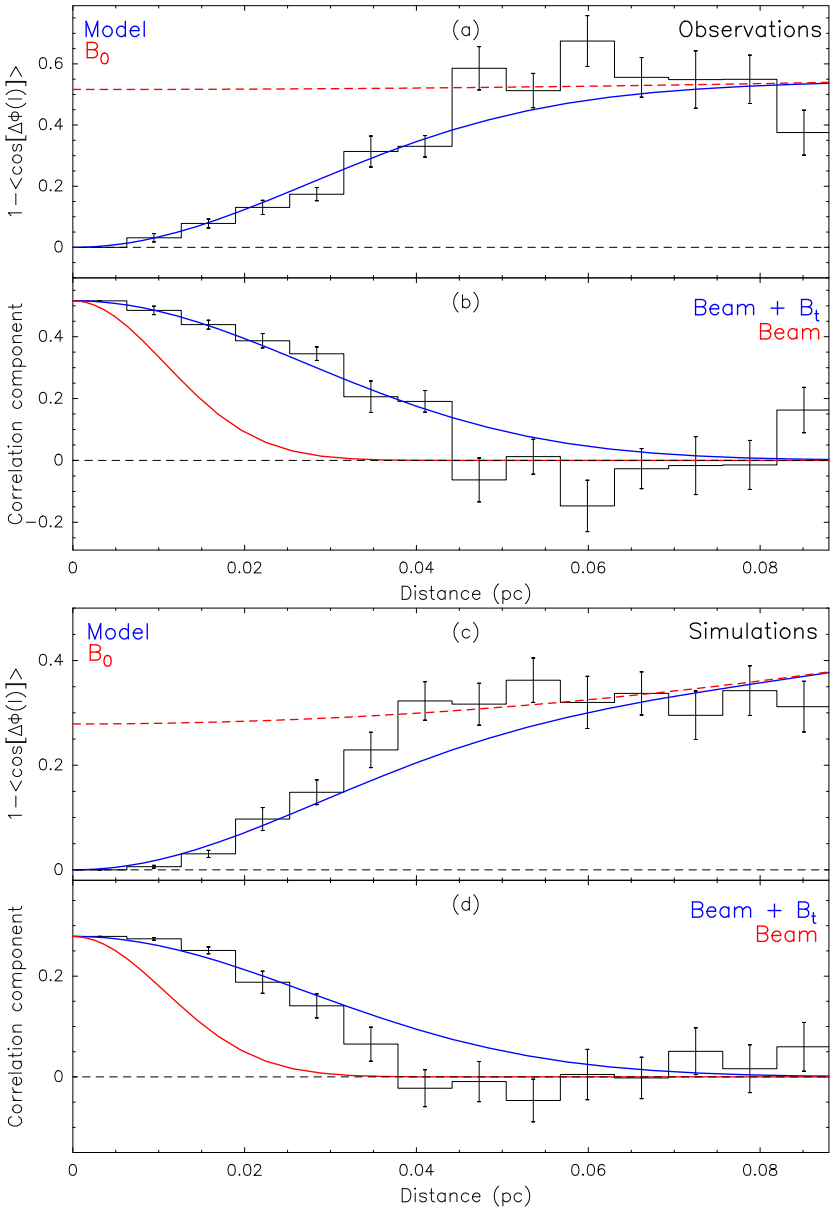

Fig. 3.11 *Panels (a) and (c)*: angular dispersion function comparison from NGC 6334 V observed and simulated magnetic field segments, using a Nyquist sampling. The solid black line and error bars are the mean and standard deviation of all the pairs contained in each bin. The red dashed line does not contain the correlated part of the function (i.e., $f_{\rm NC}(0)+a_2' \, l^2$). The blue line shows the fit to the data using Eq. (3.3) and fixed $\delta = 25$ mpc. *Panels (b) and (d)*: The solid black line represents the correlated component (exponential term of Eq. (3.3)) of the fit to the data. The solid red line shows the correlation due to the beam and the solid blue line shows the correlation due to the beam and the turbulent component of the magnetic field. Panels (a) and (b) show the results from the SMA observations. Panels (c) and (d) show the results from the numerical simulations.

2013). However, for the simulations the values are lower ($\simeq 0.3, 0.4$). One possibility for this difference is that the size of the core in the simulations could be larger than the observed one, as N is proportional to Δ'. Also, the thermal Q and U instrumental noise produced by the SMA can induce an increase of the angular dispersion which is not taken into account in the simulations (see upper panel of Fig. 3.11).

To estimate the large-scale magnetic field strength on the plane of the sky we used the CF equation, $\langle B_0^2 \rangle^{1/2} = \sqrt{4\pi\rho}\ \sigma_v\ [\langle B_t^2 \rangle / \langle B_0^2 \rangle]^{-1/2}$, (e.g., see Eq. (57) by Houde et al., 2009). Table 3.4 shows the values used for the velocity dispersion σ_v and the number density n (using a mean molecular weight of 2.33). To derive the averaged volume density we used the mass derived from the total 870 μm flux density detected with the SMA (~ 50 M$_\odot$) and the size of the core (~ 0.07 pc). We estimated the velocity dispersion from the $H^{13}CO^+$ (4–3) data, because it is well correlated with the 870 μm dust emission (see upper panel of Fig. 3.3). The derived value for the ordered large-scale magnetic field strength on the plane of the sky for both observations and simulations is $\langle B_0^2 \rangle^{1/2} \simeq 1$ mG. This value is in very good agreement with the average value of the magnetic field (weighted by density) measured in the simulation at 0.9 $t_{\rm ff}$, 0.9 mG.

3.5 Discussion

3.5.1 Simulation results and comparison with observations

In the bottom panel of Fig. 3.8 we present the results from the simulations filtered out with the SMA response. The map shows different velocity structures at scales of ~ 0.1 pc which seem to converge towards the strongest peak of the continuum and with a similar velocity range as the one present in the observed data. As in the case of the observations, in this Figure we notice that the field has three main orientations: segments that are almost horizontal, but that have two components: at +70 and +100 degrees, (also seen as a double peak in the histogram of the lower panel of Fig. 3.2). The third component is not highly populated, but it is clearly traced by the almost vertical white segments shown in Fig. 3.8. This component corresponds to the long tail towards small angles of the 70-degree component in the histogram shown in the lower panel of Fig. 3.2. Furthermore, note that at least the two main components, at +70 and +100 degrees, coincide with the two different velocity structures traced by $H^{13}CO^+$.

The magnetic field configuration shown in the lower panel of Fig. 3.8 can be understood in terms of the dynamics of the core. In Fig. 3.10 we show the gas column density (colors) and the $x-y$ velocity field of the gas (thin black arrows) after evolving the simulation. Note

that this representation has no observational counterpart, and although the simulation resolution is $\sim$ 200 au, the column density map shown in this Figure has been convolved with a beam of the same size of the observations. The column density map shows filamentary structures which seem to converge at the center of the box, where the highest column densities are found. The velocity field shows how the gas is converging from the dense structures at the large scale ($\sim$0.2 pc) towards the highest density region, at $\sim$0.02 pc scales, and they appear to be almost radial. Thus, it is clear that the core is collapsing. The originally horizontal magnetic field has been advected at this time by the collapsing gas, resulting in an hourglass shape with a dominant nearly horizontal component at the center of the core, with position angles of $+90 \pm 20$ degrees. This dominance is just the consequence of the B-field being compressed and dragged by the collapsing gas. We notice also that in the outer parts of the core, the B-field does have components that are far from parallel to the original magnetic field. Although it is a coincidence that the simulations exhibit three main orientations of the magnetic field, as in the observations, the important point here is that the B-field, in the innermost denser part of the core, seems to be oriented mostly horizontal, while in the outermost parts it looks more radial.

It can be asked whether the selected angle of view of the simulations affects what we observe in Fig. 3.8. Certainly, as the magnetic field is a vector quantity, any point of view could be considered as "particular". And we have chosen a point of view that is somehow special: it is perpendicular to the initial magnetic field (the box is seen along the z-axis, while the initial magnetic field runs along the x-axis). Given this configuration, and since the collapse occurs almost radially, one may assume that the density and magnetic field must have, in a statistical sense, an axial symmetry with respect to a declination offset=0 (Fig. 3.8). This means that, in principle, if we had observed the core along any other line of sight that was perpendicular to the x-axis, we would have observed something similar: nearly horizontal orientations of the field in the innermost parts of the core, and more radially directed orientations in the external parts of the core. However, if we were observing the simulation along the x-axis, the horizontal, dominant component of the B-field would almost not be observable. The B-field should look almost radial in the outskirts of the core, with a decreasing component at the center. The more general situation will be something in between these two possibilities, i.e., radial lines in the external parts of the core, and a less-dominant magnetic field in the center of the box.

As we do not include feedback processes in the numerical model, we cannot model the hot core itself (and the associated outflows). However, in the densest part of the simulation, where we locate the "Hot Core" labeled in Fig. 3.10, we have a group of three stars (sinks) with a total mass of ~ 9.7 $M_\odot$ in a compact space of 0.03 pc ($\sim 4.7''$, assuming a distance

of 1.3 kpc), which is comparable with the synthesized beam of our observations. It is remarkable that this mass is comparable with the mass inferred from kinematics arguments in the observed hot core (~ 6 $M_\odot$; see Sec. 3.3.2), which give us confidence that we are comparing our observations with an adequate model.

Finally, in addition to the good qualitative comparison of the velocity and magnetic field structures between the SMA observations and the numerical simulations, the angular dispersion function analysis also reveals a very similar behavior for both (see Sec. 3.4.3 and Fig. 3.11). The simulations, thus, again seem to be a good approximation to the observational results.

3.5.2 Outflow-generated cavity

We have seen in Sec. 3.3.1 that the emission from the extended dense core of NGC 6334 V (traced by $H^{13}CO^+$ (4–3) and CH_3OH 7(1,7)−6(1,6)) presents a clear ring-like structure around the systemic velocity, -5.7 km s^{-1} (see Fig. 3.3). The infrared and radio sources found in the region are located at the center of the ring, that also coincides with the cavity of the dust continuum emission. In addition, we detected high-velocity gas traced by the CO (3−2) molecular line at the position of the cavity and at the center of the ring structure (see Fig. 3.6). 4.5 μm emission is also detected crossing through the center of the ring with an east-west elongated shape presenting a bow shock structure towards the west, suggesting the emission could be shock- or outflow-generated (see Fig. 3.4). These results suggest the presence of an east-west outflow (also reported by Hashimoto et al., 2007; Simpson et al., 2009) that could be affecting the central region of NGC 6334 V, causing a cavity in both the extended dense gas as well as in the dust continuum structure.

3.5.3 Comparison with other NGC 6334 star-forming sites

In a previous work, Li et al. (2015) studied the magnetic field properties in several star-forming regions inside NGC 6334, from 100 down to 0.01 pc scales. Source V was not included in this study as large-scale polarization observations were not available. They concluded that the well ordered magnetic field (at all scales) in sources I, I(N) and IV plays a crucial role in the fragmentation of NGC 6334.

However, in NGC 6334 V, we see a more complex magnetic field morphology governed by the gas dynamics. It seems that NGC 6334 V, which is located at the southern end of the NGC 6334 ridge and possibly at the intersection region with another northwest-southeast gas filament, with gravity already being the dominant force over the magnetic field (e.g., André et al., 2016), may be more dynamically evolved than the sources I, I(N) and IV (note

that the total mass in NGC 6334 V seems to be smaller than in source I and I(N); Hunter et al., 2006).

3.6 Summary

We analyzed spectro-polarimetric observations at 345 GHz towards the intermediate/high-mass star-forming region NGC 6334 V. The main results are as follows:

- The dust continuum emission presents an arc-like structure of ∼0.07 pc (∼14,000 au), with three distinguishable peaks forming a cavity structure (Fig. 3.1). The total mass of the arc-like molecular structure is ~ 50 $M_\odot$. The main peak (HC) has a mass of $\sim$ 4–9 $M_\odot$ and exhibits the typical chemistry of a hot core with emission from ^{34}SO, SO_2, $^{34}SO_2$, CH_3OH, CH_3OCH_3, CH_3OCHO and HC_3N. Dense core tracers $H^{13}CO^+$ (4–3) and CH_3OH 7(1,7)−6(1,6) show extended emission forming a ring-like structure at the systemic velocity of -5.7 km s^{-1}. The presence of an outflow at the center of the region could be affecting the surrounding gas forming the cavity traced by the dust continuum and the dense gas emission from $H^{13}CO^+$ and CH_3OH.

- Kinematically, the dense core has two distinctive velocity components, one at -5.0 km s^{-1} tracing a filamentary-like arm on the southeast part of the core, and another one at -7.4 km s^{-1} arising mainly from the northern part (Figs. 3.5, 3.7). Both velocity structures converge towards the hot core. At higher density regions in the hot core, the hot core line tracers CH_3OCHO 31(0,31)−30(1,30) and several transitions of CH_3OH, CH_3OCH_3, $^{34}SO_2$ and SO_2 show the same two velocity components. The shock tracer SiO (8–7) (Fig. 3.7b,c) presents a velocity component just at an intermediate velocity (~ -6 km s^{-1}) suggesting interaction between the two flows.

- The magnetic field (derived from the dust thermal polarized emission at 870 μm) shows a bimodal converging pattern towards the hot core and follows the distribution of the two velocity components.

- We produced synthetic observations from numerical simulations of massive star-forming regions dominated by gravity. As in the SMA observations, the numerical simulations produced two distinctive velocity components (traced by ARTIST-generated $H^{13}CO^+$ emission) converging towards the strongest peak of the dust thermal emission, with the magnetic field being dragged by the gas. The polarization angular dispersion function comparison between the observations and simulations also reveals a very similar behavior.

- NGC 6334 V may be more dynamically evolved than the sources I, I(N) and IV (see Li et al., 2015), with gravity already being the dominant force over the magnetic field.

Finally, these results show how the gas is being accreted from the larger scale extended dense core ($\sim$ 0.1 pc) of NGC 6334 V towards the higher density hot core region at $\sim$ 0.02 pc scales, through two distinctive converging flows dragging along the magnetic field whose strength seems to have been overcome by gravity.

Chapter 4

Converging flows + rotation dynamics in L1287

4.1 General overview

L1287 is a dark cloud located at a distance of 929 pc (Rygl et al., 2010). Large-scale images at 160, 250, 350 and 500 μm from *Herschel*, tracing cold dust towards the region, show a $\sim$10 pc projected scale filamentary structure with L1287 located approximately at the center (see Fig. 4.1).

The densest core in L1287 harbors a binary FU-Orionis system, RNO1B/1C (Kenyon et al., 1993; Staude and Neckel, 1991), with its components separated by $6''$ ($\sim 5,000$ au) at P.A.$\sim 45^{\circ}$. FU-Orionis objects are young, pre-main-sequence stars which are observed to increase their brightness by 4–6 mag in the optical and remain bright for decades (Herbig, 1977). The large-amplitude flares are attributed to enhanced accretion from the surrounding circumstellar disk (Hartmann and Kenyon, 1985).

RNO1B/1C belong to a young, small stellar cluster. These young stellar objects (YSO) are detected in the near-IR and cm wavelengths (Anglada et al., 1994; Quanz et al., 2007, see Fig. 4.2). All infrared sources (except for two) have been classified as Class 0/I-II objects, including RNO1B/1C. One of the exceptions, IRAS 00338+6312, is still a very deeply embedded protostar (Quanz et al., 2007). The bolometric IR luminosity of IRAS 00338+6312 calculated from the fluxes of the four IRAS bands is ~ 600 $L_{\odot}$. Anglada et al. (1994) proposed that VLA 3 is associated with IRAS 00338+6312.

Earlier studies have found a bipolar outflow in the region in the northeast-southwest direction (Snell et al., 1990; Yang et al., 1991) and several sources have been proposed as the exciting source (e.g., RNO1B/1C by Staude & Neckel 1991, McMuldroch et al., 1995,

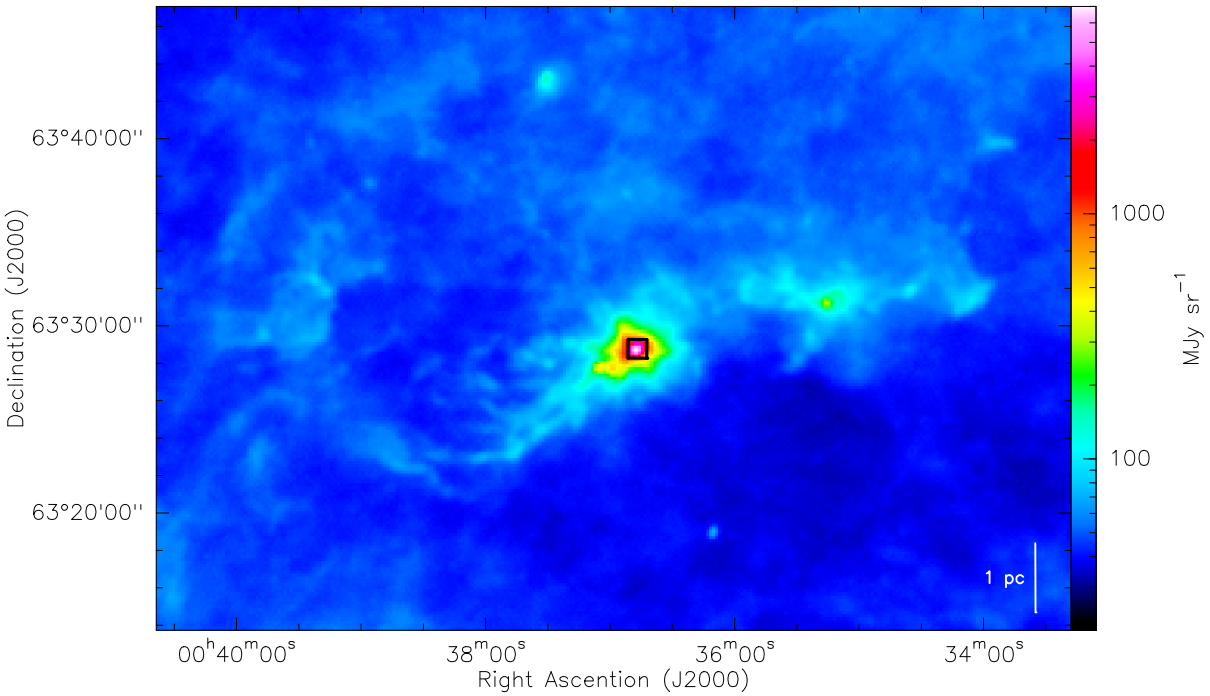

Fig. 4.1 350 μm *Herschel* image. At this band *Herschel* traces mainly the cold dust in the cloud. The black box indicates the field of view of the upper panel of Fig. 4.2, which presents the 1.3 mm continuum image taken with the SMA in extended, compact and sub-compact configurations.

VLA 3 by Anglada et al., 1994 or IRAS 0038+6312 by Yang et al., 1995, Quanz et al., 2007).

In this Chapter we study the gas structure and kinematics of L1287. The analysis will be compared to the higher-mass case of NGC 6334 V to be able to discuss whether the converging flow scenario found in NGC 6334 V also applies to L1287.

In Sec. 4.2 we present the details of our observations. The observational results from the dust continuum and molecular line emission are shown in Sec. 4.3. In Sec. 4.4 we present the analysis of the kinematics and a possible definite identification of the powering source of the previously reported outflow. Also, we compare the obtained results with the previous work done towards NGC 6334 V. A summary of the main results is presented in Sec. 4.5.

4.2 Observations and data reduction

4.2.1 Submillimeter Array (SMA)

L1287 region was observed with the Submillimeter Array (SMA) (Ho et al., 2004) in five tracks between August 2013 and July 2014 in three different configurations, subcompact, compact and extended. A summary of the observations are listed in Table 4.1. Baselines range from $\sim$4 kλ to $\sim$140 kλ. The phase and pointing center of the observations is RA(J2000)= $00^{h}36^{m}46.65^{s}$, Dec(J2000)= $+63°28'57.90''$. The observations were obtained with the 230 GHz receiver with 4 GHz bandwidth per sideband. The correlator consisted of 48 chunks with a bandwidth of 104 MHz each. The frequency was centered at 231.3 GHz at the chunk 35 of the upper sideband (USB). This configured the correlator with the lower sideband (LSB) covering from 216.48 GHz to 220.46 GHz and the USB from 228.46 GHz to 232.43 GHz. These frequency ranges include the following molecular lines: CO (2–1), ^{13}CO (2–1), SO (6(5)–5(4)), SiO (5–4), C^{18}O (2–1), N_2D^+ (3–2) and NH_2D (3(2,2)–3(1,2)). ^{13}CO and N_2D^+ were observed with 512 channels and a spectral resolution of 0.26 km s^{-1}, NH_2D was observed with 256 channels giving 0.53 km s^{-1} spectral resolution. The rest of the lines were observed with 128 channels and a 1.06 km s^{-1} spectral resolution. To generate the 1.3 mm continuum, we averaged the line-free channels in the lower and upper sidebands.

The weather conditions in all the observing dates were moderately good. The system temperature T_{sys} for all the observations was around 150 K. The calibration for absolute flux, passband, and gain were carried out using the MIR IDL software package (Scoville et al., 1993) and the images were created using the Multichannel Image Reconstruction, Image Analysis, and Display (MIRIAD, Sault et al., 1995) software package (see Table 4.1 for calibrators). We used ROBUST 0 (Briggs, 1995) and a two step cleaning process with cleaning boxes to create the 1.3 mm dust continuum emission map with only the extended configuration. To check the fidelity of the boxes chosen we created extended+compact configurations maps for different "uvranges" noticing the most compact emission remaining in the map with only the longest baselines. We used cleaning boxes only at the structures continuously present in all the maps. The synthesized beam for the extended configuration map is $0.96'' \times 0.79''$, P.A.$= -22°$, and the root-mean square (RMS) noise level is 0.5 mJy beam^{-1}. Also, we used the three configurations to create the dust continuum emission map to obtain the more extended structure. We used ROBUST 1 and the same two step cleaning process as before, this time with one central box around the emission. The synthesized beam is $2.28'' \times 2.17''$, P.A. $= -19°$. The molecular line maps were also generated using the three configurations, except for OCS (18–17), HNCO 10(0,10)–9(0,9) and CH_3OH 3($-$2,2)–

Table 4.1 SMA observations summary.

Array configuration	subcompact	compact	extended
Observing date	2014 Feb 10, July 25	2013 Aug 2	2013 Oct 24, 25
$\tau_{225\mathrm{GHz}}$	0.14, 0.12	0.13	0.25, 0.16
Number of antennas	6, 7	5	6
Time on target (hours)	2, 5	8	8
Flux calibrator	Callisto, Neptune	Uranus	Uranus
Passband calibrator	0102+584	3c84	3c454.3
Gain calibrator	0102+584	0102+584	0102+584

4(−1,4) which present very compact emission and were generated using only extended and compact configurations. We used a ROBUST parameter of 2 (natural weighting), which provides the best sensitivity, for all the molecular lines except for the CO (2–1) line where we used a ROBUST parameter of 0 to obtain a better angular resolution.

4.2.2 Very Large Array (VLA)

As additional information for the discussion of the SMA results, we show observations of the $(J,K) = (1,1)$ and $(J,K) = (2,2)$ inversion transitions of the ammonia molecule (at the rest frequencies 23.694495 and 23.722633 GHz, respectively) from Sepúlveda et al. in prep. These observations were carried out with the VLA of the NRAO[1] in the D configuration in August 1996. The synthesized beam is $3.69'' \times 3.29''$, P.A. = 1.56°, and the rms noise level is 3 mJy beam^{-1}.

4.3 Results

4.3.1 Dust continuum

Figure 4.2 shows the 1.3 mm continuum image taken with the SMA. The continuum emission at 1.3 mm can arise from dust thermal emission and free-free continuum emission. Based on the deep VLA observations of the centimeter free-free continuum emission presented in Anglada et al. (1994), we constrained the 1.3 mm free-free emission to be $<$ 0.5 mJy towards IRAS 0038+6312 and RNO1C sources, which is negligible as compared to the detected emission level in Fig. 4.2 (see Table 4.2).

[1]The National Radio Astronomy Observatory is a facility of the National Science Foundation, operated under cooperative agreement by the Associated Universities, Inc

The 1.3 mm dust continuum emission shows six main cores (with at least a 35σ closed contour) separated by a mean distance of ~ 0.03 pc ($\sim 6,500$ au) and with a mean size of ~ 0.02 pc ($\sim 4,500$ au). We estimated the gas+dust mass of each core following

$$M = R\frac{d^2 S_\nu}{B_\nu(T_d)\kappa_\nu}, \tag{4.1}$$

where d is the distance, S_ν is the flux density, $B_\nu(T_d)$ is the Plank function at the isothermal dust temperature T_d, κ_ν is the dust opacity and the factor R is the gas-to-dust mass ratio. We assumed the gas-to-dust ratio to be 100 and $T_d = 20$ K (the average temperature in starless cores, e.g., Sánchez-Monge et al., 2013) and adopted $\kappa_\nu = 0.899$ cm^{2}g^{-1} for thin ice mantles after 10^5 years of coagulation at a gas density of 10^6 cm^{-3} and for the frequency of our observations (Ossenkopf and Henning, 1994). The masses range between ~ 0.4 and ~ 4 M$_\odot$, with the central core (associated to RNO1C and VLA 1) and the northeast core (associated to IRAS 0038+6312 and VLA 3) being the most massive ones, with ~ 4 and ~ 2 M$_\odot$, respectively. The faintest core, towards the southeast of the central core, seems to be associated to VLA 4 and has a mass of ~ 0.4 M$_\odot$. The faint and small core located towards the south of the central core seems to be associated to FU-Orionis candidate RNO1B and has a mass of ~ 0.6 M$_\odot$. The total mass of the region is 25 M$_\odot$.

To better resolve the internal fragmentation in the region, we present the 1.3 mm continuum image generated using only the extended configuration data. The lower panel of Fig. 4.2 presents the higher-resolution image. The emission shows a very fragmented structure forming a ~ 0.02 pc scale clumpy toroid, and two ~ 0.04 pc scale spiral arms to the north and south. The previous central core has been divided in eight different condensations or fragments, two of them very close to RNO1C and VLA 1 sources. The core associated to IRAS 0038+6312 and VLA3 does not seem to present further fragmentation, while the core associated to RNO1B has fragmented into two condensations.

In total, we identify 14 fragments with at least a 7σ closed contour, they are labeled MM1 to MM14 in order of increasing right ascension. To estimate the gas+dust mass for each individual fragment we measured the flux density of each fragment by fitting an elliptical gaussian using the MIRIAD task IMFIT. The polygons for fitting the gaussians were drawn following the 6σ and the 9σ contour levels for the most extended sources ($1\sigma = 0.5$ mJy beam^{-1}). The properties derived from these fits also included the peak position, the deconvolved angular size and position angle and the intensity of the peak. The results are listed in Table 4.2.

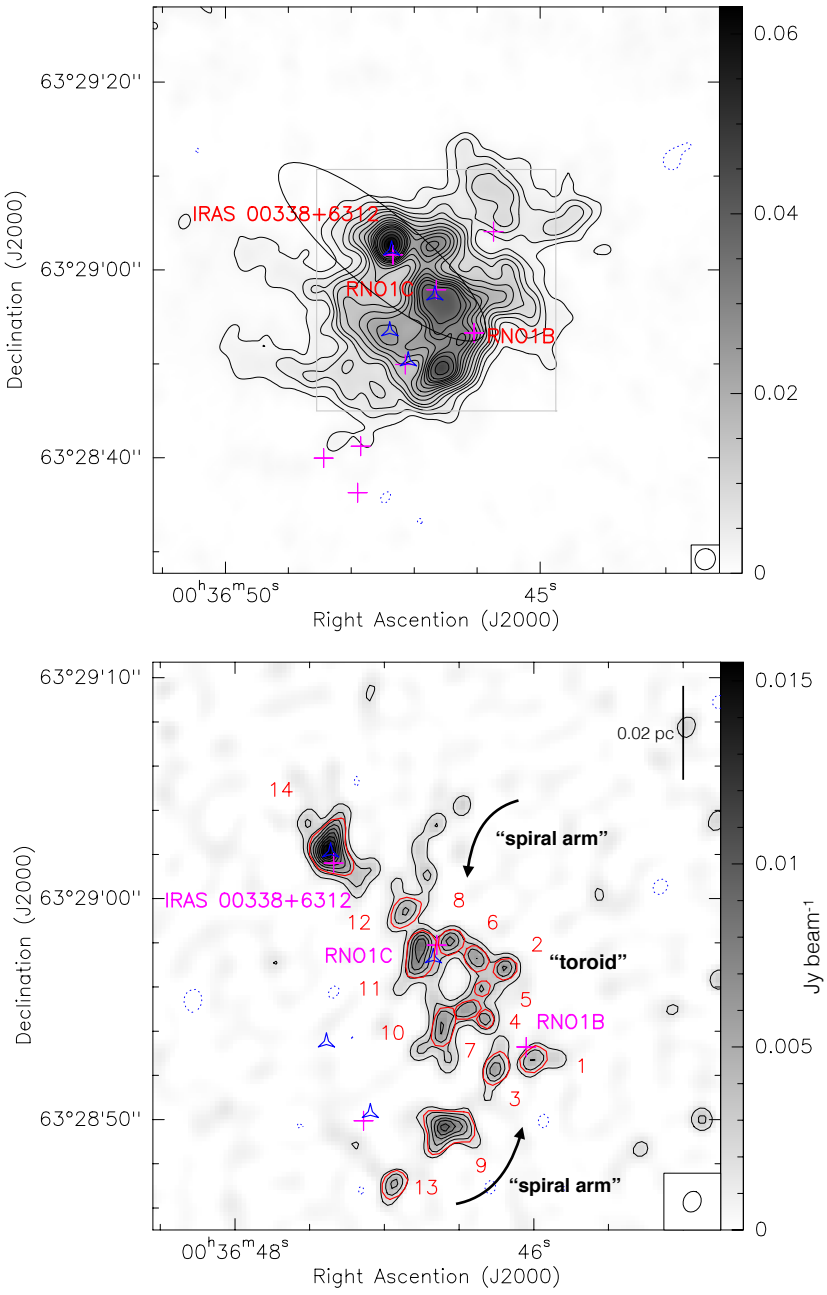

Fig. 4.2 *Upper panel*: 1.3 mm dust continuum emission with extended, compact and sub-compact configurations. Contours are -6, -3, 3, 6, ..., 15, 20, 25, 30, ..., 55, 65, 75, ..., 95 times the rms level of the map, 0.6 mJy beam^{-1}. Black ellipse corresponds to the position error ellipse for IRAS 00338+6312. The synthesized beam located at bottom right is $2.28'' \times 2.17''$, P.A. $= -19°$. Gray square corresponds to lower panel's field of view. *Lower panel*: 1.3 mm dust continuum emission with extended configuration. Contours are -3, 3, 6, 9, 12, ..., 30 times the rms level of the map, 0.5 mJy beam^{-1}. Sources are defined having at least a 7σ closed contour. Red polygons are drawn following the 6σ and 9σ contour levels for the most extended sources. Blue triangles and pink crosses in both panels are radio (Anglada et al., 1994) and infrared (Quanz et al., 2007) sources respectively. A scale bar is located at the upper right corner. The synthesized beam located at bottom right is $0.96'' \times 0.79''$, P.A. $= -22°$.

Table 4.2 Parameters of the sources detected with the SMA at 1.3 mm dust continuum emission.

Source	Position[a]		Deconv.ang.size[a]	P.A.[a]	$I_\nu^{\rm peak}$ [a]	S_ν [b]	Mass[c]	Association[d]
	α(J2000)	δ(J2000)	($''\times''$)	($^\circ$)	(mJy beam^{-1})	(mJy)	($M_\odot$)	
MM1-RNO1B	00:36:46.000	63:28:52.704	$1.1\pm0.3\times0.5\pm0.2$	-64 ± 17	4.50 ± 0.42	8.3 ± 1.7	0.16	IR
MM2	00:36:46.198	63:28:56.829	$0.6\pm0.1\times0.5\pm0.1$	-77 ± 29	6.24 ± 0.35	8.6 ± 1.8	0.16	–
MM3	00:36:46.255	63:28:52.307	$0.9\pm0.2\times0.1\pm0.1$	-16 ± 8	5.63 ± 0.46	7.6 ± 1.6	0.14	–
MM4	00:36:46.330	63:28:54.583	point source	–	5.41 ± 0.39	7.3 ± 1.5	0.14	–
MM5	00:36:46.348	63:28:55.930	$1.0\pm0.3\times0.6\pm0.1$	-25 ± 11	4.74 ± 0.10	8.6 ± 1.8	0.16	–
MM6	00:36:46.387	63:28:57.326	point source	–	5.93 ± 0.24	11.0 ± 2.2	0.21	–
MM7	00:36:46.450	63:28:54.966	$1.5\pm0.3\times0.4\pm0.2$	-70 ± 10	5.72 ± 0.36	13.0 ± 2.7	0.25	–
MM8	00:36:46.562	63:28:58.040	$0.9\pm0.3\times0.6\pm0.2$	-69 ± 31	6.45 ± 0.66	11.1 ± 2.3	0.21	–
MM9	00:36:46.584	63:28:49.613	$1.5\pm0.3\times0.9\pm0.2$	-82 ± 22	8.50 ± 0.11	25.7 ± 5.2	0.48	–
MM10	00:36:46.606	63:28:54.248	$2.0\pm0.6\times0.6\pm0.2$	-13 ± 8	6.22 ± 0.58	18.4 ± 3.8	0.35	–
MM11-RNO1C	00:36:46.761	63:28:57.583	$1.9\pm0.4\times0.6\pm0.1$	-9 ± 6	8.72 ± 0.85	24.7 ± 5.0	0.47	CM/IR
MM12	00:36:46.860	63:28:59.414	$1.2\pm0.2\times0.6\pm0.1$	-44 ± 8	4.71 ± 0.28	9.2 ± 1.9	0.17	–
MM13	00:36:46.936	63:28:47.078	$0.7\pm0.1\times0.2\pm0.1$	-28 ± 8	4.96 ± 0.24	6.5 ± 1.3	0.12	–
MM14-IRAS	00:36:47.366	63:29:02.237	$1.6\pm0.3\times0.9\pm0.2$	8 ± 15	13.84 ± 1.72	41.4 ± 8.3	0.78	CM/IR

[a] Position, deconvolved size, position angle (P.A.), peak intensity, flux density and the respective uncertainties derived from fitting a 2D Gaussian to each source using IMFIT task from MIRIAD. Using data only from the extended configuration.

[b] Error in flux density has been calculated as $\sqrt{(\sigma\,\theta_{\rm source}/\theta_{\rm beam})^2+(\sigma_{\rm flux-scale})^2}$ (Beltrán et al., 2001; Palau et al., 2013), where σ is the rms of the map, $\theta_{\rm source}$ and $\theta_{\rm beam}$ are the size of the source and the beam, respectively, and $\sigma_{\rm flux-scale}$ is the error in the flux scale, which takes into account the uncertainty on the calibration applied to the flux density of the source ($S_\nu\times\%_{\rm uncertainty}$) which we assumed to be 20%.

[c] Masses derived assuming a dust temperature of 20 K, and a dust (+gas) mass opacity coefficient at 1.3 mm of 0.899 cm^2 g^{-1} (for thin ice mantles after 10^5 years of coagulation at a gas density of 10^6 cm^{-3}, Ossenkopf and Henning, 1994). The uncertainty in the masses due to the opacity law and temperature is estimated to be a factor of 4.

[d] Association with signposts of stellar activity: IR = infrared source; CM = Centimeter radio source.

4.3.2 Molecular lines

In addition to the dust continuum emission, the SMA detected many molecular lines in the 8 GHz bandwidth. We identified 15 molecular lines including hot-core tracer methanol (CH_3OH) and shock tracers SO, OCS and SiO. We also detected formaldehyde (H_2CO) in several transitions and HNCO. Two deuterated molecules DCN and DNC and outflow tracer CO are also present. Table 4.3 lists the frequency, the energy of the upper level and the estimated critical density for each transition.

The molecular line emission presents a complicated structure. In Fig. 4.3 we present the velocity integrated emission (i.e., moment 0) maps of several characteristic lines. Shock tracer SiO (5–4) presents compact emission towards IRAS 00338+6312, RNO1C, VLA 4 and the dust continuum core towards the south and situated close to VLA 2. Also, it presents compact emission, not associated to dust continuum emission nor to any YSO, towards the east, west and southwestern parts of the region. Shock tracer SO 6(5)–5(4) presents similar structure, with strong emission towards IRAS 00338+6312 and RNO1C but with more extended emission covering the central part of the region. Also, the southwestern emission is more extended than the SiO emission forming a "V" structure. CH_3OH 8(−1,8)–7(0,7) and formaldehyde (H_2CO) transitions present similar emission to SiO and SO, but showing some emission towards VLA 2 and fainter emission towards RNO1C. DCN (3–2) and H_2CO 3(2,1)–2(2,0) transitions trace well the dust continuum emission. The emission extends over the dust continuum presenting the strongest emission at the IRAS source. In addition, DCN (3–2) presents strong emission towards the dust toroidal structure, with fainter emission coinciding with RNO1C and the center of the dust continuum toroid. Furthermore, unresolved emission of CH_3OH 5(1,4)–4(2,2), CH_3OH 3(−2,2)–4(−1,4), OCS (18–17) and HNCO 10(0,10)–9(0,9) is detected at the IRAS source.

In Fig. 4.4 we present the intensity-weighted averaged velocity (i.e., moment 1) maps of the same lines. A Gaussian fit to the averaged spectrum of the entire emission of the dense core tracer DCN (3–2) suggests that the systemic velocity of L1287 is -17.4 km s^{-1}. Dense core tracers H_2CO, SO 6(5)–5(4) and more clearly DCN (3–2) show a northwest-southeast large scale (~ 0.1 pc) velocity gradient between -15 and -19 km s^{-1} centered at the dust central core near RNO1C and VLA 1. These tracers also present a more compact reversed velocity gradient at the IRAS 00338+6312 source position, in a perpendicular orientation with respect to the northeast-southwest bipolar outflow previously reported (Snell et al., 1990; Yang et al., 1991). The velocity gradient at the IRAS source position is also seen in CH_3OH 8(−1,8)–7(0,7). The emission towards the southwest of the dust continuum emission seen in H_2CO, SO and SiO is clearly blue-shifted with a velocity of ~ -24 km s^{-1}.

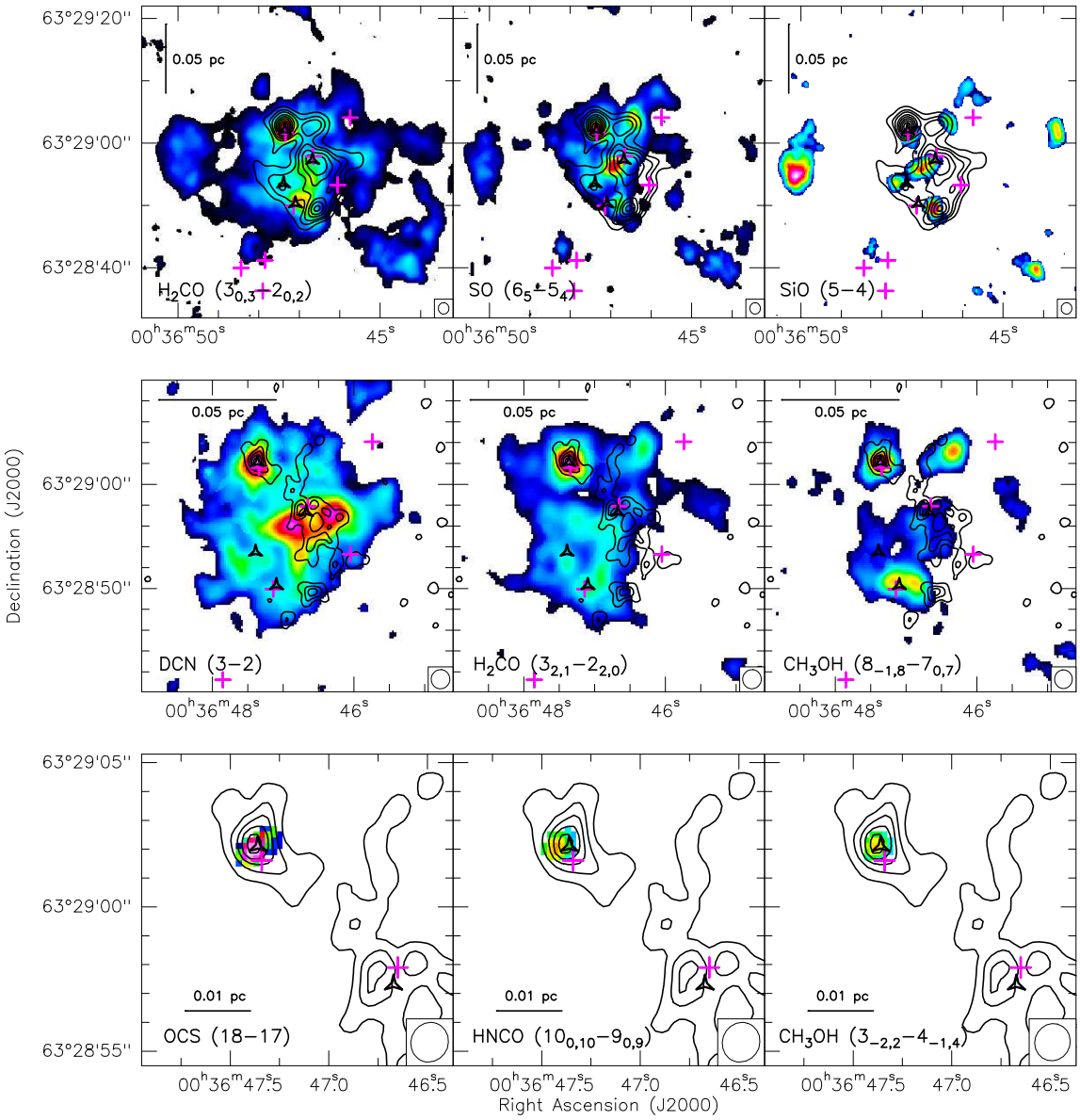

Fig. 4.3 Color scale image of the integrated intensity (i.e., moment 0) maps of selected molecular line tracers overlapped with the contour map of the 1.3 mm dust continuum emission (only using the extended configuration for the dust continuum emission in the middle and lower panels). Pink crosses and black triangles indicate infrared (Quanz et al., 2007) and radio (Anglada et al., 1994) sources, respectively. The synthesized beam of each molecule is located at the bottom right corner.

Table 4.3 Molecular lines.

Molecule	Transition	Frequency (GHz)	E_U (K)	ρ^{a}_{crit} (cm^{-3})
CH_3OH	5(1,4)–4(2,2)	216.946	56	2.33×10^{6}
SiO	(5–4)	217.105	31	3.25×10^{8}
DCN	(3–2)	217.239	21	–
H_2CO	3(0,3)–2(0,2)	218.222	21	2.56×10^{6}
H_2CO	3(2,2)–2(2,1)	218.476	68	2.96×10^{6}
H_2CO	3(2,1)–2(2,0)	218.760	68	3.36×10^{6}
OCS	(18–17)	218.903	100	4.28×10^{5}
$C^{18}O$	(2–1)	219.560	16	9.33×10^{3}
HNCO	10(0,10)–9(0,9)	219.798	58	–
SO	6(5)–5(4)	219.949	35	–
^{13}CO	(2–1)	220.399	16	9.38×10^{3}
DNC	(3–2)	228.910	22	–
CH_3OH	8(−1,8)–7(0,7)	229.759	89	2.62×10^{7}
CH_3OH	3(−2,2)–4(−1,4)	230.027	40	7.05×10^{6}
CO	(2–1)	230.538	17	1.07×10^{4}

[a] $\rho_{crit}=A_{ul}/\gamma$, where A_{ul} is the Einstein spontaneous emission coefficient and $\gamma=\sigma\ <v>$ is the collisional rate where σ is the cross section of the collision for each transition and $<v>\approx(3kT/m)^{1/2}$ is the average velocity of the collisional particles. As H_2 is the most abundant molecule it is used as the dominant collisional particle. We assume T=20 K. The Einstein spontaneous emission coefficients are taken from the Leiden Atomic and Molecular Database (LAMDA[b]) and splatalogue.net databases and γ values are taken from LAMDA database.

[b] http://home.strw.leidenuniv.nl/∼moldata/

To study in more detail the kinematics in the region, we present the blue- and red-shifted emission of DCN (3–2) in Fig. 4.5. The first panel shows the emission at ±1.2 km s^{-1} from the systemic velocity. The blue- and red-shifted emission shows two structures forming the large-scale and reversed small-scale velocity gradients. At higher velocities (at ±2.4 and ±3.6 km s^{-1}), the small-scale velocity gradient at IRAS 00338+6312 becomes more compact. In Fig. 4.6, we present the blue- and red-shifted integrated map, from -20.0 to -18.8 km s^{-1} and -16.4 to -15.2 km s^{-1}, showing the two low-velocity structures separated by ~ 3 km s^{-1} which seem to converge at the IRAS 00338+6312 source position.

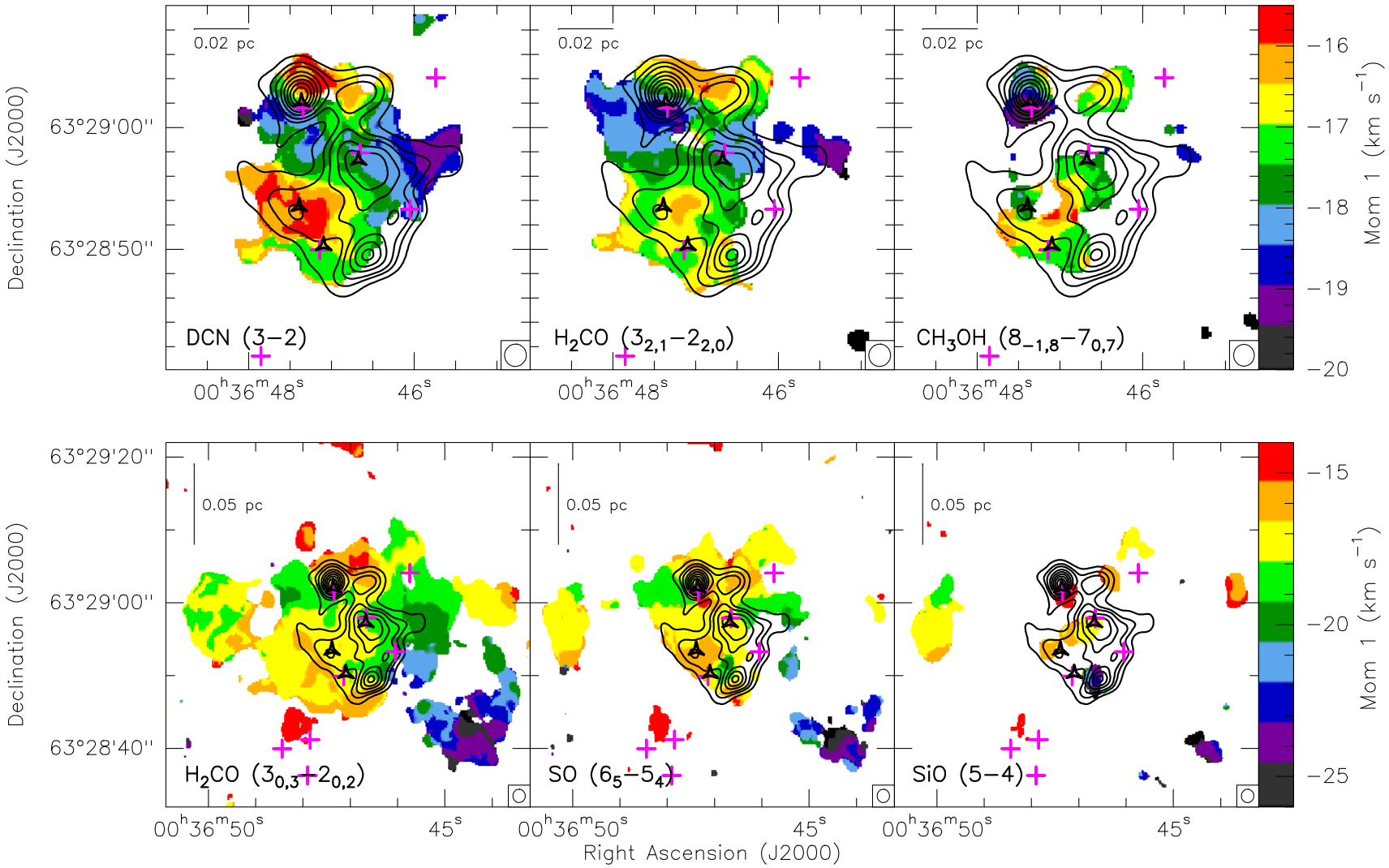

Fig. 4.4 Color scale image of the intensity-weighted averaged velocity (i.e., moment 1) maps of selected molecular line tracers overlapped with the contour map of the 1.3 mm dust continuum emission. Pink crosses and black triangles indicate infrared (Quanz et al., 2007) and radio (Anglada et al., 1994) sources, respectively. The synthesized beam of each molecule is located at the bottom right corner.

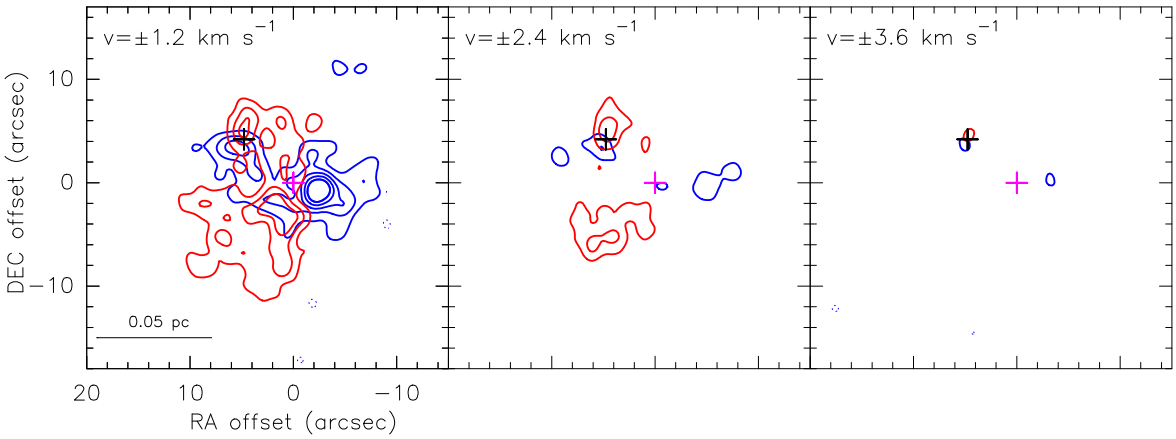

Fig. 4.5 Each panel shows the blue- and red-shifted emission of DCN (3–2) at ±1.2, ±2.4 and ±3.6 kms^{-1} from the systemic velocity −17.4 km s^{-1}. Contours are −4, 4, 8, 12, ..., 20, 30, 40, 50 times the rms noise level of the map, 0.03 Jy beam^{-1}. Black and pink crosses are IRAS 0038+6312 and RNO1C sources, respectively. The synthesized beam located at the bottom right corner of the first panel is 1.85″ × 1.77″, P.A. = −6°.

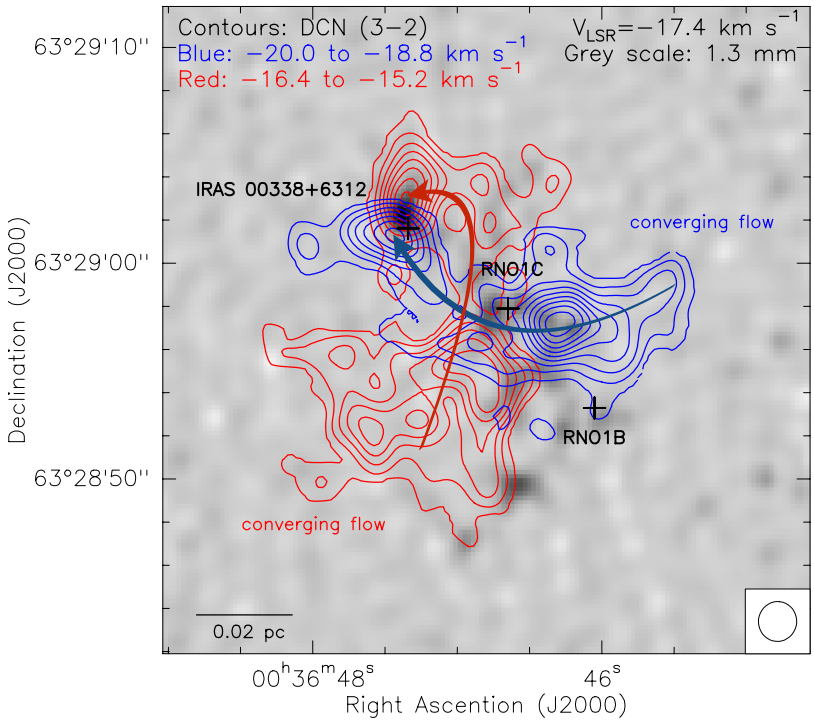

Fig. 4.6 *Contours*: averaged emission from blue- and red-shifted channels of DCN (3–2) displaying the two low-velocity flow components. Contours are 6, 9, 12, 15, ..., 30 times the rms noise level of the map, 0.03 Jy beam^{-1}. The synthesized beam is located at the bottom right corner. *Gray scale*: 1.3 mm dust continuum emission. Arrows indicate the two converging flows. Black crosses indicate the position of infrared sources IRAS 00338+6312 and FU-Orionis RNO1B and RNO1C (Quanz et al., 2007).

Molecular outflow

In Fig. 4.7 we display the red- and blue-shifted high-velocity emission of the CO (2–1) at $\pm$12, $\pm$16, $\pm$20 and $\pm$24 km s^{-1} from the systemic velocity $-$17.4 km s^{-1}. At these high velocities, the CO (2$-$1) traces molecular outflows. In agreement with the previous observations by Snell et al. (1990) and Yang et al. (1991), the emission shows an extended northeast-southwest bipolar molecular outflow centered near IRAS 0038+6312 (and VLA3) and FU-Orionis candidate RNO1C, however, IRAS 0038+6312 seems to be better centered. In the second panel (at $\pm$16 km s^{-1}), the center of the bipolar structure is also seen clearly towards the IRAS source. Furthermore, the red- and blue-shifted emission in the northeast and southwest lobes respectively, present clear cavity features, with the southern side of the blue-shifted lobe coinciding with the emission detected with the dense gas tracer H_2CO and the shock tracers SO and SiO. This strongly suggests the outflow is dragging dense gas from the region (see Figs. 4.4 and 4.8). In the last two panels, at the highest velocities, the blue-shifted emission appears at the position of RNO1C with an elongated structure in the north-south direction.

To analyze only the highest-velocity gas from the CO (2–1) emission, Fig. 4.9 shows the integrated emission between $-$51 and $-$47 km s^{-1}. The emission at these velocities is compact and appears only very close to the position of RNO1C. It is also good to notice that shock tracer SiO (5–4) shows emission towards both IRAS 0038+6312 and RNO1C (see Fig. 4.3).

4.4 Analysis and discussion

4.4.1 Converging flows + rotation dynamics

In Sec. 4.3.2 and Figs. 4.5 and 4.6 we have seen that the molecular dense gas traced by DCN (3–2) presents two velocity structures forming two distinguishable velocity gradients. A large scale one centered towards the central core of the dust continuum and a more compact one with a reversed orientation towards the IRAS 00338+6312 source. It is good to mention that the large-scale velocity gradient is also consistent with the even larger-scale dense gas traced with NH_3 observations (Sepúlveda et al. in prep).

In Fig. 4.10 we present position-velocity diagrams of the DCN (3–2) emission along both velocity gradients. The emission at the IRAS 0038+6312 source shows two velocity components at $-$18.6 and $-$16.3 km s^{-1} and a Keplerian-like velocity distribution, with the highest velocities close to the center position of the source and the lower velocities as you go farther from the center. The emission from the larger-scale velocity gradient shows the same

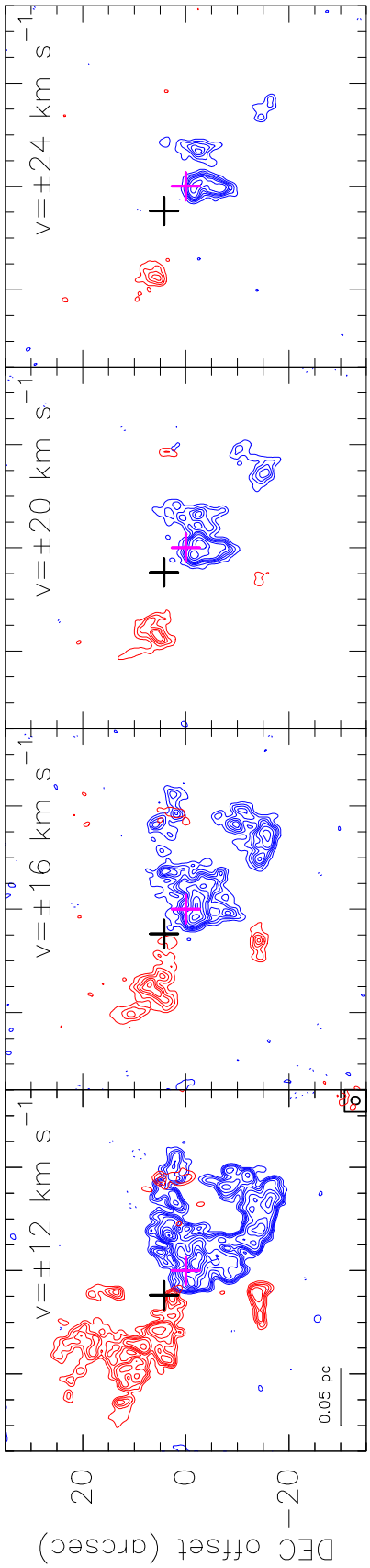

Fig. 4.7 CO (2–1) high-velocity emission. Each panel shows the red- and blue-shifted emission at ± 12, ± 16, ± 20 and ± 24 km s^{-1} from the systemic velocity -17.4 km s^{-1}. Contour levels are: $-6, 6, 9, ..., 15, 20, 30, 40, ...,$ 70 and $-3, 3, 6, 9, ..., 15, 20, 30, 40, 50$ times the rms level 0.04 Jy beam^{-1} for the first and the rest of the panels, respectively. Black and pink crosses are IRAS 0038+6312 (also VLA3) and RNO1C sources, respectively. The synthesized beam, located at bottom right of the first panel, is $1.66'' \times 1.38''$, P.A. $= -8°$. A scale bar is located at the bottom left corner.

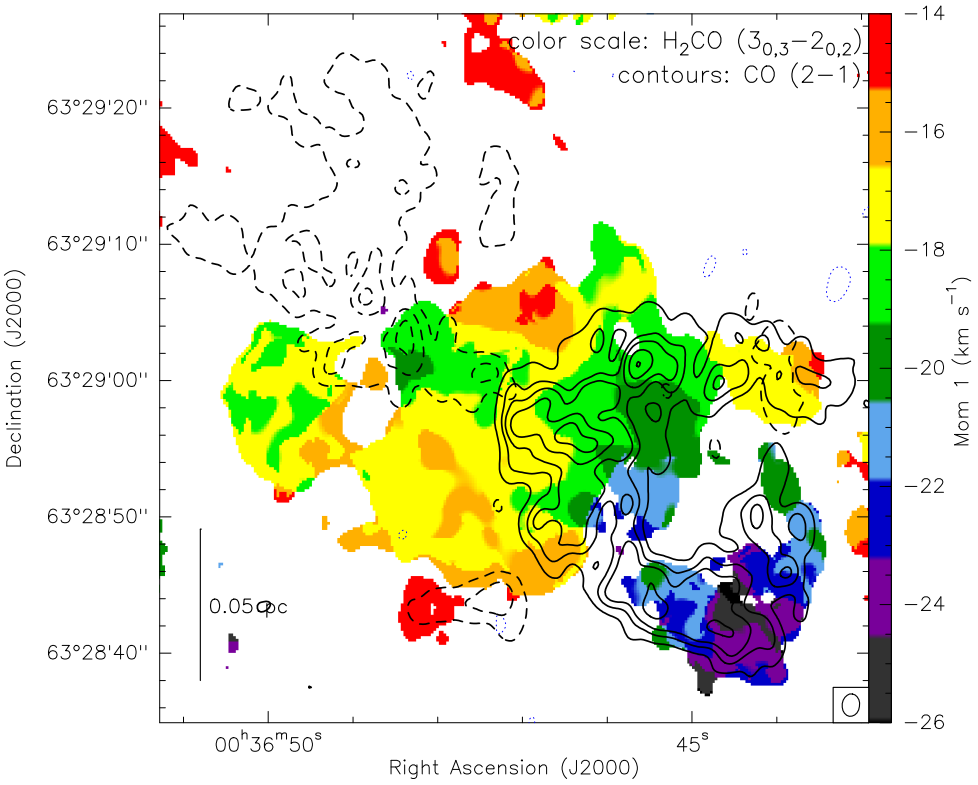

Fig. 4.8 *Contours*: CO (2–1) red- (dashed) and blue-shifted emission (solid) at ± 12 km s^{-1} from the systemic velocity -17.4 km s^{-1}. Contour levels are: -6, 6, 18, 30, 50, 70 times the rms level 0.04 Jy beam^{-1}. The synthesized beam located at the bottom right corner is $1.66'' \times 1.38''$, P.A. $= -8°$. *Color scale*: intensity-weighted averaged velocity (i.e., moment 1) map of H_2CO 3(0,3)–2(0,2) emission. A scale bar is located at the bottom left corner.

two velocity components centered at -18.6 and -16.3 km s^{-1} but without a Keplerian-like velocity distribution.

From the IRAS 0038+6312 velocity gradient, assuming Keplerian motion ($v = \sqrt{GM/R}$, where v is the velocity, G is the gravitational constant, M is the mass and R is the radius) and using a radius of $2.5''$ and $v = 1.25$ km s^{-1}, we estimated a mass for IRAS 0038+6312 of 4 $M_\odot$. The mass obtained is within the uncertainty of the lower-limit mass (considering that we are filtering extended emission with the SMA) obtained from the dust continuum emission (see Sec. 4.3.1 and Table 4.2).

On the other hand, to check if the gas associated to the larger-scale velocity gradient is gravitationally bound, we estimated the needed minimum mass. Given that the maximum velocity for an object accelerated in a gravitationally bound system is $v_{\rm max} = (2GM/R)^{1/2}$, we obtained a mass for the entire region of ~ 25 $M_\odot$, using a radius of $12''$ and a velocity of 2 km s^{-1}. The estimated mass is again within the uncertainty of the lower-limit mass obtained from the dust continuum emission of the entire region (see Sec. 4.3.1).

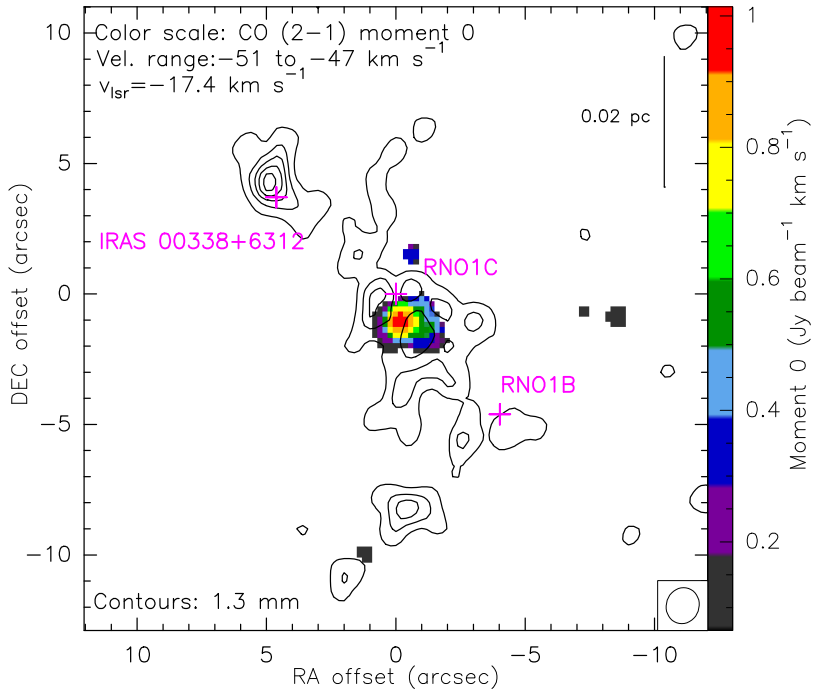

Fig. 4.9 CO (2–1) highest-velocity emission. *Color scale*: Moment 0 (i.e., integrated intensity) map. Velocity range from -51 to -47 km s^{-1}. The synthesized beam located at the bottom right corner is $1.39'' \times 1.27''$, P.A. $= -19°$. *Contours*: 1.3 mm dust continuum emission. Pink crosses are infrared sources (Quanz et al., 2007).

As the gas in the region seems to be gravitationally bound, one possibility for the observed kinematics is that both large-scale and small-scale velocity gradients belong to separate dynamics. The larger-scale velocity gradient could be associated to the central and southern dust continuum cores and to the more evolved infrared and radio sources found in the region (Quanz et al., 2007). Thus, the large-scale velocity gradient would be related to the past formation of these objects. On the other hand, the reversed smaller-scale velocity gradient could be associated to different kinematics taking place separately at the younger object IRAS 0038+6312.

Another explanation for both observed velocity gradients can be a single scenario of converging flows+rotation towards the compact high-density region (if we take into account the viewing angle projection; see Fig. 4.11). The two large-scale converging flows, traced by the large-scale velocity gradient, could be merging towards the compact IRAS source where the rotational motions seem to dominate the kinematics. Figures 4.5 and 4.6 seem to support this scenario, as it seems clear that both velocity gradients have connecting velocity structures.

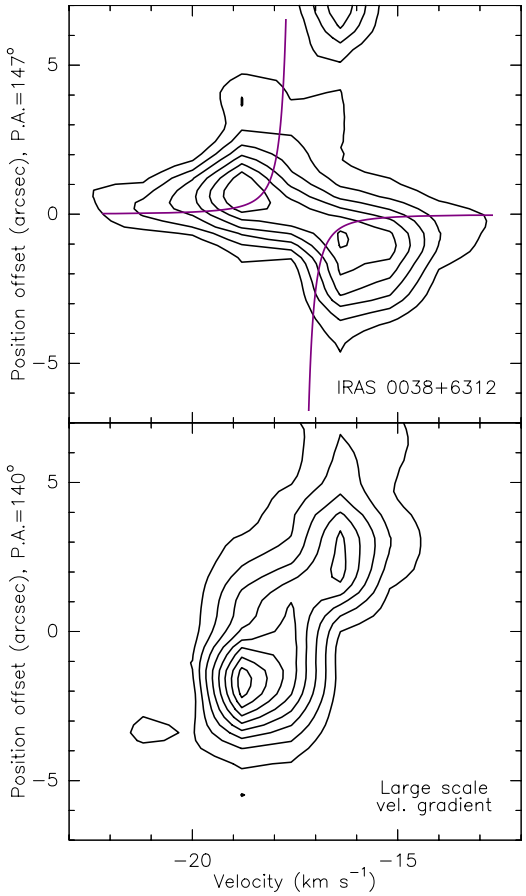

Fig. 4.10 DCN (3–2) position-velocity maps. *Upper panel*: Emission along the velocity gradient at the IRAS 0038+6312 source. Contours are $-3, 3, 5, 7, ..., 13$ times the rms noise level of the map, 0.03 Jy beam^{-1}. The purple lines indicate a keplerian velocity distribution. *Lower panel*: Emission along the large velocity gradient passing through the center of the toroid traced by the dust continuum emission. Contours are $-3, 3, 6, 9, ..., 24$ times the rms noise level of the map, 0.03 Jy beam^{-1}.

4.4.2 Molecular outflow

Powering source

The powering source of the reported northeast-southwest bipolar outflow in L1287 has been a matter of debate in the past. Several sources have been proposed, as RNO1B/1C by Staude and Neckel (1991), VLA 3 by Anglada et al. (1994) and IRAS 0038+6312 by Yang et al. (1995), but their results were not conclusive. In Sec. 4.3.2, we showed the outflow tracer CO $(2-1)$ high-velocity emission. The center of the bipolar molecular outflow is close to both IRAS 00338+6312 and FU-Orionis candidate RNO1C. However, at the first and second panels of Fig. 4.7, at ± 12 and ± 16 km s^{-1} from the systemic velocity, the IRAS

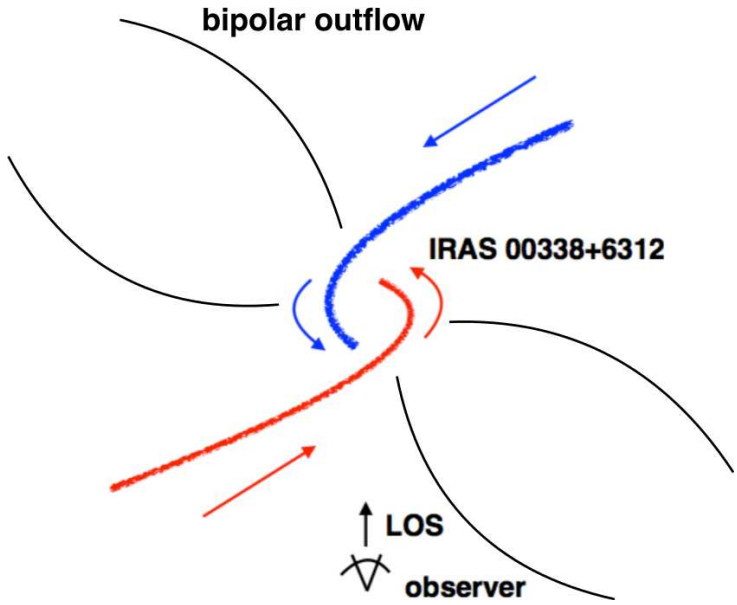

Fig. 4.11 Schematic model of the L1287 region. Converging flows+rotation dynamics. The blue and red lines indicate the ~ 0.1 pc scale molecular gas converging towards the center. We can observe a reversed velocity gradient projected towards our line of sight as we can see at the IRAS 00338+6312 source.

00338+6312 source seems located closer to the center than RNO1C. Also, as we have seen in Sec. 4.3.2, IRAS 00338+6312 presents a clear velocity gradient perpendicular to the structure of the bipolar outflow. Thus, it seems clear that IRAS 00338+6312 is more likely to be the powering source of the northeast-southwest bipolar outflow in the region.

On the other hand, the CO $(2-1)$ high-velocity emission is complex and the highest-velocity emission seem to be associated to RNO1C (see Fig. 4.9). This emission seems to correspond to a monopolar outflow, as only blue-shifted emission is detected. Probably there is no molecular gas which could interact with the red-shifted part of the outflow. Then, it seems that in addition to the northeast-southwest bipolar outflow, there could be also an additional molecular outflow powered by the FU-Orionis candidate RNO1C.

Outflow feedback

As previously shown in Fig. 4.8, it seems clear that the large-scale northeast-southwest molecular outflow has some interaction with the surrounding dense gas. In addition, in Fig. 4.12 we show the molecular outflow an the kinetic temperature map (Sepúlveda et al. in prep.) extracted from the NH_3 emission which traces more extended dense gas. We observe how the higher temperatures coincide well with the outflow structure, especially

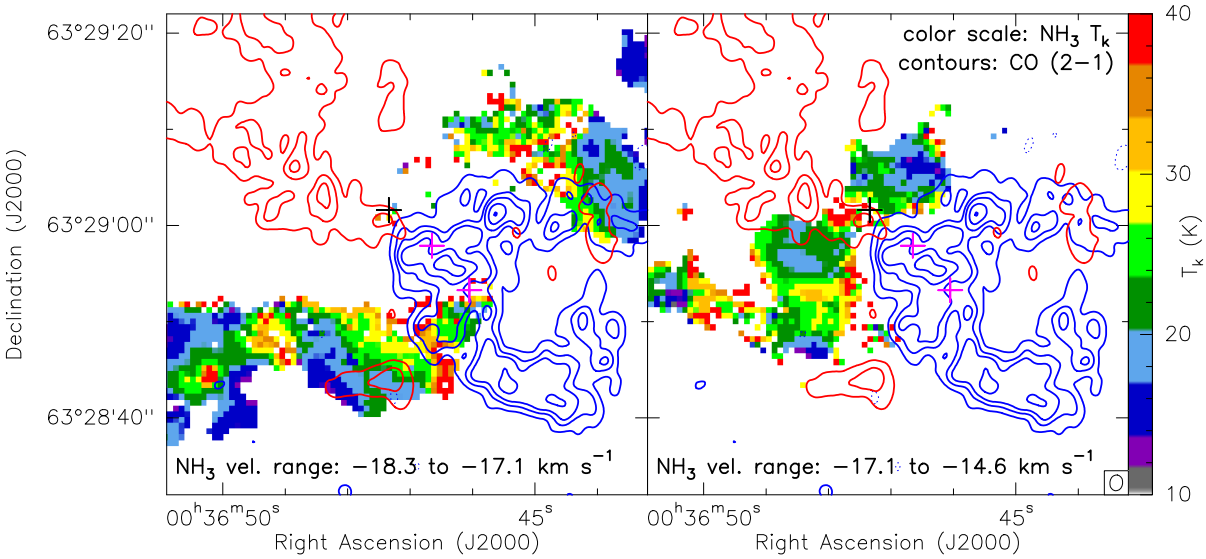

Fig. 4.12 *Contours*: same as in Fig. 4.8. *Color scale*: Kinetic temperature from the ratio between NH_3 (2,2) and (1,1) transitions. Both panels present different velocity components of the ammonia emission. The black and pink crosses indicate the position of IRAS 00338+6312, and FU-Orionis candidates RNO1C and RNO1B, respectively.

around the blue lobe and near IRAS 00338+6312. Also, the outflow seems to have caused the cavities we observed in the dense gas traced by the ammonia molecule.

Thus, it seems clear that the northeast-southwest molecular outflow is interacting with the dense gas affecting the chemistry and producing a complex large-scale kinematics in L1287. Furthermore, the highest-velocity gas detected with CO (at ~ 30 km s^{-1} from the systemic velocity) near RNO1C, is almost coinciding with the dust hole at the center of the toroid (see Fig. 4.9), suggesting that the high-velocity gas may have produced this cavity and may have also affected the rest of the dust continuum structure. Furthermore, the nature of the millimeter sources detected using only the extended configuration of the SMA can be discussed. One possibility is that some of the fragments may not form stars in the future and the structure observed in the dust continuum is just a consequence of the molecular outflow which shapes the dust and dense gas in the region. On the other hand, if we consider that the continuum sources forming the toroid and spiral structures will form stars in the future, the interaction of the outflow with the gas and dust in the region may have been responsible of triggering star formation in L1287.

4.4.3 Comparison with the case of NGC 6334 V

As we have studied in the previous Chapter, the intermediate/high-mass star-forming region NGC 6334 V presents clear features of a converging flow scenario. As we have shown in

Figs. 3.7, 4.5, 4.6 and 4.10, the velocity structures observed in both regions seem to trace two converging flows separated by similar velocities between $\sim 2-3$ km s^{-1}. Furthermore, the spatial scales are comparable, as the dense molecular gas flows are observed at spatial scales of ~ 0.1 pc converging towards higher-density regions at ~ 0.02 pc scales.

Regarding the mass of each region, we compare the mass enclosed in an area of ~ 0.1 pc diameter, as both regions are located at slightly different distances of 1.3 and 0.929 kpc. Assuming a temperature of 30 K for NGC 6334 V and 20 K for L1287, as all NGC 6334 V main dust continuum peaks have high-velocity gas associated (see Sec. 3.3.1), we obtain ~ 46 and ~ 22 M$_\odot$, respectively. Even though the uncertainty in the masses due to the opacity law and temperature is estimated to be a factor of 4, NGC 6334 V seems to be a more massive star-forming region. Also, the bolometric luminosity of NGC 6334 V ($\sim 10^4$ L$_\odot$) is one order of magnitude larger than the luminosity of L1287 (~ 600 L$_\odot$). Nevertheless, even though both regions differ in mass, they seem to present a very similar scenario of converging flows.

Finally, both regions present sources at different stages of evolution, harboring several centimeter and infrared sources (classified as Class 0/I-II objects) as well as still very deeply embedded protostars. As discussed in Sec. 1.4.4, different population of objects are expected in a global hierarchical collapse scenario, for which converging flows are a signature, with the massive stars forming late in the global process (Vazquez-Semadeni et al., 2016).

4.5 Summary

We analyzed 230 GHz SMA observations towards the low-mass star-forming region L1287. The main results are as follows:

- The dust continuum emission shows six main cores with masses between ~ 0.4 and ~ 4 M$_\odot$. The central core (associated to FU-Orionis candidate RNO1C and VLA 1) and the northeast core (associated to the YSO IRAS 0038+6312 and VLA 3) are the most massive ones, with ~ 4 and ~ 2 M$_\odot$, respectively. The cores present a mean size of ~ 0.02 pc ($\sim$4,500 au) and are separated by a mean distance of ~ 0.03 pc ($\sim$6,500 au). The total mass in the region is 25 M$_\odot$. The high-angular resolution image (using only the extended configuration data) shows a ~ 0.02 pc scale clumpy toroid connected with ~ 0.04 pc scale spiral arms towards the north and south, and strong continuum emission towards IRAS 00338+6312. We identified 14 dust condensations with masses ranging from 0.12 to 0.78 M$_\odot$, with the condensation associated to IRAS 00338+6312 being the most massive one.

- 15 molecular lines were identified, including several transitions of the dense core tracers CH_3OH and H_2CO, the shock tracers SO, OCS and SiO, and the deuterated molecules DCN and DNC. The dense gas tracer DCN (3–2) traces well the dust continuum emission and shows a clear velocity gradient between -15 and -19 km s^{-1} centered near the center of the region. Also, a reverse velocity gradient is observed towards the IRAS 00338+6312 position. The total mass estimated from the large-scale velocity gradient indicates that the gas is gravitationally bound.

- The dynamics in the region can be understood by a single scenario of converging flows+rotation towards the compact high-density region at the IRAS 00338+6312 position. This scenario of converging flows is similar to the higher-mass case of NGC 6334 V. Both regions show low-velocity ($2-3$ km s^{-1}) molecular gas structures converging from large scales (~ 0.1 pc) to the highest-density regions at ~ 0.02 pc scales.

- IRAS 0038+6312 seems to be the most likely powering source of the previously reported northeast-southwest bipolar outflow as it is located at the center of symmetry of both outflow lobes and its velocity gradient is oriented perpendicular to the outflow direction. The FU-Orionis candidate RNO1C seems to be the powering source of an additional molecular outflow, as it presents very high-velocity CO (2–1) emission elongated in the north-south direction. The high-velocity gas associated to the molecular outflows seems to have interacted with the dense gas and dust affecting the structure, the chemistry and the large-scale kinematics of L1287.

Chapter 5

Conclusions and future work

5.1 Conclusions

The aim of the thesis has focused on the study of the different collapse scenarios and the role of the magnetic field in star-forming regions at dense core scales (< 0.1 pc). For that we have used millimeter and submillimeter observational data from the interferometers Plateau de Bure (PdBI) and Submillimeter Array (SMA) and from the IRAM 30m single-dish telescope. The studies have been performed towards 3 different low- and high-mass star-forming regions located in different environments and evolutionary states.

In the first project, we wanted to study the earliest stages of star formation observing the pre-stellar core FeSt 1-457. We have seen that the core is located at the edge between two molecular structures separated by 3 km s^{-1}, possibly two flows of dense gas that interacts just at the position of the pre-stellar core. From polarization data taken from Alves et al. (2014) and the N_2H^+ data analysis, we obtained an approximation for the plane of the sky component of the magnetic field strength, ~ 45 μG. We also obtained that the core is magnetically supercritical, which means that the magnetic field is not strong enough to avoid the collapse. On the other hand, estimating the abundances of each molecular line detected, we found depletion of the molecules onto the dust grains towards the interior of the core, where grain growth (Forbrich et al., 2015) and depolarization also take place, suggesting these properties may be related. Moreover, the asymmetries found in the molecular emission seem to be correlated with the submillimeter polarization asymmetry. Both asymmetries could be due to a interstellar radiation field from the west side of the core.

In the second project, the observations of the kinematics and magnetic field towards the intermediate/high-mass star-forming region NGC 6334 V, show how the gas is accreted from the core envelope at large scales of ~ 0.1 pc towards the highest-density hot core region at ~ 0.02 pc scales. The gas is accreted through two flows of dense gas, traced by two different

velocity structures separated by $2-3$ km s^{-1}, and drags the magnetic field, whose strength seems to have been overcome by gravity. Furthermore, from 3D numerical simulations of star-forming regions dominated by gravity we observed a very similar scenario (at similar spatial scales), of two different velocity structures also separated by $2-3$ km s^{-1}, and dragging the magnetic field lines towards the potential well of the region. In addition, the polarization angular dispersion function generated for both observations and simulations also reveals a very similar behavior and gives an estimated magnetic field strength on the plane of the sky of ~ 1 mG.

The third project aims to study the dust structure and kinematics towards the lower-mass cluster-forming region L1287. In this case polarization observations providing the magnetic field information were not available as the capabilities of the instruments at the time of the observations were not sensitive enough. These polarization observations will be a possible future project thanks to the recent improvement of the available instruments. Towards L1287 we observe a similar scenario to the more massive case of NGC 6334 V, with two velocity structures also separated by 2–3 km s^{-1} which seem to converge towards the potential well in the region, the young stellar object IRAS 00338+6312. In addition, the molecular outflow seems to have interacted with the surrounding dense gas in the region. The complex kinematics of the dense gas that spatially coincides with the outflow seems clearly affected, especially the blue-shifted structure towards the southwestern part. Also, the chemistry has been affected by the outflow, showing emission from shock tracers SO and SiO. Finally, it seems clear that IRAS 00338+6312 is the powering source of this outflow.

The studies towards the pre-stellar core FeSt 1-457 and the high-mass star-forming region NGC 6334 V show that the magnetic field in both regions has been overcome by gravity and is not enough to avoid the gravitational collapse. In the case of FeSt 1-457, the core is in a very early evolutionary state and isolated in a magnetized environment. The location of the core, at the edge between two different gas flows, may have affected the evolution of the core. A Bonnor-Ebert sphere fit shows that the core is clearly unstable against gravitational collapse. Moreover, the mass-to-flux ratio estimation shows that the core is magnetically supercritical, which means that the magnetic support is insufficient to maintain its stability. NGC 6334 V, on the other hand, is a more evolved and massive star-forming region, harboring several infrared and radio sources, and high-velocity gas from molecular outflows. In this case, we also observed how gravity dominates over the magnetic field, as we see how the magnetic field is dragged by the converging gas structures.

On the other hand, NGC 6334 V and the lower-mass cluster-forming region L1287 present similar scenarios with the material being accreted from the larger-scale envelope (~ 0.1 pc) towards the potential wells of both regions at smaller scales (~ 0.02 pc), through

converging flows with velocities separated by 2–3 km s^{-1}. In addition, both regions have similar characteristics as they present sources at different stages of evolution, harboring several centimeter and infrared sources as well as still very deeply embedded protostars. As we have discussed, different population of objects and converging flows are characteristics of a global hierarchical collapse scenario, however we cannot discard a turbulent medium.

In a similar scenario to NGC 6334 V and L1287, FeSt 1-457 seems to be located at the converging point between two gas flows, also separated by 3 km s^{-1}, however, in this case the observations are tracing two lower-density gas structures. The location of the core precisely at the edge of the two flows could have affected its evolution. We have seen that the thermal pressure in the core seems to be dominant over the turbulent pressure and that the pre-stellar core is already collapsing with the magnetic field not being strong enough to stop it. Contrary to the case of NGC 6334 V and L1287, in FeSt 1-457 only one of the two low-density gas structures is associated to the core. In this case, the magnetic field and the velocity gradient orientations are perpendicular (contrary to the case of NGC 6334 V). Even though we have seen that gravity is the dominant force in FeSt 1-457, it is possible that the magnetic field is strong enough to be dynamically more important than in the more massive cases.

5.2 Future work

Several ideas for future work have been developed during the course of the projects.

In relation to the work done towards FeSt 1-457, it would be interesting to take advantage of the high-angular resolution in combination with good sensitivity of ALMA observatory to confirm and analyze the arc-like feature observed from N_2H^+ emission at the center of the core and examine if it is due to chemical effects, or if instead, it reflects an actual physical structure. If the structure in the inner region of the core is also detected with a different tracer of high-density regions, as for example NH_2D, it will confirm it is a real physical structure. On the other hand, if the feature is a chemical effect related to N_2H^+, as freeze out of the gas onto the grains, we should not observe it in other high-density gas tracers.

Secondly, we would like to continue the work on NGC 6334 V and use ALMA to observe, in high-angular resolution, the inner region of the hot core. We are interested in observing shock tracers, as for example SiO, to analyze the interaction between the two converging flows. Furthermore, we would like to observe the polarized emission from the dust to study the magnetic field near the shock. In addition, these observations would allow us to search for protostellar disks, and to determine if the large-scale structure is associated to them. We could unveil how the magnetic field in the converging flow is connected to the

forming young stellar object(s) and their disk(s) on the small scale. This study could provide insight about the global hierarchical collapse star formation model and to disk formation in such systems.

In a similar way as in NGC 6334 V, we would like to continue the analysis of the L1287 region observing the dust polarized emission to add the magnetic field information. Until now this was not possible as the instruments did not provide the sensitivity required to detect the polarized emission in this faint region. From the analysis of the magnetic field we would be able to further confirm whether such cluster-forming environment can be described by a converging flows scenario. In a broader context, we would be able to also study if the magnetic field is dominated by the kinematics and gravity in such systems or, on the contrary, the magnetic field plays a more dominant role influencing the dynamics and the final gravitational collapse of the region.

References

Aguti, E. D., Lada, C. J., Bergin, E. A., Alves, J. F., and Birkinshaw, M. (2007). The Dynamical State of the Starless Dense Core FeSt 1-457: A Pulsating Globule? *ApJ*, 665:457–465.

Aikawa, Y., Herbst, E., Roberts, H., and Caselli, P. (2005). Molecular Evolution in Collapsing Prestellar Cores. III. Contraction of a Bonnor-Ebert Sphere. *ApJ*, 620:330–346.

Alves, F. O. and Franco, G. A. P. (2007). An accurate determination of the distance to the Pipe nebula. *A& A*, 470:597–603.

Alves, F. O., Franco, G. A. P., and Girart, J. M. (2008). Optical polarimetry toward the Pipe nebula: revealing the importance of the magnetic field. *A& A*, 486:L13–L16.

Alves, F. O., Frau, P., Girart, J. M., Franco, G. A. P., Santos, F. P., and Wiesemeyer, H. (2014). On the radiation driven alignment of dust grains: Detection of the polarization hole in a starless core. *A& A*, 569:L1.

André, P., Revéret, V., Könyves, V., Arzoumanian, D., Tigé, J., Gallais, P., Roussel, H., Le Pennec, J., Rodriguez, L., Doumayrou, E., Dubreuil, D., Lortholary, M., Martignac, J., Talvard, M., Delisle, C., Visticot, F., Dumaye, L., De Breuck, C., Shimajiri, Y., Motte, F., Bontemps, S., Hennemann, M., Zavagno, A., Russeil, D., Schneider, N., Palmeirim, P., Peretto, N., Hill, T., Minier, V., Roy, A., and Rygl, K. L. J. (2016). Characterizing filaments in regions of high-mass star formation: High-resolution submilimeter imaging of the massive star-forming complex NGC 6334 with ArTéMiS. *A& A*, 592:A54.

Anglada, G., Rodriguez, L. F., Girart, J. M., Estalella, R., and Torrelles, J. M. (1994). A radio candidate for the exciting source of the L1287 bipolar outflow. *ApJL*, 420:L91–L93.

Ascenso, J., Lada, C. J., Alves, J., Román-Zúñiga, C. G., and Lombardi, M. (2013). The mid-infrared extinction law in the darkest cores of the Pipe Nebula. *A& A*, 549:A135.

Audit, E. and Hennebelle, P. (2005). Thermal condensation in a turbulent atomic hydrogen flow. *A& A*, 433:1–13.

Ballesteros-Paredes, J., Hartmann, L., and Vázquez-Semadeni, E. (1999a). Turbulent Flow-driven Molecular Cloud Formation: A Solution to the Post-T Tauri Problem? *ApJ*, 527:285–297.

Ballesteros-Paredes, J., Hartmann, L. W., Pérez-Goytia, N., and Kuznetsova, A. (2015). Bondi-Hoyle-Littleton accretion and the upper-mass stellar initial mass function. *MNRAS*, 452:566–574.

Ballesteros-Paredes, J., Vázquez-Semadeni, E., and Scalo, J. (1999b). Clouds as Turbulent Density Fluctuations: Implications for Pressure Confinement and Spectral Line Data Interpretation. *ApJ*, 515:286–303.

Banerjee, R. and Pudritz, R. E. (2007). Massive Star Formation via High Accretion Rates and Early Disk-driven Outflows. *ApJ*, 660:479–488.

Beccari, G., Spezzi, L., De Marchi, G., Paresce, F., Young, E., Andersen, M., Panagia, N., Balick, B., Bond, H., Calzetti, D., Carollo, C. M., Disney, M. J., Dopita, M. A., Frogel, J. A., Hall, D. N. B., Holtzman, J. A., Kimble, R. A., McCarthy, P. J., O'Connell, R. W., Saha, A., Silk, J. I., Trauger, J. T., Walker, A. R., Whitmore, B. C., and Windhorst, R. A. (2010). Progressive Star Formation in the Young Galactic Super Star Cluster NGC 3603. *ApJ*, 720:1108–1117.

Belloche, A. and André, P. (2004). Disappearance of N_2H^+ from the gas phase in the class 0 protostar IRAM 04191. *A& A*, 419:L35–L38.

Beltrán, M. T., Cesaroni, R., Codella, C., Testi, L., Furuya, R. S., and Olmi, L. (2006). Infall of gas as the formation mechanism of stars up to 20 times more massive than the Sun. *Nature*, 443:427–429.

Beltrán, M. T., Estalella, R., Anglada, G., Rodríguez, L. F., and Torrelles, J. M. (2001). Radio Spectral Indices of the Powering Sources of Outflows. *AJ*, 121:1556–1568.

Bergin, E. A. and Tafalla, M. (2007). Cold Dark Clouds: The Initial Conditions for Star Formation. *ARA&A*, 45:339–396.

Bertram, E., Federrath, C., Banerjee, R., and Klessen, R. S. (2012). Statistical analysis of the mass-to-flux ratio in turbulent cores: effects of magnetic field reversals and dynamo amplification. *MNRAS*, 420:3163–3173.

Bonazzola, S., Heyvaerts, J., Falgarone, E., Perault, M., and Puget, J. L. (1987). Jeans collapse in a turbulent medium. *A& A*, 172:293–298.

Bonnell, I. A. and Bate, M. R. (2006). Star formation through gravitational collapse and competitive accretion. *MNRAS*, 370:488–494.

Bonnell, I. A., Bate, M. R., Clarke, C. J., and Pringle, J. E. (1997). Accretion and the stellar mass spectrum in small clusters. *MNRAS*, 285:201–208.

Bonnell, I. A., Bate, M. R., Clarke, C. J., and Pringle, J. E. (2001). Competitive accretion in embedded stellar clusters. *MNRAS*, 323:785–794.

Bonnell, I. A., Bate, M. R., and Zinnecker, H. (1998). On the formation of massive stars. *MNRAS*, 298:93–102.

Bonnor, W. B. (1956). Boyle's Law and gravitational instability. *MNRAS*, 116:351.

Bourke, T. L., Myers, P. C., Robinson, G., and Hyland, A. R. (2001). New OH Zeeman Measurements of Magnetic Field Strengths in Molecular Clouds. *ApJ*, 554:916–932.

Briggs, D. S. (1995). High Fidelity Interferometric Imaging: Robust Weighting and NNLS Deconvolution. In *American Astronomical Society Meeting Abstracts*, volume 27 of *Bulletin of the American Astronomical Society*, page 1444.

Brinch, C. and Hogerheijde, M. R. (2010). LIME - a flexible, non-LTE line excitation and radiation transfer method for millimeter and far-infrared wavelengths. *A& A*, 523:A25.

Brooks, K. J. and Whiteoak, J. B. (2001). Ground-state OH observations towards NGC 6334. *MNRAS*, 320:465–476.

Busquet, G., Palau, A., Estalella, R., Girart, J. M., Sánchez-Monge, Á., Viti, S., Ho, P. T. P., and Zhang, Q. (2010). The NH_2D/NH_3 ratio toward pre-protostellar cores around the UC H II region in IRAS 20293+3952. *A& A*, 517:L6.

Caselli, P., Myers, P. C., and Thaddeus, P. (1995). Radio-astronomical Spectroscopy of the Hyperfine Structure of N 2H +. *ApJL*, 455:L77.

Caselli, P., Walmsley, C. M., Terzieva, R., and Herbst, E. (1998). The Ionization Fraction in Dense Cloud Cores. *ApJ*, 499:234–249.

Caselli, P., Walmsley, C. M., Zucconi, A., Tafalla, M., Dore, L., and Myers, P. C. (2002). Molecular Ions in L1544. II. The Ionization Degree. *ApJ*, 565:344–358.

Chandra, S. and Kegel, W. H. (2000). Collisional rates for asymmetrical top molecules. *A&AS*, 142:113–118.

Chandrasekhar, S. (1951). The Gravitational Instability of an Infinite Homogeneous Turbulent Medium. *Proceedings of the Royal Society of London Series A*, 210:26–29.

Chandrasekhar, S. and Fermi, E. (1953). Magnetic Fields in Spiral Arms. *ApJ*, 118:113.

Chibueze, J. O., Omodaka, T., Handa, T., Imai, H., Kurayama, T., Nagayama, T., Sunada, K., Nakano, M., Hirota, T., and Honma, M. (2014). Astrometry and Spatio-kinematics of H_2O Masers in the Massive Star-forming Region NGC 6334I(North) with VERA. *ApJ*, 784:114.

Chin, Y.-N., Henkel, C., Whiteoak, J. B., Langer, N., and Churchwell, E. B. (1995). VizieR Online Data Catalog: Interstellar S isotopes (Chin+, 1996). *VizieR Online Data Catalog*, 330.

Ciolek, G. E. and Mouschovias, T. C. (1994). Ambipolar diffusion, interstellar dust, and the formation of cloud cores and protostars. 3: Typical axisymmetric solutions. *ApJ*, 425:142–160.

Colín, P., Vázquez-Semadeni, E., and Gómez, G. C. (2013). Molecular cloud evolution - V. Cloud destruction by stellar feedback. *MNRAS*, 435:1701–1714.

Cortes, P. C., Girart, J. M., Hull, C. L. H., Sridharan, T. K., Louvet, F., Plambeck, R., Li, Z.-Y., Crutcher, R. M., and Lai, S.-P. (2016). Interferometric Mapping of Magnetic Fields: The ALMA View of the Massive Star-forming Clump W43-MM1. *ApJL*, 825:L15.

Crapsi, A., Caselli, P., Walmsley, C. M., Myers, P. C., Tafalla, M., Lee, C. W., and Bourke, T. L. (2005). Probing the Evolutionary Status of Starless Cores through N_2H^+ and N_2D^+ Observations. *ApJ*, 619:379–406.

Crapsi, A., Caselli, P., Walmsley, M. C., and Tafalla, M. (2007). Observing the gas temperature drop in the high-density nucleus of L 1544. *A& A*, 470:221–230.

Crutcher, R. M. (2012). Magnetic Fields in Molecular Clouds. *ARA&A*, 50:29–63.

Crutcher, R. M., Wandelt, B., Heiles, C., Falgarone, E., and Troland, T. H. (2010). Magnetic Fields in Interstellar Clouds from Zeeman Observations: Inference of Total Field Strengths by Bayesian Analysis. *ApJ*, 725:466–479.

Csengeri, T., Bontemps, S., Schneider, N., Motte, F., Gueth, F., and Hora, J. L. (2011). Convergent Flows and Low-velocity Shocks in DR21(OH). *ApJL*, 740:L5.

Dale, J. E., Ercolano, B., and Bonnell, I. A. (2015). Early evolution of embedded clusters. *MNRAS*, 451:987–1003.

Daniel, F., Cernicharo, J., and Dubernet, M.-L. (2006). The Excitation of N_2H^+ in Interstellar Molecular Clouds. I. Models. *ApJ*, 648:461–471.

Daniel, F., Dubernet, M.-L., Meuwly, M., Cernicharo, J., and Pagani, L. (2005). Collisional excitation rate coefficients of N_2H^+ by He. *MNRAS*, 363:1083–1091.

Davis, C. J., Kumar, M. S. N., Sandell, G., Froebrich, D., Smith, M. D., and Currie, M. J. (2007). WFCAM, Spitzer/IRAC and SCUBA observations of the massive star-forming region DR21/W75 - I. The collimated molecular jets. *MNRAS*, 374:29–53.

Davis, Jr., L. and Greenstein, J. L. (1951). The Polarization of Starlight by Aligned Dust Grains. *ApJ*, 114:206.

Dolginov, A. Z. and Mitrofanov, I. G. (1976). Orientation of cosmic dust grains. *Ap& SS*, 43:291–317.

Draine, B. T. and Weingartner, J. C. (1996). Radiative Torques on Interstellar Grains. I. Superthermal Spin-up. *ApJ*, 470:551.

Draine, B. T. and Weingartner, J. C. (1997). Radiative Torques on Interstellar Grains. II. Grain Alignment. *ApJ*, 480:633–646.

Duarte-Cabral, A., Bontemps, S., Motte, F., Gusdorf, A., Csengeri, T., Schneider, N., and Louvet, F. (2014). SiO emission from low- and high-velocity shocks in Cygnus-X massive dense clumps. *A& A*, 570:A1.

Dunham, M. M., Crapsi, A., Evans, II, N. J., Bourke, T. L., Huard, T. L., Myers, P. C., and Kauffmann, J. (2008). Identifying the Low-Luminosity Population of Embedded Protostars in the c2d Observations of Clouds and Cores. *ApJS*, 179:249–282.

Ebert, R. (1955). Über die Verdichtung von H I-Gebieten. Mit 5 Textabbildungen. *ZAp*, 37:217.

Estalella, R. (2016). HfS, Hyperfine Structure Fitting Tool. *ArXiv e-prints*.

Evans, II, N. J., Rawlings, J. M. C., Shirley, Y. L., and Mundy, L. G. (2001). Tracing the Mass during Low-Mass Star Formation. II. Modeling the Submillimeter Emission from Preprotostellar Cores. *ApJ*, 557:193–208.

Faúndez, S., Bronfman, L., Garay, G., Chini, R., Nyman, L.-Å., and May, J. (2004). SIMBA survey of southern high-mass star forming regions. I. Physical parameters of the 1.2 mm/IRAS sources. *A& A*, 426:97–103.

Federrath, C., Banerjee, R., Clark, P. C., and Klessen, R. S. (2010). Modeling Collapse and Accretion in Turbulent Gas Clouds: Implementation and Comparison of Sink Particles in AMR and SPH. *ApJ*, 713:269–290.

Fedoseev, G., Ioppolo, S., and Linnartz, H. (2015). Deuterium enrichment of ammonia produced by surface N+H/D addition reactions at low temperature. *MNRAS*, 446:449–458.

Feitzinger, J. V. and Stuewe, J. A. (1984). Catalogue of dark nebulae and globules for galactic longitudes 240 to 360 degrees. *A&AS*, 58:365–369.

Fernández-López, M., Girart, J. M., Curiel, S., Zapata, L. A., Fonfría, J. P., and Qiu, K. (2013). Multiple Monopolar Outflows Driven by Massive Protostars in IRAS 18162-2048. *ApJ*, 778:72.

Fiedler, R. A. and Mouschovias, T. C. (1993). Ambipolar Diffusion and Star Formation: Formation and Contraction of Axisymmetric Cloud Cores. II. Results. *ApJ*, 415:680.

Fischer, J., Joyce, R. R., Simon, M., and Simon, T. (1982). Near-infrared observations of the far-infrared source V region in NGC 6334. *ApJ*, 258:165–169.

Fissel, L. M., Ade, P. A. R., Angilè, F. E., Ashton, P., Benton, S. J., Devlin, M. J., Dober, B., Fukui, Y., Galitzki, N., Gandilo, N. N., Klein, J., Korotkov, A. L., Li, Z.-Y., Martin, P. G., Matthews, T. G., Moncelsi, L., Nakamura, F., Netterfield, C. B., Novak, G., Pascale, E., Poidevin, F., Santos, F. P., Savini, G., Scott, D., Shariff, J. A., Diego Soler, J., Thomas, N. E., Tucker, C. E., Tucker, G. S., and Ward-Thompson, D. (2016). Balloon-Borne Submillimeter Polarimetry of the Vela C Molecular Cloud: Systematic Dependence of Polarization Fraction on Column Density and Local Polarization-Angle Dispersion. *ApJ*, 824:134.

Flower, D. R. (1999). Rotational excitation of HCOˆ+ by H_2. *MNRAS*, 305:651–653.

Fontani, F., Busquet, G., Palau, A., Caselli, P., Sánchez-Monge, Á., Tan, J. C., and Audard, M. (2015). Deuteration and evolution in the massive star formation process. The role of surface chemistry. *A& A*, 575:A87.

Forbrich, J., Lada, C. J., Lombardi, M., Román-Zúñiga, C., and Alves, J. (2015). Smoke in the Pipe Nebula: dust emission and grain growth in the starless core FeSt 1-457. *A& A*, 580:A114.

Forbrich, J., Lada, C. J., Muench, A. A., Alves, J., and Lombardi, M. (2009). A Spitzer Census of Star Formation Activity in the Pipe Nebula. *ApJ*, 704:292–305.

Forster, J. R. and Caswell, J. L. (1989). The spatial relationship of OH and H2O masers. *A& A*, 213:339–350.

Franco, G. A. P., Alves, F. O., and Girart, J. M. (2010). Detailed Interstellar Polarimetric Properties of the Pipe Nebula at Core Scales. *ApJ*, 723:146–165.

Franco, J., Shore, S. N., and Tenorio-Tagle, G. (1994). On the massive star-forming capacity of molecular clouds. *ApJ*, 436:795–799.

Frau, P., Galli, D., and Girart, J. M. (2011). Comparing star formation models with interferometric observations of the protostar NGC 1333 IRAS 4A. I. Magnetohydrodynamic collapse models. *A& A*, 535:A44.

Frau, P., Girart, J. M., Alves, F. O., Franco, G. A. P., Onishi, T., and Román-Zúñiga, C. G. (2015). Formation of dense structures induced by filament collisions. Correlation of density, kinematics, and magnetic field in the Pipe nebula. *A& A*, 574:L6.

Frau, P., Girart, J. M., and Beltrán, M. T. (2012a). Chemical differentiation toward the Pipe nebula starless cores. *A& A*, 537:L9.

Frau, P., Girart, J. M., Beltrán, M. T., Morata, O., Masqué, J. M., Busquet, G., Alves, F. O., Sánchez-Monge, Á., Estalella, R., and Franco, G. A. P. (2010). Young Starless Cores Embedded in the Magnetically Dominated Pipe Nebula. *ApJ*, 723:1665–1677.

Frau, P., Girart, J. M., Beltrán, M. T., Padovani, M., Busquet, G., Morata, O., Masqué, J. M., Alves, F. O., Sánchez-Monge, Á., Franco, G. A. P., and Estalella, R. (2012b). Young Starless Cores Embedded in the Magnetically Dominated Pipe Nebula. II. Extended Data Set. *ApJ*, 759:3.

Frau, P., Girart, J. M., Zhang, Q., and Rao, R. (2014). Shaping a high-mass star-forming cluster through stellar feedback. The case of the NGC 7538 IRS 1-3 complex. *A& A*, 567:A116.

Fryxell, B., Olson, K., Ricker, P., Timmes, F. X., Zingale, M., Lamb, D. Q., MacNeice, P., Rosner, R., Truran, J. W., and Tufo, H. (2000). FLASH: An Adaptive Mesh Hydrodynamics Code for Modeling Astrophysical Thermonuclear Flashes. *ApJS*, 131:273–334.

Galli, D. and Shu, F. H. (1993a). Collapse of Magnetized Molecular Cloud Cores. I. Semianalytical Solution. *ApJ*, 417:220.

Galli, D. and Shu, F. H. (1993b). Collapse of Magnetized Molecular Cloud Cores. II. Numerical Results. *ApJ*, 417:243.

Galván-Madrid, R., Zhang, Q., Keto, E., Ho, P. T. P., Zapata, L. A., Rodríguez, L. F., Pineda, J. E., and Vázquez-Semadeni, E. (2010). From the Convergence of Filaments to Disk-outflow Accretion: Massive Star Formation in W33A. *ApJ*, 725:17–28.

Gibb, E., Nummelin, A., Irvine, W. M., Whittet, D. C. B., and Bergman, P. (2000). Chemistry of the Organic-Rich Hot Core G327.3-0.6. *ApJ*, 545:309–326.

Girart, J. M., Beltrán, M. T., Zhang, Q., Rao, R., and Estalella, R. (2009). Magnetic Fields in the Formation of Massive Stars. *Science*, 324:1408.

Girart, J. M., Estalella, R., and Ho, P. T. P. (1998). On the Nature of the Molecular Condensation Downstream from HH 80 North. *ApJL*, 495:L59–L62.

Girart, J. M., Estalella, R., Ho, P. T. P., and Rudolph, A. L. (2000). A Multitransition HCO^+ Study in NGC 2264G: Anomalous Emission of the J=1–0 Line. *ApJ*, 539:763–774.

Girart, J. M., Frau, P., Zhang, Q., Koch, P. M., Qiu, K., Tang, Y.-W., Lai, S.-P., and Ho, P. T. P. (2013). DR 21(OH): A Highly Fragmented, Magnetized, Turbulent Dense Core. *ApJ*, 772:69.

Girart, J. M., Rao, R., and Marrone, D. P. (2006). Magnetic Fields in the Formation of Sun-Like Stars. *Science*, 313:812–814.

Girart, J. M., Torrelles, J. M., Estalella, R., Curiel, S., Anglada, G., Gómez, J. F., Carrasco-González, C., Cantó, J., Rodríguez, L. F., Patel, N. A., and Trinidad, M. A. (2016). SMA observations towards the compact, short-lived bipolar water maser outflow in the LkHα234 region. *MNRAS*, 462:352–361.

Girart, J. M., Viti, S., Williams, D. A., Estalella, R., and Ho, P. T. P. (2002). The molecular condensations ahead of Herbig-Haro objects. I. Multi-transition observations of HH 2. *A& A*, 388:1004–1015.

Goldreich, P. and Kwan, J. (1974). Molecular Clouds. *ApJ*, 189:441–454.

Green, S. and Chapman, S. (1978). Collisional excitation of interstellar molecules - Linear molecules CO, CS, OCS, and HC3N. *ApJS*, 37:169–194.

Green, S. and Thaddeus, P. (1974). Rotational Excitation of HCN by Collisions. *ApJ*, 191:653–658.

Gritschneder, M. and Lin, D. N. C. (2012). The Role of θ Oph in the Formation and Evolution of the Pipe Nebula – Is Star Formation Ever Isolated? *ApJL*, 754:L13.

Gundlach, B. and Blum, J. (2015). The Stickiness of Micrometer-sized Water-ice Particles. *ApJ*, 798:34.

Hardegree-Ullman, E., Harju, J., Juvela, M., Sipilä, O., Whittet, D. C. B., and Hotzel, S. (2013). Chemical and Physical Conditions in Molecular Cloud Core DC 000.4-19.5 (SL42) in Corona Australis. *ApJ*, 763:45.

Hartmann, L., Ballesteros-Paredes, J., and Bergin, E. A. (2001). Rapid Formation of Molecular Clouds and Stars in the Solar Neighborhood. *ApJ*, 562:852–868.

Hartmann, L. and Kenyon, S. J. (1985). On the nature of FU Orionis objects. *ApJ*, 299:462–478.

Harvey, P. M. and Gatley, I. (1983). Infrared observations of OB star formation in NGC 6334. *ApJ*, 269:613–624.

Harvey, P. M. and Wilking, B. A. (1984). NGC 6334-V - an infrared bipolar nebula. *ApJL*, 280:L19–L22.

Hashimoto, J., Tamura, M., Suto, H., Abe, L., Ishii, M., Kudo, T., and Mayama, S. (2007). Subarcsecond Near-Infrared Images of Massive Star Formation Region NGC 6334V. *PASJ*, 59:221–225.

Hatchell, J., Wilson, T., Drabek, E., Curtis, E., Richer, J., Nutter, D., Di Francesco, J., Ward-Thompson, D., and JCMT GBS Consortium (2013). The JCMT Gould Belt Survey: SCUBA-2 observations of radiative feedback in NGC 1333. *MNRAS*, 429:L10–L14.

Heitsch, F. and Hartmann, L. (2008). Rapid Molecular Cloud and Star Formation: Mechanisms and Movies. *ApJ*, 689:290–301.

Heitsch, F., Mac Low, M.-M., and Klessen, R. S. (2001). Gravitational Collapse in Turbulent Molecular Clouds. II. Magnetohydrodynamical Turbulence. *ApJ*, 547:280–291.

Herbig, G. H. (1977). Eruptive phenomena in early stellar evolution. *ApJ*, 217:693–715.

Hildebrand, R. H. (1983). The Determination of Cloud Masses and Dust Characteristics from Submillimetre Thermal Emission. *QJRAS*, 24:267.

Hildebrand, R. H. (1988). Magnetic fields and stardust. *QJRAS*, 29:327–351.

Hildebrand, R. H., Davidson, J. A., Dotson, J. L., Dowell, C. D., Novak, G., and Vaillancourt, J. E. (2000). A Primer on Far-Infrared Polarimetry. *PASP*, 112:1215–1235.

Hildebrand, R. H., Kirby, L., Dotson, J. L., Houde, M., and Vaillancourt, J. E. (2009). Dispersion of Magnetic Fields in Molecular Clouds. I. *ApJ*, 696:567–573.

Hillenbrand, L. A. and Hartmann, L. W. (1998). A Preliminary Study of the Orion Nebula Cluster Structure and Dynamics. *ApJ*, 492:540–553.

Ho, P. T. P., Moran, J. M., and Lo, K. Y. (2004). The Submillimeter Array. *ApJL*, 616:L1–L6.

Hoare, M. G., Kurtz, S. E., Lizano, S., Keto, E., and Hofner, P. (2007). Ultracompact Hii Regions and the Early Lives of Massive Stars. *Protostars and Planets V*, pages 181–196.

Hollenbach, D. J. and Tielens, A. G. G. M. (1997). Dense Photodissociation Regions (PDRs). *ARA&A*, 35:179–216.

Houde, M., Hull, C. L. H., Plambeck, R. L., Vaillancourt, J. E., and Hildebrand, R. H. (2016). Dispersion of Magnetic Fields in Molecular Clouds. IV. Analysis of Interferometry Data. *ApJ*, 820:38.

Houde, M., Rao, R., Vaillancourt, J. E., and Hildebrand, R. H. (2011). Dispersion of Magnetic Fields in Molecular Clouds. III. *ApJ*, 733:109.

Houde, M., Vaillancourt, J. E., Hildebrand, R. H., Chitsazzadeh, S., and Kirby, L. (2009). Dispersion of Magnetic Fields in Molecular Clouds. II. *ApJ*, 706:1504–1516.

Hull, C. L. H., Plambeck, R. L., Kwon, W., Bower, G. C., Carpenter, J. M., Crutcher, R. M., Fiege, J. D., Franzmann, E., Hakobian, N. S., Heiles, C., Houde, M., Hughes, A. M., Lamb, J. W., Looney, L. W., Marrone, D. P., Matthews, B. C., Pillai, T., Pound, M. W., Rahman, N., Sandell, G., Stephens, I. W., Tobin, J. J., Vaillancourt, J. E., Volgenau, N. H., and Wright, M. C. H. (2014). TADPOL: A 1.3 mm Survey of Dust Polarization in Star-forming Cores and Regions. *ApJS*, 213:13.

Hunter, T. R., Brogan, C. L., Megeath, S. T., Menten, K. M., Beuther, H., and Thorwirth, S. (2006). Millimeter Multiplicity in NGC 6334 I and I(N). *ApJ*, 649:888–893.

Jiménez-Serra, I., Caselli, P., Tan, J. C., Hernandez, A. K., Fontani, F., Butler, M. J., and van Loo, S. (2010). Parsec-scale SiO emission in an infrared dark cloud. *MNRAS*, 406:187–196.

Jørgensen, J., Brinch, C., Girart, J. M., Padovani, M., Frau, P., Schaaf, R., Kuiper, R., Bertoldi, F., Hogerheijde, M., Juhasz, A., and Vlemmings, W. (2014). ARTIST: Adaptable Radiative Transfer Innovations for Submillimeter Telescopes. Astrophysics Source Code Library.

Kandori, R., Nakajima, Y., Tamura, M., Tatematsu, K., Aikawa, Y., Naoi, T., Sugitani, K., Nakaya, H., Nagayama, T., Nagata, T., Kurita, M., Kato, D., Nagashima, C., and Sato, S. (2005). Near-Infrared Imaging Survey of Bok Globules: Density Structure. *AJ*, 130:2166–2184.

Kenyon, S. J., Hartmann, L., Gomez, M., Carr, J. S., and Tokunaga, A. (1993). RNO 1B/1C - A double FU Orionis system. *AJ*, 105:1505–1510.

Klaassen, P. D. and Wilson, C. D. (2008). Outflow and Infall in a Sample of Massive Star Forming Regions. II. Large-Scale Kinematics. *ApJ*, 684:1273–1280.

Klessen, R. S., Heitsch, F., and Mac Low, M.-M. (2000). Gravitational Collapse in Turbulent Molecular Clouds. I. Gasdynamical Turbulence. *ApJ*, 535:887–906.

Koch, P. M., Tang, Y.-W., and Ho, P. T. P. (2010). Magnetic Field Properties in High-mass Star Formation from Large to Small Scales: A Statistical Analysis from Polarization Data. *ApJ*, 721:815–827.

Koch, P. M., Tang, Y.-W., Ho, P. T. P., Zhang, Q., Girart, J. M., Chen, H.-R. V., Frau, P., Li, H.-B., Li, Z.-Y., Liu, H.-Y. B., Padovani, M., Qiu, K., Yen, H.-W., Chen, H.-H., Ching, T.-C., Lai, S.-P., and Rao, R. (2014). The Importance of the Magnetic Field from an SMA-CSO-combined Sample of Star-forming Regions. *ApJ*, 797:99.

Körtgen, B. and Banerjee, R. (2015). Impact of magnetic fields on molecular cloud formation and evolution. *MNRAS*, 451:3340–3353.

Kraemer, K. E., Deutsch, L. K., Jackson, J. M., Hora, J. L., Fazio, G. G., Hoffmann, W. F., and Dayal, A. (1999). The Mid-Infrared Properties of Three Star-forming Sites in NGC 6334. *ApJ*, 516:817–833.

Kraemer, K. E. and Jackson, J. M. (1995). Shock-excited NH3 (3, 3) masers in the NGC 6334 star-forming region. *ApJL*, 439:L9–L12.

Krumholz, M. R., McKee, C. F., and Klein, R. I. (2005). How Protostellar Outflows Help Massive Stars Form. *ApJL*, 618:L33–L36.

Kuhn, M. A., Getman, K. V., and Feigelson, E. D. (2015). The Spatial Structure of Young Stellar Clusters. II. Total Young Stellar Populations. *ApJ*, 802:60.

Kurtz, S., Cesaroni, R., Churchwell, E., Hofner, P., and Walmsley, C. M. (2000). Hot Molecular Cores and the Earliest Phases of High-Mass Star Formation. *Protostars and Planets IV*, pages 299–326.

Larson, R. B. (1969). Numerical calculations of the dynamics of collapsing proto-star. *MNRAS*, 145:271.

Launhardt, R., Stutz, A. M., Schmiedeke, A., Henning, T., Krause, O., Balog, Z., Beuther, H., Birkmann, S., Hennemann, M., Kainulainen, J., Khanzadyan, T., Linz, H., Lippok, N., Nielbock, M., Pitann, J., Ragan, S., Risacher, C., Schmalzl, M., Shirley, Y. L., Stecklum, B., Steinacker, J., and Tackenberg, J. (2013). The Earliest Phases of Star Formation (EPoS): a Herschel key project. The thermal structure of low-mass molecular cloud cores. *A& A*, 551:A98.

Lazarian, A. and Hoang, T. (2007). Radiative torques: analytical model and basic properties. *MNRAS*, 378:910–946.

Li, H.-B., Goodman, A., Sridharan, T. K., Houde, M., Li, Z.-Y., Novak, G., and Tang, K. S. (2014). The Link Between Magnetic Fields and Cloud/Star Formation. *Protostars and Planets VI*, pages 101–123.

Li, H.-B., Yuen, K. H., Otto, F., Leung, P. K., Sridharan, T. K., Zhang, Q., Liu, H., Tang, Y.-W., and Qiu, K. (2015). Self-similar fragmentation regulated by magnetic fields in a region forming massive stars. *Nature*, 520:518–521.

Lique, F., Dubernet, M.-L., Spielfiedel, A., and Feautrier, N. (2006a). Rotational excitation of sulfur monoxide in collision with helium at high temperature. *A& A*, 450:399–405.

Lique, F., Spielfiedel, A., and Cernicharo, J. (2006b). Rotational excitation of carbon monosulfide by collisions with helium. *A& A*, 451:1125–1132.

Lis, D. C., Serabyn, E., Keene, J., Dowell, C. D., Benford, D. J., Phillips, T. G., Hunter, T. R., and Wang, N. (1998). 350 Micron Continuum Imaging of the Orion A Molecular Cloud with the Submillimeter High Angular Resolution Camera. *ApJ*, 509:299–308.

Liu, H. B., Lai, S.-P., Hasegawa, Y., Hirano, N., Rao, R., Li, I.-H., Fukagawa, M., Girart, J. M., Carrasco-González, C., and Rodríguez, L. F. (2016). Detection of Linearly Polarized 6.9 mm Continuum Emission from the Class 0 Young Stellar Object NGC 1333 IRAS4A. *ApJ*, 821:41.

Liu, H. B., Qiu, K., Zhang, Q., Girart, J. M., and Ho, P. T. P. (2013a). Gas Kinematics and the Dragged Magnetic Field in the High-mass Molecular Outflow Source G192.16-3.84: An SMA View. *ApJ*, 771:71.

Liu, T., Wu, Y., and Zhang, H. (2013b). Gaseous CO Abundance – An Evolutionary Tracer for Molecular Clouds. *ApJL*, 775:L2.

Loison, J.-C., Wakelam, V., and Hickson, K. M. (2014). The interstellar gas-phase chemistry of HCN and HNC. *MNRAS*, 443:398–410.

Lombardi, M., Alves, J., and Lada, C. J. (2006). 2MASS wide field extinction maps. I. The Pipe nebula. *A& A*, 454:781–796.

Lommen, D., Wright, C. M., Maddison, S. T., Jørgensen, J. K., Bourke, T. L., van Dishoeck, E. F., Hughes, A., Wilner, D. J., Burton, M., and van Langevelde, H. J. (2007). Investigating grain growth in disks around southern T Tauri stars at millimetre wavelengths. *A& A*, 462:211–220.

Marrone, D. P., Moran, J. M., Zhao, J.-H., and Rao, R. (2006). Interferometric Measurements of Variable 340 GHz Linear Polarization in Sagittarius A*. *ApJ*, 640:308–318.

Marrone, D. P. and Rao, R. (2008). The submillimeter array polarimeter. In *Millimeter and Submillimeter Detectors and Instrumentation for Astronomy IV*, volume 7020 of *Proc. SPIE*, page 70202B.

Marsh, K. A., Griffin, M. J., Palmeirim, P., André, P., Kirk, J., Stamatellos, D., Ward-Thompson, D., Roy, A., Bontemps, S., Francesco, J. D., Elia, D., Hill, T., Könyves, V., Motte, F., Nguyen-Luong, Q., Peretto, N., Pezzuto, S., Rivera-Ingraham, A., Schneider, N., Spinoglio, L., and White, G. (2014). Properties of starless and prestellar cores in Taurus revealed by Herschel: SPIRE/PACS imaging. *MNRAS*, 439:3683–3693.

Masqué, J. M., Girart, J. M., Anglada, G., Osorio, M., Estalella, R., and Beltrán, M. T. (2013). Interferometric Observations of Nitrogen-bearing Molecular Species in the Star-forming Core Ahead of HH 80N. *ApJ*, 776:28.

Matthews, B. C., McPhee, C. A., Fissel, L. M., and Curran, R. L. (2009). The Legacy of SCUPOL: 850 μm Imaging Polarimetry from 1997 to 2005. *ApJS*, 182:143–204.

McKee, C. F. and Tan, J. C. (2002). Massive star formation in 100,000 years from turbulent and pressurized molecular clouds. *Nature*, 416:59–61.

McKee, C. F. and Tan, J. C. (2003). The Formation of Massive Stars from Turbulent Cores. *ApJ*, 585:850–871.

Mestel, L. and Spitzer, Jr., L. (1956). Star formation in magnetic dust clouds. *MNRAS*, 116:503.

Morata, O. and Herbst, E. (2008). Time-dependent models of dense PDRs with complex molecules. *MNRAS*, 390:1549–1561.

Mouschovias, T. C. (1991). Magnetic braking, ambipolar diffusion, cloud cores, and star formation - Natural length scales and protostellar masses. *ApJ*, 373:169–186.

Mouschovias, T. C. and Spitzer, Jr., L. (1976). Note on the collapse of magnetic interstellar clouds. *ApJ*, 210:326.

Muñoz, D. J., Mardones, D., Garay, G., Rebolledo, D., Brooks, K., and Bontemps, S. (2007). Massive Clumps in the NGC 6334 Star-forming Region. *ApJ*, 668:906–917.

Nakamura, F. and Li, Z.-Y. (2005). Quiescent Cores and the Efficiency of Turbulence-accelerated, Magnetically Regulated Star Formation. *ApJ*, 631:411–428.

Nakano, T. and Nakamura, T. (1978). Gravitational Instability of Magnetized Gaseous Disks 6. *PASJ*, 30:671–680.

Naranjo-Romero, R., Zapata, L. A., Vázquez-Semadeni, E., Takahashi, S., Palau, A., and Schilke, P. (2012). From Dusty Filaments to Massive Stars: The Case of NGC 7538 S. *ApJ*, 757:58.

Nguyen-Lu'o'ng, Q., Motte, F., Carlhoff, P., Louvet, F., Lesaffre, P., Schilke, P., Hill, T., Hennemann, M., Gusdorf, A., Didelon, P., Schneider, N., Bontemps, S., Duarte-Cabral, A., Menten, K. M., Martin, P. G., Wyrowski, F., Bendo, G., Roussel, H., Bernard, J.-P., Bronfman, L., Henning, T., Kramer, C., and Heitsch, F. (2013). Low-velocity Shocks Traced by Extended SiO Emission along the W43 Ridges: Witnessing the Formation of Young Massive Clusters. *ApJ*, 775:88.

Noriega-Crespo, A., Morris, P., Marleau, F. R., Carey, S., Boogert, A., van Dishoeck, E., Evans, II, N. J., Keene, J., Muzerolle, J., Stapelfeldt, K., Pontoppidan, K., Lowrance, P., Allen, L., and Bourke, T. L. (2004). A New Look at Stellar Outflows: Spitzer Observations of the HH 46/47 System. *ApJS*, 154:352–358.

Ossenkopf, V. and Henning, T. (1994). Dust opacities for protostellar cores. *A& A*, 291:943–959.

Ostriker, E. C., Stone, J. M., and Gammie, C. F. (2001). Density, Velocity, and Magnetic Field Structure in Turbulent Molecular Cloud Models. *ApJ*, 546:980–1005.

Padoan, P. (1995). Supersonic turbulent flows and the fragmentation of a cold medium. *MNRAS*, 277:377–388.

Padoan, P. and Nordlund, Å. (1999). A Super-Alfvénic Model of Dark Clouds. *ApJ*, 526:279–294.

Padovani, M., Brinch, C., Girart, J. M., Jørgensen, J. K., Frau, P., Hennebelle, P., Kuiper, R., Vlemmings, W. H. T., Bertoldi, F., Hogerheijde, M., Juhasz, A., and Schaaf, R. (2012). Adaptable radiative transfer innovations for submillimetre telescopes (ARTIST). Dust polarisation module (DustPol). *A& A*, 543:A16.

Padovani, M., Jørgensen, J. K., Bertoldi, F., Brinch, C., Frau, P., Girart, J. M., Hogerheijde, M., Juhasz, A., Kuiper, R., Schaaf, R., and Vlemmings, W. H. T. (2011). Adaptable Radiative Transfer Innovations for Submillimeter Telescopes (ARTIST). In Alves, J., Elmegreen, B. G., Girart, J. M., and Trimble, V., editors, *Computational Star Formation*, volume 270 of *IAU Symposium*, pages 451–454.

Pagani, L., Bacmann, A., Cabrit, S., and Vastel, C. (2007). Depletion and low gas temperature in the L183 (=L134N) prestellar core: the N2Hˆ+-N2D$^+$ tool. *A& A*, 467:179–186.

Palau, A., Ballesteros-Paredes, J., Vázquez-Semadeni, E., Sánchez-Monge, Á., Estalella, R., Fall, S. M., Zapata, L. A., Camacho, V., Gómez, L., Naranjo-Romero, R., Busquet, G., and Fontani, F. (2015). Gravity or turbulence? - III. Evidence of pure thermal Jeans fragmentation at $\sim$0.1 pc scale. *MNRAS*, 453:3785–3797.

Palau, A., Fuente, A., Girart, J. M., Estalella, R., Ho, P. T. P., Sánchez-Monge, Á., Fontani, F., Busquet, G., Commerçon, B., Hennebelle, P., Boissier, J., Zhang, Q., Cesaroni, R., and Zapata, L. A. (2013). Early Stages of Cluster Formation: Fragmentation of Massive Dense Cores down to $\lesssim$ 1000 AU. *ApJ*, 762:120.

Palau, A., Fuente, A., Girart, J. M., Fontani, F., Boissier, J., Piétu, V., Sánchez-Monge, Á., Busquet, G., Estalella, R., Zapata, L. A., Zhang, Q., Neri, R., Ho, P. T. P., Alonso-Albi, T., and Audard, M. (2011). Intermediate-mass Hot Cores at ˜500 AU: Disks or Outflows? *ApJL*, 743:L32.

Palau, A., Sánchez-Monge, Á., Busquet, G., Estalella, R., Zhang, Q., Ho, P. T. P., Beltrán, M. T., and Beuther, H. (2010). Three intermediate-mass young stellar objects with different properties emerging from the same natal cloud in IRAS 00117+6412. *A& A*, 510:A5.

Palla, F. and Stahler, S. W. (2000). Accelerating Star Formation in Clusters and Associations. *ApJ*, 540:255–270.

Patel, N. A., Curiel, S., Sridharan, T. K., Zhang, Q., Hunter, T. R., Ho, P. T. P., Torrelles, J. M., Moran, J. M., Gómez, J. F., and Anglada, G. (2005). A disk of dust and molecular gas around a high-mass protostar. *Nature*, 437:109–111.

Pety, J., Teyssier, D., Fossé, D., Gerin, M., Roueff, E., Abergel, A., Habart, E., and Cernicharo, J. (2005). Are PAHs precursors of small hydrocarbons in photo-dissociation regions? The Horsehead case. *A& A*, 435:885–899.

Piétu, V., Guilloteau, S., Di Folco, E., Dutrey, A., and Boehler, Y. (2014). Faint disks around classical T Tauri stars: Small but dense enough to form planets. *A& A*, 564:A95.

Pillai, T., Kauffmann, J., Tan, J. C., Goldsmith, P. F., Carey, S. J., and Menten, K. M. (2015). Magnetic Fields in High-mass Infrared Dark Clouds. *ApJ*, 799:74.

Qiu, K., Zhang, Q., Megeath, S. T., Gutermuth, R. A., Beuther, H., Shepherd, D. S., Sridharan, T. K., Testi, L., and De Pree, C. G. (2008). Spitzer IRAC and MIPS Imaging of Clusters and Outflows in Nine High-Mass Star Forming Regions. *ApJ*, 685:1005–1025.

Qiu, K., Zhang, Q., Menten, K. M., Liu, H. B., and Tang, Y.-W. (2013). From Poloidal to Toroidal: Detection of a Well-ordered Magnetic Field in the High-mass Protocluster G35.2-0.74 N. *ApJ*, 779:182.

Qiu, K., Zhang, Q., Menten, K. M., Liu, H. B., Tang, Y.-W., and Girart, J. M. (2014). Submillimeter Array Observations of Magnetic Fields in G240.31+0.07: An Hourglass in a Massive Cluster-forming Core. *ApJL*, 794:L18.

Quanz, S. P., Henning, T., Bouwman, J., Linz, H., and Lahuis, F. (2007). Deeply Embedded Objects and Shocked Molecular Hydrogen: The Environment of the FU Orionis Stars RNO 1B/1C. *ApJ*, 658:487–497.

Rabli, D. and Flower, D. R. (2010). The rotational excitation of methanol by molecular hydrogen. *MNRAS*, 406:95–101.

Raimond, E. and Eliasson, B. (1969). Positions and Stokes Parameters of Seven Oh-Emission Sources. *ApJ*, 155:817.

Rathborne, J. M., Lada, C. J., Muench, A. A., Alves, J. F., and Lombardi, M. (2008). The Nature of the Dense Core Population in the Pipe Nebula: A Survey of NH_3, CCS, and HC_5N Molecular Line Emission. *ApJS*, 174:396–425.

Reid, M. J., Menten, K. M., Brunthaler, A., Zheng, X. W., Dame, T. M., Xu, Y., Wu, Y., Zhang, B., Sanna, A., Sato, M., Hachisuka, K., Choi, Y. K., Immer, K., Moscadelli, L., Rygl, K. L. J., and Bartkiewicz, A. (2014). Trigonometric Parallaxes of High Mass Star Forming Regions: The Structure and Kinematics of the Milky Way. *ApJ*, 783:130.

Reid, M. J., Schneps, M. H., Moran, J. M., Gwinn, C. R., Genzel, R., Downes, D., and Roennaeng, B. (1988). The distance to the center of the Galaxy - H2O maser proper motions in Sagittarius B2(N). *ApJ*, 330:809–816.

Rengarajan, T. N. and Ho, P. T. P. (1996). Search for Optically Thick H II Regions and Ionized Stellar Wind from Luminous Embedded Infrared Sources. *ApJ*, 465:363.

Ricci, L., Trotta, F., Testi, L., Natta, A., Isella, A., and Wilner, D. J. (2012). The effect of local optically thick regions in the long-wave emission of young circumstellar disks. *A& A*, 540:A6.

Rimmer, P. B., Herbst, E., Morata, O., and Roueff, E. (2012). Observing a column-dependent ζ in dense interstellar sources: the case of the Horsehead nebula. *A& A*, 537:A7.

Roberts, H., Herbst, E., and Millar, T. J. (2003). Enhanced Deuterium Fractionation in Dense Interstellar Cores Resulting from Multiply Deuterated H^+_3. *ApJL*, 591:L41–L44.

Roberts, H., Herbst, E., and Millar, T. J. (2004). The chemistry of multiply deuterated species in cold, dense interstellar cores. *A& A*, 424:905–917.

Román-Zúñiga, C. G., Alves, J. F., Lada, C. J., and Lombardi, M. (2010). Deep Near-infrared Survey of the Pipe Nebula. II. Data, Methods, and Dust Extinction Maps. *ApJ*, 725:2232–2250.

Román-Zúñiga, C. G., Lada, C. J., and Alves, J. F. (2009). High Resolution Near-Infrared Survey of the Pipe Nebula. I. A Deep Infrared Extinction Map of Barnard 59. *ApJ*, 704:183–195.

Roy, A., André, P., Palmeirim, P., Attard, M., Könyves, V., Schneider, N., Peretto, N., Men'shchikov, A., Ward-Thompson, D., Kirk, J., Griffin, M., Marsh, K., Abergel, A., Arzoumanian, D., Benedettini, M., Hill, T., Motte, F., Nguyen Luong, Q., Pezzuto, S., Rivera-Ingraham, A., Roussel, H., Rygl, K. L. J., Spinoglio, L., Stamatellos, D., and White, G. (2014). Reconstructing the density and temperature structure of prestellar cores from Herschel data: A case study for B68 and L1689B. *A& A*, 562:A138.

Ruffle, D. P., Hartquist, T. W., Caselli, P., and Williams, D. A. (1999). The sulphur depletion problem. *MNRAS*, 306:691–695.

Ruoskanen, J., Harju, J., Juvela, M., Miettinen, O., Liljeström, A., Väisälä, M., Lunttila, T., and Kontinen, S. (2011). Mapping the prestellar core Ophiuchus D (L1696A) in ammonia. *A& A*, 534:A122.

Rygl, K. L. J., Brunthaler, A., Reid, M. J., Menten, K. M., van Langevelde, H. J., and Xu, Y. (2010). Trigonometric parallaxes of 6.7 GHz methanol masers. *A& A*, 511:A2.

Sánchez-Monge, Á., Palau, A., Fontani, F., Busquet, G., Juárez, C., Estalella, R., Tan, J. C., Sepúlveda, I., Ho, P. T. P., Zhang, Q., and Kurtz, S. (2013). Properties of dense cores in clustered massive star-forming regions at high angular resolution. *MNRAS*, 432:3288–3319.

Sault, R. J., Teuben, P. J., and Wright, M. C. H. (1995). A Retrospective View of MIRIAD. In Shaw, R. A., Payne, H. E., and Hayes, J. J. E., editors, *Astronomical Data Analysis Software and Systems IV*, volume 77 of *Astronomical Society of the Pacific Conference Series*, page 433.

Scoville, N. Z., Carlstrom, J. E., Chandler, C. J., Phillips, J. A., Scott, S. L., Tilanus, R. P. J., and Wang, Z. (1993). The relational database and calibration software for the Caltech millimeter array. *PASP*, 105:1482–1494.

Shu, F. H., Adams, F. C., and Lizano, S. (1987). Star formation in molecular clouds - Observation and theory. *ARA&A*, 25:23–81.

Simon, T., Dyck, H. M., Wolstencroft, R. D., McLean, I. S., Joyce, R. R., and Johnson, P. E. (1985). The morphology of NGC 6334 IRS V-1. *MNRAS*, 212:21P–25P.

Simpson, J. P., Burton, M. G., Colgan, S. W. J., Cotera, A. S., Erickson, E. F., Hines, D. C., and Whitney, B. A. (2009). Hubble Space Telescope NICMOS Polarization Observations of Three Edge-on Massive Young Stellar Objects. *ApJ*, 700:1488–1501.

Sipilä, O., Harju, J., and Juvela, M. (2011). On the stability of non-isothermal Bonnor-Ebert spheres. *A& A*, 535:A49.

Smith, H. A., Hora, J. L., Marengo, M., and Pipher, J. L. (2006). Outflows from Massive Young Stellar Objects as Seen with the Infrared Array Camera. *ApJ*, 645:1264–1271.

Snell, R. L., Dickman, R. L., and Huang, Y.-L. (1990). Molecular outflows associated with a flux-limited sample of bright far-infrared sources. *ApJ*, 352:139–148.

Soler, J. D., Alves, F., Boulanger, F., Bracco, A., Falgarone, E., Franco, G. A. P., Guillet, V., Hennebelle, P., Levrier, F., Martin, P. G., and Miville-Deschênes, M.-A. (2016). Magnetic field morphology in nearby molecular clouds as revealed by starlight and submillimetre polarization. *A& A*, 596:A93.

Staude, H. J. and Neckel, T. (1991). RNO 1B - A new FUor in Cassiopeia. *A& A*, 244:L13–L16.

Steer, D. G., Dewdney, P. E., and Ito, M. R. (1984). Enhancements to the deconvolution algorithm 'CLEAN'. *A& A*, 137:159–165.

Stone, J. M., Ostriker, E. C., and Gammie, C. F. (1998). Dissipation in Compressible Magnetohydrodynamic Turbulence. *ApJL*, 508:L99–L102.

Tafalla, M., Myers, P. C., Caselli, P., and Walmsley, C. M. (2004). On the internal structure of starless cores. I. Physical conditions and the distribution of CO, CS, N_2H^+, and NH_3 in L1498 and L1517B. *A& A*, 416:191–212.

Tafalla, M., Myers, P. C., Caselli, P., Walmsley, C. M., and Comito, C. (2002). Systematic Molecular Differentiation in Starless Cores. *ApJ*, 569:815–835.

Tafalla, M., Santiago-García, J., Myers, P. C., Caselli, P., Walmsley, C. M., and Crapsi, A. (2006). On the internal structure of starless cores. II. A molecular survey of L1498 and L1517B. *A& A*, 455:577–593.

Takami, M., Chen, H.-H., Karr, J. L., Lee, H.-T., Lai, S.-P., and Minh, Y.-C. (2012). Emission Mechanism of "Green Fuzzies" in High-mass Star-forming Regions. *ApJ*, 748:8.

Tang, Y.-W., Ho, P. T. P., Girart, J. M., Rao, R., Koch, P., and Lai, S.-P. (2009a). Evolution of Magnetic Fields in High Mass Star Formation: Submillimeter Array Dust Polarization Image of the Ultracompact H II Region G5.89-0.39. *ApJ*, 695:1399–1412.

Tang, Y.-W., Ho, P. T. P., Koch, P. M., Girart, J. M., Lai, S.-P., and Rao, R. (2009b). Evolution of Magnetic Fields in High-Mass Star Formation: Linking Field Geometry and Collapse for the W51 e2/e8 Cores. *ApJ*, 700:251–261.

Tang, Y.-W., Ho, P. T. P., Koch, P. M., Guilloteau, S., and Dutrey, A. (2013). Dust Continuum and Polarization from Envelope to Cores in Star Formation: A Case Study in the W51 North Region. *ApJ*, 763:135.

Tassis, K., Willacy, K., Yorke, H. W., and Turner, N. J. (2012). Non-equilibrium Chemistry of Dynamically Evolving Prestellar Cores. II. Ionization and Magnetic Field. *ApJ*, 754:6.

Troland, T. H. and Crutcher, R. M. (2008). Magnetic Fields in Dark Cloud Cores: Arecibo OH Zeeman Observations. *ApJ*, 680:457–465.

Truelove, J. K., Klein, R. I., McKee, C. F., Holliman, II, J. H., Howell, L. H., and Greenough, J. A. (1997). The Jeans Condition: A New Constraint on Spatial Resolution in Simulations of Isothermal Self-gravitational Hydrodynamics. *ApJL*, 489:L179–L183.

Vaillancourt, J. E. (2006). Placing Confidence Limits on Polarization Measurements. *PASP*, 118:1340–1343.

Vázquez-Semadeni, E., Ballesteros-Paredes, J., and Klessen, R. S. (2003). A Holistic Scenario of Turbulent Molecular Cloud Evolution and Control of the Star Formation Efficiency: First Tests. *ApJL*, 585:L131–L134.

Vázquez-Semadeni, E., Banerjee, R., Gómez, G. C., Hennebelle, P., Duffin, D., and Klessen, R. S. (2011). Molecular cloud evolution - IV. Magnetic fields, ambipolar diffusion and the star formation efficiency. *MNRAS*, 414:2511–2527.

Vázquez-Semadeni, E., Colín, P., Gómez, G. C., Ballesteros-Paredes, J., and Watson, A. W. (2010). Molecular Cloud Evolution. III. Accretion Versus Stellar Feedback. *ApJ*, 715:1302–1317.

Vázquez-Semadeni, E., Gómez, G. C., Jappsen, A.-K., Ballesteros-Paredes, J., and Klessen, R. S. (2009). High- and Low-Mass Star-Forming Regions from Hierarchical Gravitational Fragmentation. High Local Star Formation Rates with Low Global Efficiencies. *ApJ*, 707:1023–1033.

Vazquez-Semadeni, E., Gonzalez-Samaniego, A., and Colin, P. (2016). Hierarchical Cluster Assembly in Globally Collapsing Clouds. *ArXiv e-prints*.

Vazquez-Semadeni, E., Passot, T., and Pouquet, A. (1995). A turbulent model for the interstellar medium. 1: Threshold star formation and self-gravity. *ApJ*, 441:702–725.

Vazquez-Semadeni, E., Passot, T., and Pouquet, A. (1996). Influence of Cooling-induced Compressibility on the Structure of Turbulent Flows and Gravitational Collapse. *ApJ*, 473:881.

Viti, S., Girart, J. M., Garrod, R., Williams, D. A., and Estalella, R. (2003). The molecular condensations ahead of Herbig-Haro objects. II. A theoretical investigation of the HH 2 condensation. *A& A*, 399:187–195.

Viti, S., Girart, J. M., and Hatchell, J. (2006). An observational survey of molecular emission ahead of Herbig-Haro objects. *A& A*, 449:1089–1100.

Viti, S. and Williams, D. A. (1999). Chemical evolution ahead of Herbig-Haro objects. *MNRAS*, 310:517–526.

Wang, H., Bell, R. C., Iedema, M. J., Tsekouras, A. A., and Cowin, J. P. (2005). Sticky Ice Grains Aid Planet Formation: Unusual Properties of Cryogenic Water Ice. *ApJ*, 620:1027–1032.

Whitworth, A. (1979). The erosion and dispersal of massive molecular clouds by young stars. *MNRAS*, 186:59–67.

Wilcock, L. A., Ward-Thompson, D., Kirk, J. M., Stamatellos, D., Whitworth, A., Battersby, C., Elia, D., Fuller, G. A., DiGiorgio, A., Griffin, M. J., Molinari, S., Martin, P., Mottram, J. C., Peretto, N., Pestalozzi, M., Schisano, E., Smith, H. A., and Thompson, M. A. (2012). Isolated starless cores in infrared dark clouds in the Hi-GAL survey. *MNRAS*, 424:716–727.

Wilson, T. L. and Matteucci, F. (1992). Abundances in the interstellar medium. *A&A Rev.*, 4:1–33.

Yang, B., Stancil, P. C., Balakrishnan, N., and Forrey, R. C. (2010). Rotational Quenching of CO due to H_2 Collisions. *ApJ*, 718:1062–1069.

Yang, J., Ohashi, N., and Fukui, Y. (1995). Interferometric Observations of the Circumstellar Molecular Structure around the Young Stellar Object in L1287. *ApJ*, 455:175.

Yang, J., Umemoto, T., Iwata, T., and Fukui, Y. (1991). A millimeter-wave line study of L1287 - A case of induced star formation by stellar wind compression? *ApJ*, 373:137–145.

Zamora-Avilés, M. and Vázquez-Semadeni, E. (2014). An Evolutionary Model for Collapsing Molecular Clouds and their Star Formation Activity. II. Mass Dependence of the Star Formation Rate. *ApJ*, 793:84.

Zamora-Avilés, M., Vázquez-Semadeni, E., and Colín, P. (2012). An Evolutionary Model for Collapsing Molecular Clouds and Their Star Formation Activity. *ApJ*, 751:77.

Zapata, L. A., Palau, A., Ho, P. T. P., Schilke, P., Garrod, R. T., Rodríguez, L. F., and Menten, K. (2008). Forming an early O-type star through gas accretion? *A& A*, 479:L25–L28.

Zhang, Q., Qiu, K., Girart, J. M., (Baobab) Liu, H., Tang, Y.-W., Koch, P. M., Li, Z.-Y., Keto, E., Ho, P. T. P., Rao, R., Lai, S.-P., Ching, T.-C., Frau, P., Chen, H.-H., Li, H.-B., Padovani, M., Bontemps, S., Csengeri, T., and Juárez, C. (2014). Magnetic Fields and Massive Star Formation. *ApJ*, 792:116.

Zuckerman, B. and Palmer, P. (1974). Radio radiation from interstellar molecules. *ARA&A*, 12:279–313.